

AD _____
(Leave blank)

Award Number:
W81XWH-06-01-0791

TITLE:
Development and Optimization of a Dedicated, Hybrid Dual-Modality SPECT-CmT System for Improved Breast Lesion Diagnosis

PRINCIPAL INVESTIGATOR:
Priti Madhav

CONTRACTING ORGANIZATION:
Duke University
Durham NC, 27708

REPORT DATE:
January 2010

TYPE OF REPORT:
Annual Summary

PREPARED FOR: U.S. Army Medical Research and Materiel Command
Fort Detrick, Maryland 21702-5012

DISTRIBUTION STATEMENT: (Check one)

- ☒ Approved for public release; distribution unlimited
- ☐ Distribution limited to U.S. Government agencies only;
report contains proprietary information

The views, opinions and/or findings contained in this report are those of the author(s) and should not be construed as an official Department of the Army position, policy or decision unless so designated by other documentation.

REPORT DOCUMENTATION PAGE				Form Approved OMB No. 0704-0188	
Public reporting burden for this collection of information is estimated to average 1 hour per response, including the time for reviewing instructions, searching existing data sources, gathering and maintaining the data needed, and completing and reviewing this collection of information. Send comments regarding this burden estimate or any other aspect of this collection of information, including suggestions for reducing this burden to Department of Defense, Washington Headquarters Services, Directorate for Information Operations and Reports (0704-0188), 1215 Jefferson Davis Highway, Suite 1204, Arlington, VA 22202-4302. Respondents should be aware that notwithstanding any other provision of law, no person shall be subject to any penalty for failing to comply with a collection of information if it does not display a currently valid OMB control number. PLEASE DO NOT RETURN YOUR FORM TO THE ABOVE ADDRESS.					
1. REPORT DATE (DD-MM-YYYY) 01-31-2010		2. REPORT TYPE Annual Summary		3. DATES COVERED (From - To) 01-01-2009 to 12-31-2009	
4. TITLE AND SUBTITLE Development and Optimization of a Dedicated, Hybrid Dual-Modality SPECT-CmT System for Improved Breast Lesion Diagnosis				5a. CONTRACT NUMBER	
				5b. GRANT NUMBER W81XWH-06-1-0791	
				5c. PROGRAM ELEMENT NUMBER	
6. AUTHOR(S) Priti Madhav Email: priti.madhav@duke.edu				5d. PROJECT NUMBER	
				5e. TASK NUMBER	
				5f. WORK UNIT NUMBER	
7. PERFORMING ORGANIZATION NAME(S) AND ADDRESS(ES) Duke University Office of Sponsored Programs Box 104135 Durham, NC 27708 E-mail: priti.madhav@duke.edu				8. PERFORMING ORGANIZATION REPORT NUMBER	
9. SPONSORING / MONITORING AGENCY NAME(S) AND ADDRESS(ES) U.S. Army Medical Research and Materiel Command Fort Detrick, Maryland 21702-5012				10. SPONSOR/MONITOR'S ACRONYM(S)	
				11. SPONSOR/MONITOR'S REPORT NUMBER(S)	
12. DISTRIBUTION / AVAILABILITY STATEMENT Approved for public release ; distribution unlimited					
13. SUPPLEMENTARY NOTES					
14. ABSTRACT The overall objective of this project was to implement a dual-modality single photon emission computed tomography (SPECT) and x-ray computed mammotomography (CmT) system for the detection and staging of breast cancer, monitoring of treatment therapies, and improving surgical biopsy guidance. The sequential acquisition with emission (nuclear) and transmission (x-ray) 3D imaging systems can aid in localizing the radioactive uptake of a tumor from the emission image by using the anatomical structure from the transmission image. In this third and final year, CmT scatter correction was implemented to help in characterizing different materials <i>in vivo</i> in the CmT reconstructed images based on absolute attenuation values. Attenuation correction of SPECT images was also initiated. Different attenuation maps were compared by measuring SNR, contrast, and quantification of radiotracer uptake. Other aspects of the training program were accomplished including the publication of two first author manuscripts in a peer-reviewed journal, presentations at various local and international conferences, and writing of the PhD dissertation.					
15. SUBJECT TERMS X-ray imaging, Nuclear Medicine Imaging, SPECT, CT, Molecular Breast Imaging, Mammotomography					
16. SECURITY CLASSIFICATION OF:			17. LIMITATION OF ABSTRACT Unlimited	18. NUMBER OF PAGES 59	19a. NAME OF RESPONSIBLE PERSON Priti Madhav
a. REPORT Unclassified	b. ABSTRACT Unclassified	c. THIS PAGE Unclassified			19b. TELEPHONE NUMBER (include area code) (919)684-7948

Table of Contents

A. INTRODUCTION	4
B. BODY	4
C. KEY RESEARCH ACCOMPLISHMENTS	12
D. REPORTABLE OUTCOMES	12
E. CONCLUSION	14
F. REFERENCES	14
APPENDIX A: STATEMENT OF WORK	16
APPENDIX B: SPIE CONFERENCE PROCEEDING	17
APPENDIX C: IEEE MIC CONFERENCE PROCEEDING	27
APPENDIX D: IEEE TNS MANUSCRIPT	32
APPENDIX E: PMB MANUSCRIPT	42

A. INTRODUCTION

The overall objective of this project was to implement a dual-modality single photon emission computed tomography (SPECT) and x-ray computed mammotomography (CmT) system for the detection and staging of breast cancer, monitoring of treatment therapies, and improving surgical biopsy guidance. The sequential acquisition with emission (nuclear) and transmission (x-ray) 3D imaging systems can aid in localizing the radioactive uptake of a tumor from the emission image by using the anatomical structure from the transmission image. In this third and final year, CmT scatter correction was implemented to help in characterizing different materials *in vivo* in the CmT reconstructed images based on absolute attenuation values. Attenuation correction of SPECT images was also initiated. Different attenuation maps were compared by measuring SNR, contrast, and quantification of radiotracer uptake. Other aspects of the training program were accomplished including the publication of two first author manuscripts in a peer-reviewed journal, presentations at various local and international conferences, and writing of the PhD dissertation.

B. BODY

The Statement of Work along with the original project timeline is attached in Appendix A of this Progress Report. In the following sections, the remaining tasks for Year 3 are discussed. As a reference, Figure 1 is a photograph of the current dedicated dual-modality SPECT-CmT breast scanner with a customized patient bed.

Task 2: Optimize CmT system by applying corrections to improve image quality

Task 2(b): CmT Scatter Correction

Due to the complexity of this task, this work was started in Year 2. Based on preliminary studies that were accomplished in Year 2, a final design of the beam stop array (BSA) was drawn up and built at the machine shop. The BSA was a 10x10cm acrylic plate with 2mm diameter lead beads arranged in a square pattern, spaced 0.5cm apart (Figure 2). This BSA was attached to the front of the collimator housing, which was approximately 15cm from the x-ray focal spot, during a CmT acquisition such that the amount of scatter in the object could be measured. The theory behind this method is that any incident x-rays striking a lead ball at 36keV (i.e. photon energy of the quasi-monochromatic x-ray source used by this system) would be completely stopped before reaching the detector. Consequently, the measured value in the shadow behind this beam stop should be zero (except for a small DC offset from the digital detector). However, due to the presence of scatter, the detected quantity is greater than zero + DC offset. Therefore, any signal detected behind this beam stop can be assumed to be primarily due to scatter. For acquisitions without the BSA, this plate was replaced with a clear 10x10cm acrylic plate to provide an equal amount of attenuating material as when the BSA was in place.

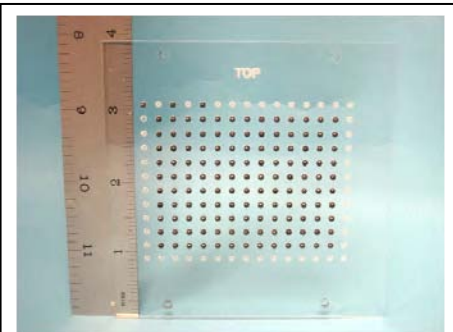


FIGURE 2: Photograph of beam stop array with 2mm lead beads that was placed in front of the collimator (~15cm from the x-ray focal spot) for scatter measurements.



FIGURE 1: Photograph of SPECT-CmT dedicated breast scanner with a customized patient bed. Arrows illustrate the system movement.

The scatter algorithm, written in MATLAB (*The Mathworks, Inc.*, Natick, MA), was extended to measure the scatter from a single projection to all 240 projections (# of projections acquired from a 360° CmT acquisition). A flow chart is presented in Figure 3. From a CmT projection with only the BSA in the FOV, the location of all the lead beads was found. In addition, for each projection, a region containing only the object was automatically created by thresholding the images using a k-means algorithm [1]. The k-means algorithm is a clustering algorithm which divides the pixel values into k groups such that each pixel value belongs to a cluster with the nearest mean. In this case, k was set to 2 with one cluster signifying the background and the second cluster representing the object. Next, the amount of scatter in all projections was measured using images with the BSA and object in the FOV. In this step, an average scatter value was measured over a 5x5pixel ROI in each lead bead

localized inside the object. For each row containing the lead beads, the average scatter values were extrapolated using a cubic spline to obtain a single scatter measurement near the boundaries at both ends of

the object. This was repeated for each column with the lead beads. After the extrapolation along each row and column was completed, a 2D cubic spline interpolation was done to obtain a 2D scatter profile over the entire projection image. This profile was subtracted from projection images without the BSA to obtain final projection images with minimal scatter [2].

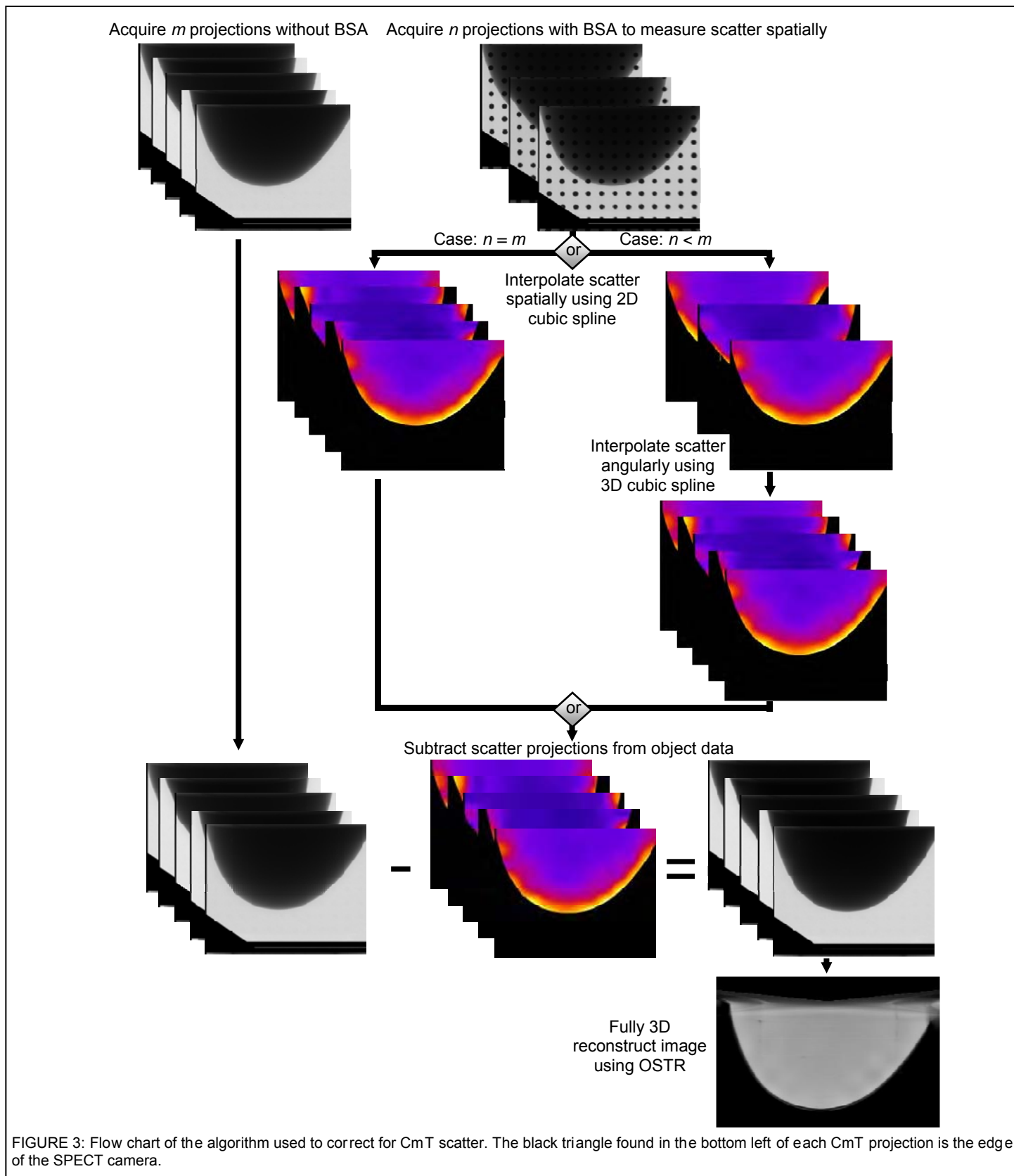


FIGURE 3: Flow chart of the algorithm used to correct for CmT scatter. The black triangle found in the bottom left of each CmT projection is the edge of the SPECT camera.

In addition, this algorithm was written such that scatter measurements could be obtained from only a few projections or from all 240 projections. In this case, after the 2D scatter profiles for 6 evenly spaced projections were measured, a 3D cubic spline interpolation between the measured azimuthal angles was performed to obtain the 2D scatter maps for all projections. The importance of this flexibility in the algorithm is that scatter measurements should not be obtained for all 240 projections, since that would double the amount of dose given to the patient. So, this algorithm was also tested on far fewer numbers of projection views.

This scatter technique was implemented on CmT acquisitions with the goal of enhancing image visualization and characterizing different materials *in vivo* based on absolute attenuation values measured from the reconstructed images. An oral presentation for this work will be given next month at the *2010 SPIE Medical Imaging Conference* (Appendix B). For this quantitative study, a multi-material rod phantom and human cadaver breast were scanned (Figure 4). A previously acquired human volunteer study was retrospectively scatter corrected as described below (Note that clinical patient scanning was approved by the Duke University Medical Center Institutional Review Board (IRB) and informed written consent was obtained from the volunteer). Actual attenuation coefficient values of all the materials are presented in Table 1. The multi-material rod phantom was also custom built at the machine shop. It contained five different materials: acrylic, delrin, polyethylene (PE), and fat-equivalent and glandular-equivalent plastic rods (*Computerized Imaging Reference Systems, Inc.*, Norfolk, VA). Each rod had a length and diameter of 4.5cm and 1.9cm, respectively, and the rods were arranged in a pentagonal pattern. An earlier study showed that the fat-equivalent and glandular-equivalent phantoms available by CIRS have very similar composition and attenuation coefficients to actual fat and glandular tissue [3]. This phantom was placed in a water-filled cylinder with an inner length and diameter of 5.6cm and 8.2cm, respectively.

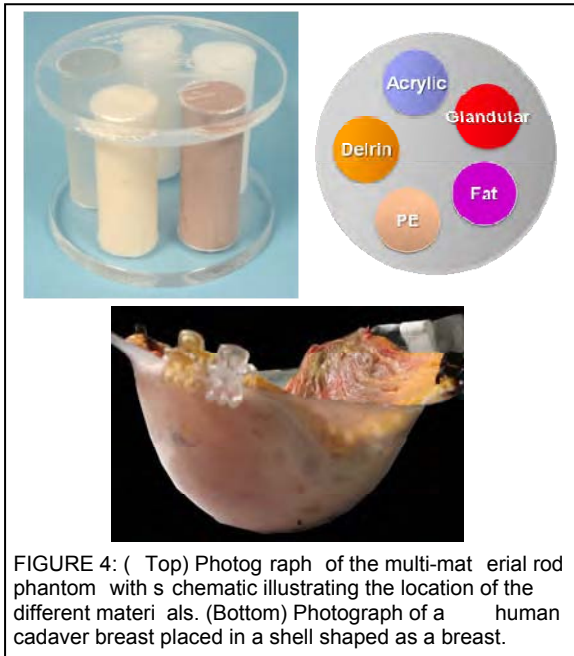


FIGURE 4: (Top) Photograph of the multi-material rod phantom with schematic illustrating the location of the different materials. (Bottom) Photograph of a human cadaver breast placed in a shell shaped as a breast.

The whole cadaver breast, obtained from a 48-year old woman, was placed in a breast shaped shell (nipple-to-chest distance of ~7cm, medial-to-lateral distance of ~16cm, and superior-to-inferior distance of ~18 cm). Prior to imaging, the cadaver breast was fastened by clips to the breast shell and refrigerated overnight. The next day the cadaver breast was defrosted before imaging with the CmT sub-system.

The human volunteer data was from a 54yr old, 96kg patient with biopsy confirmed ductal carcinoma *in situ* (DCIS) anterior to her chest wall. The dimensions of her breast were nipple-to-chest distance of ~7.5cm and superior-to-inferior distance of ~11.5cm. As mentioned in the previous paragraph, since the BSA was not implemented at the time of the patient study, a post-acquisition scatter correction was performed to approximate the amount of scatter present in the images obtained from the patient's breast. This was done by first acquiring a 360° data set of a breast phantom filled with water with the CmT sub-system with and without the BSA. Scatter images obtained with this phantom at 0°, 40°, 80°, 120°, 160°, and 200° were scaled and registered to the projections of the patient's breast at these same angles. Using these six scaled and registered scatter projections, the amount of scatter for the rest of the projections was calculated using 3D cubic spline interpolation as described previously.

TABLE 1: Narrow beam attenuation coefficient values (in cm^{-1}) of the materials in the multi-material rod phantom and cadaver breast spline interpolated to 36keV

Material	Attenuation coefficient
Acrylic ^a 0.313	6
Delrin ^a 0.349	0
Ductal Carcinoma (Breast Tissue) ^c	0.3102
Fat (CIRS) ^b 0.230	5
Fat (Breast Tissue) ^c 0.228	4
Glandular (CIRS) ^b	0.3037
Glandular (Breast Tissue) ^c	0.3009
Polyethylene ^a	0.2285
Water ^a	0.3130

^a NIST table of x-ray mass attenuation coefficients [4]

^b Byng, Mainprize, and Yaffe [3]

^c Johns and Yaffe [5]

Contrast and attenuation values were calculated for the different materials along with line profiles and image histograms. In addition, the reconstructed images were “flattened” according to [6, 7] to reduce any remaining non-uniformity.

Line profiles of the multi-material rod phantom are shown in Figure 5 to illustrate that after scatter correction and post-reconstruction flattening, the contrast improved between the different materials and the attenuation values were aligned closer to their actual ones. Measured attenuation values had a less than 8% error from actual attenuation

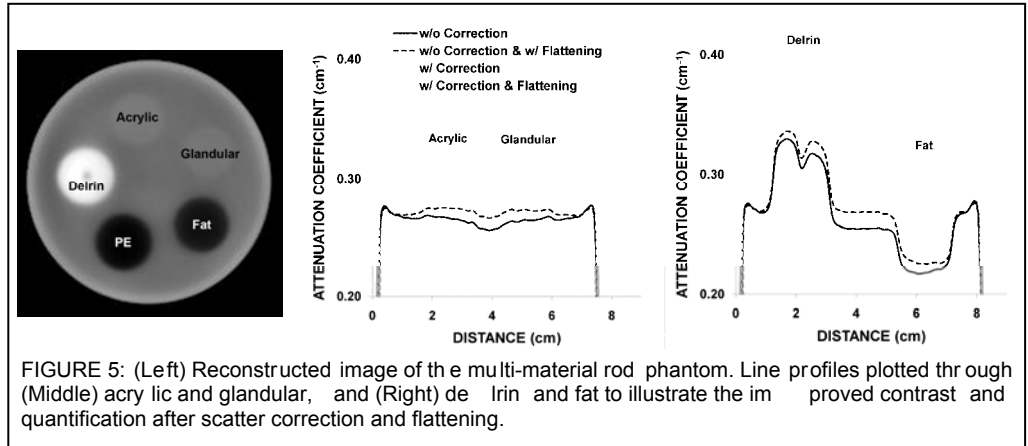


FIGURE 5: (Left) Reconstructed image of the multi-material rod phantom. Line profiles plotted through (Middle) acrylic and glandular, and (Right) delrin and fat to illustrate the improved contrast and quantification after scatter correction and flattening.

coefficients after only applying scatter correction (Table 2). This was very similar to values that were obtained using a narrower fan-beam-like geometry, which in theory, should have far less scatter in the final images.

TABLE 2: Measured attenuation coefficient (in cm^{-1}) and % error of the different materials in the multi-material rod phantom

Material	w/o Scatter Correction		w/o Scatter Correction & w/ Flattening		w/ Scatter Correction		w/ Scatter Correction & Flattening	
	Atten Coef	% Error	Atten Coef	% Error	Atten Coef	% Error	Atten Coef	% Error
Acrylic	0.2659	15.2	0.273	1	0.3079	1.8	0.320	4
Delrin	0.3196	8.4	0.327	6	0.3755	7.6	0.395	0
Fat	0.2121	8.0	0.228	5	0.2447	6.2	0.261	4
Glandular	0.2644	12.9	0.272	2	0.3110	2.4	0.319	2
PE	0.2136	6.5	0.222	2	0.2417	5.8	0.251	9
Water	0.2658	15.3	0.267	7	0.3091	1.2	0.315	2

Histograms of the reconstructed images of the cadaver breast also showed how scatter correction improved the distinction between different tissues in the breast. In Figures 6 and 7, image histograms are shown for single coronal and sagittal reconstructed slices. Due to cupping, the image histogram of the non-scatter corrected coronal slice showed three peaks since the center appeared darker (i.e. lower attenuation

coefficient) than the edges. On the other hand, the image histogram of the non-scatter corrected sagittal slice incorrectly showed only a single peak when in actuality there should have been at least two separate distributions since there were two different types of tissue, fat and glandular, in the slice. Having a single peak makes it difficult to distinguish between the two different tissues, though it can be assumed that there were two underlying distributions [8]. After scatter correction and/or post-reconstruction flattening, these images were higher in contrast and more uniform throughout the entire 3D volume which made quantification of the different tissues in the breast possible. The peaks representing glandular and fat in the image histogram for the scatter corrected cases were shown to be narrower and with values that are closer to the true attenuation value of fat and glandular tissue [5]. Less than 10% error in attenuation value measurement of fat and glandular tissue was measured after applying scatter correction (Table 3). However, only applying the post-reconstruction flattening technique to the images demonstrated that the measured attenuation values did not match its true values, indicating the importance of implementing scatter correction for more accurate quantification.

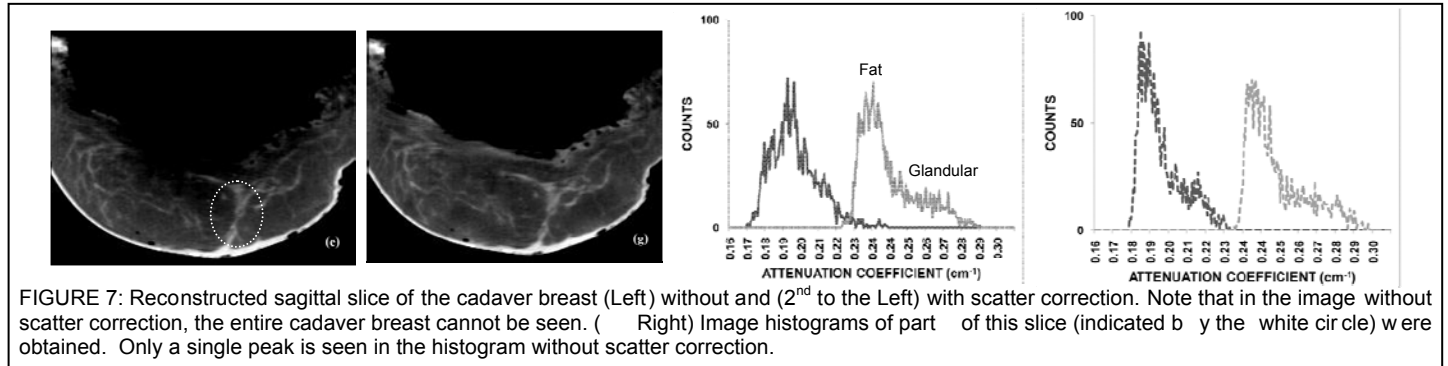
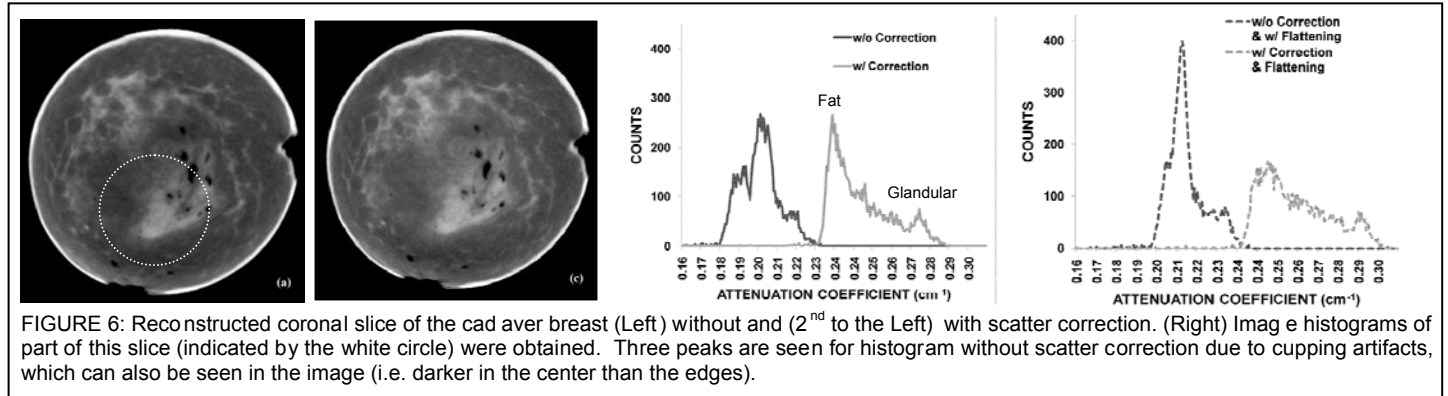


TABLE 3: Measured attenuation values (in cm^{-1}) and % error for fat and glandular for reconstructed images of the breast of the human cadaver and human volunteer

		Material	w/o Scatter Correction		w/o Scatter Correction & w/ Flattening		w/ Scatter Correction		w/ Scatter Correction & Flattening	
			Atten Coef	% Error	Atten Coef	% Error	Atten Coef	% Error	Atten Coef	% Error
Cadaver Breast	Coronal	Fat	0.1873	18.0	0.211	4	0.232	1	0.2498	9.4
		Glandular	0.2148	28.6	0.230	4	0.279	3	0.2960	1.6
	Sagittal	Fat	0.2025	11.3	0.196	5	0.236	3	0.2407	5.4
		Glandular	0.2223	26.1	0.224	1	0.272	0	0.2798	7.0
Patient	Coronal	Fat	0.198	6	-	-	0.2270	0.6	-	-
		Glandular	0.227	5	-	-	0.2832	5.9	-	-

Using the cadaver breast, scatter projections were also measured from two different sets of 6 uniformly distributed angles: one set using 0° , 60° , 120° , 180° , 240° , and 300° , and the second set using 45° , 105° , 165° , 225° , 285° , and 345° . Results showed that there was no dependency or effect on which set of 6 angles were chosen for scatter measurements since both sets gave similar results to each other, and importantly, to the

data set that used all 240 projections to measure scatter. During a procedure, scatter measurements could be obtained before the scan when a few scout images are acquired to assure that the breast is at the center of rotation (COR) or they could be obtained during the acquisition itself with the BSA moved into place when the system is at a specific angle. A previous study [9] had shown that with the CmT system in which the central ray of the cone-beam is aligned with the COR, up to 60° of projection data can be removed from the entire 360° scan with minimal distortion and degradation. Hence, it can be inferred that taking out six projection images from the entire scan will not harm the resolution or image quality.

Another quantification study was done with a human volunteer, post hoc, in which scatter measurements were not taken during acquisition, since the BSA was not implemented at the time of this scan. Results were promising in that the contrast and attenuation quantification between fat and glandular improved (Figure 8). A less than 6% error from actual attenuation values for fat and glandular tissue seems to have been measured (Table 3). However, the addition of artifacts in the scatter corrected reconstructed images could cause misinterpretation. Therefore, it is still considered necessary to implement scatter correction using the proposed BSA method individually for each patient.

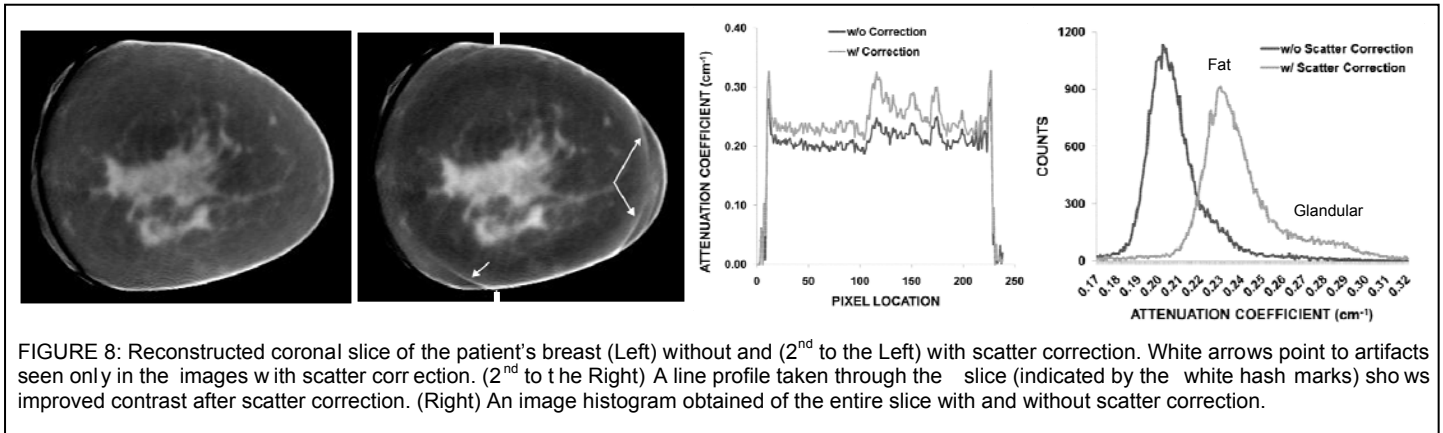


FIGURE 8: Reconstructed coronal slice of the patient's breast (Left) without and (2nd to the Left) with scatter correction. White arrows point to artifacts seen only in the images with scatter correction. (2nd to the Right) A line profile taken through the slice (indicated by the white hash marks) shows improved contrast after scatter correction. (Right) An image histogram obtained of the entire slice with and without scatter correction.

This study showed that minimizing beam hardening and correcting for scatter can reduce cupping artifacts, improve intrinsic material contrast, and attain pixel values closer to the actual attenuation value of a material. Results showed that scatter-corrected data yielded attenuation values within 10% (range from 0.0 to 9.6%) to the actual attenuation coefficients (Table 2 and 3).

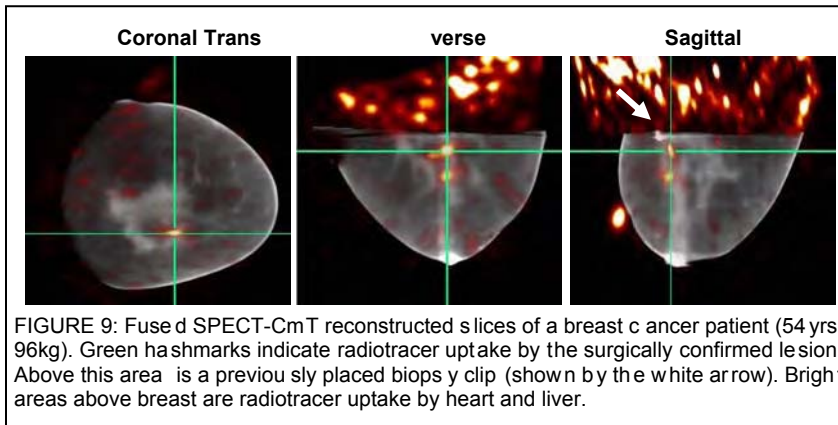
Task 3: Evaluate SPECT system for quantification measurements of lesion activity

Task 3(a): Investigate, implement, and compare two attenuation correction methods (i.e. uniform attenuation distribution, CmT-based attenuation distribution) to apply to SPECT data

AND

Task 3(b): Perform SPECT quantification measurements incorporating all corrections using phantoms and lesions with known concentration activity

Two different types of SPECT attenuation corrections were compared: uniform and CmT-based distribution [10, 11]. In the uniform distribution, a uniform attenuation correction (0.1537cm^{-1} which is the attenuation value of water at 140keV) was assumed within the object. Two uniform attenuation masks were obtained separately from SPECT and CmT. For the CmT-based distribution, the scatter corrected CmT reconstructed images acquired at a mean energy of 36keV were translated and rotated relative to the 140keV acquired SPECT data [12-14]. This was done by aligning the external fiducial markers seen in both SPECT and CmT reconstructed data using AMIDE. To obtain the attenuation map at 140 keV, the CmT images were scaled by the ratio of attenuation coefficients of water at SPECT and CmT energies, 140keV and 36keV, respectively. Using the NIST table of x-ray mass attenuation coefficients, the attenuation coefficients at 140 and 36keV for water were 0.1537 and 0.3130, respectively, to give a ratio of 0.4911 [4]. As seen in Table 1, water and glandular tissue are very similar in attenuation value. Another attenuation map at 140 keV was also obtained by scaling the images by the ratio of attenuation coefficients of fat, 0.6370. All attenuation maps were integrated into the reconstruction.



signs of Tc^{99m} -sestamibi uptake anterior to the biopsy clip signifying a suspicious lesion in this patient (Figure 9). This lesion was DCIS, as confirmed by surgical excision. SNR and contrast measurements were taken in this area using the different attenuation maps (Table 4).

TABLE 4: SNR and contrast measured using various attenuation maps

Attenuation Map	SNR	Contrast
None 0.02		0.07
SPECT Uniform Mask	0.70	2.30
CmT Uniform Mask	0.59 1.96	
Non-scatter corrected CmT scaled to 140keV using water	0.33 1.06	
Non-scatter corrected CmT scaled to 140 keV using fat	0.45 1.47	
Scatter corrected CmT scaled to 140keV using water	0.36 1.16	
Scatter corrected CmT scaled to 140 keV using fat	0.49 1.63	

As expected the SNR and contrast improved when applying an attenuation map to the reconstructed images. However, a range of SNR and contrast measurements were found for the different types of attenuation maps used. The SPECT uniform map gave the highest SNR and contrast which could likely be due to the mask created from SPECT images consisting of a larger breast volume than that from the CmT. As illustrated in Figure 9, unlike the CmT images, SPECT could “see” into the chest wall, hence giving a larger attenuation volume that could be used in the reconstruction. The scatter corrected CmT -scaled attenuation map did improve the SNR and contrast in the SPECT image. However results varied with which scale ratio (water or fat) was chosen. An area having a higher attenuation value indicates a higher percentage of the photon to change direction resulting in a possible missed count. Therefore, when scaling the images by the ratio calculated from fat, the measured attenuation values in the CmT images were higher than when the images were scaled by the ratio calculated from water resulting in a higher SNR and contrast.

Based on a SPECT quantification scheme that was implemented in our lab in which I was also a collaborator and co-author (Appendix C), the uptake of the whole breast was also measured for the different attenuation maps (Table 5). In the literature, it has been shown that the uptake in the breast is about 0.02-0.07 $\mu\text{Ci/mL}$ when assaying the tissues themselves [15]. Without attenuation correction of the images, the value is below this range. However, for all other attenuation masks, the values ranged from 0.019-0.024 $\mu\text{Ci/mL}$. Since this breast has a higher fat than glandular distributions, it can be concluded that the map obtained using the ratio with fat may be closer to actual values. More work needs to be done to definitively validate this conclusion.

TABLE 5: Mean value of radiotracer uptake in the patient's breast

Attenuation Map	Mean Uptake ($\mu\text{Ci/mL}$)
None	0.012
SPECT Uniform Mask	0.029
CmT Uniform Mask	0.024
Non-scatter corrected CmT scaled to 140keV using water	0.019
Non-scatter corrected CmT scaled to 140 keV using fat	0.022
Scatter corrected CmT scaled to 140keV using water	0.020
Scatter corrected CmT scaled to 140 keV using fat	0.024

Future work needs to be done in scaling the CmT data to 140keV to improve attenuation correction and quantification. One possible method that could be done would be to first segment the CmT reconstructed data separately into fat and glandular [16]. Each of the two areas could then be scaled by a different ratio. Fat would be scaled by 0.6370 and glandular would be scaled by 0.5068 to obtain attenuation values at 140keV.

Task 4: Complete other aspects of the breast cancer training program

Task 4(b): Publish work in journals

Two first author papers were published in peer-reviewed journals in Year 3. One was on the modulation transfer function (MTF) measurements made with 3D SPECT which was published in the *IEEE Transactions of Nuclear Science* (attached in App endix D). The second paper was on the effect of cone-beam tilted CmT source on distortion and artifacts in images which was published in *Physics in Medicine and Biology* (Appendix E). Other first author papers that are still in the works include MTF measurements with 3D CmT (submitted to *Medical Physics*) and quantification of materials *in vivo* using absolute attenuation coefficients (to be submitted to *Academic Radiology*). Over the duration of this grant, nine conference proceedings have been published and twelve presentations have been given.

Task 4(c): Attend and present at local conferences

At the end of October, I presented at the *Breast Imaging Scientific Symposium* at UNC. My topic was on "3D Molecular Breast Imaging Using Dedicated SPECT-CT". At this conference, it was also great to get an overview of other breast imaging modalities.

Task 4(d): Attend and present at international conferences

I will be presenting at the upcoming *2010 SPIE Medical Imaging Conference on "Development of *in vivo* characterization of breast tissues through absolute attenuation coefficients using dedicated cone-beam CT"* (Appendix B).

Task 4(e): Prepare thesis and defend

I am currently working on writing and putting together my thesis. I hope to defend within the next few months.

C. KEY RESEARCH ACCOMPLISHMENTS

From the original proposed Statement of Works, Tasks 2-4 were completed in Year 3.

- Built a beam stop array to measure scatter, and wrote the code to implement scatter correction for all projections collected with the CmT system.
- Performed a study on CmT quantification of materials *in vivo* based on attenuation coefficient values in the reconstructed images. This work will be presented at the *2010 SPIE Medical Imaging Conference* (Appendix B).
- Worked on attenuation correction in SPECT images to improve SNR, contrast, and lesion quantification.
- Contributed to work on quantification in SPECT images which was presented at the *2009 IEEE Medical Imaging Conference* (Appendix C).
- Had manuscripts published in *IEEE Transactions of Nuclear Science* (Appendix D) and *Physics of Medicine and Biology* (Appendix E) with others on deck to be submitted.

D. REPORTABLE OUTCOMES

YEAR 3

Peer-Reviewed Papers

P Madhav, DJ Crotty, RL McKinley, MP Tornai. 2009. "Evaluation of tilted cone-beam CT orbits in the development of a dedicated hybrid mammothomograph." *Phys Med Biol.* 54(12): 3659-676.

P Madhav, JE Bowsher, SJ Cutler, MP Tornai. 2009. "Characterizing the MTF in 3D for a quantized SPECT camera having arbitrary trajectories." *IEEE Trans Nucl Sci.* 56(3, Part 1): 661-670.

P Madhav, RL McKinley, E Samei, JE Bowsheer, MP Tornai. "A multi-wire technique to characterize the MTF in 3D for computed mammothomography." In Preparation to *Med Phys*

P Madhav, CM Li, MP Tornai. "Characterization of Breast Tissues through Absolute Attenuation Coefficients using Dedicated Cone-Beam CT." In Preparation to *Acad Rad*

Conference Proceedings

DJ Crotty, RL McKinley, **P Madhav**, SJ Cutler, MP Tornai. "Initial investigation of novel trajectories to improve chest wall imaging in a dedicated breast computed tomography system." Presented at the *2009 SPIE Medical Imaging Conference*, Orlando, FL, 7-12 Feb. 2009, and published in *Proc. SPIE: Physics of Medical Imaging*, 7258:72585L-1-72585L-10.

KL Perez, SJ Cutler, **P Madhav**, MP Tornai. "Towards quantification of dedicated breast SPECT using non-traditional acquisition trajectories." Presented at the *2009 IEEE Nucl. Sci. Symposium & Med. Imaging Conference*, Orlando, FL, 25-31 Oct. 2009 and to be published in *IEEE Conference Record NSS/MIC*.

Abstracts and Presentations

P Madhav, DJ Crotty, SJ Cutler, KL Perez, MP Tornai. "3D Molecular Breast Imaging Using Dedicated SPECT-CT." Presented at the *2009 Breast Imaging Scientific Symposium*, Chapel Hill, NC, 29 Oct. 2009.

P Madhav, CM Li, MP Tornai. "Development of *in vivo* characterization of breast tissues through absolute attenuation coefficients using dedicated cone-beam CT." Presenting at the *2010 SPIE Medical Imaging Conference*, San Diego, CA, 13-18 Feb. 2010.

YEARS 1-2

Conference Proceedings

DJ Crotty, **P Madhav**, RL McKinley, MP Tornai. "Investigating novel patient bed designs for use in a hybrid dual modality dedicated 3D breast imaging system." Presented at the *2007 SPIE Medical Imaging Conference*, San Diego, CA, 17-22 Feb. 2007, and published in *Proc. SPIE: Physics of Medical Imaging*, 6510:H1-10.

P Madhav, DJ Crotty, RL McKinley, MP Tornai. "Evaluation of lesion distortion at various CT system tilts in the development of a hybrid system for dedicated mammotomography." Presented at the *2007 SPIE Medical Imaging Conference*, San Diego, CA, 17-22 Feb. 2007, and published in *Proc. SPIE: Physics of Medical Imaging*, 6510:F1-12.

KL Perez, **P Madhav**, DJ Crotty, MP Tornai. "Analysis of patient bed positioning in SPECT-CT imaging for dedicated mammotomography." Presented at the *2007 SPIE Medical Imaging Conference*, San Diego, CA, 17-22 Feb. 2007, and published in *Proc. SPIE: Physics of Medical Imaging*, 6510:371-8.

P Madhav, SJ Cutler, KL Perez, DJ Crotty, RL McKinley, TZ Wong, MP Tornai. "Initial patient study with dedicated dual-modality SPECT-CT mammotomography." Presented at the *2007 IEEE Nucl. Sci. Symposium & Med. Imaging Conference*, Honolulu, Hawaii, 28 Oct.-3 Nov. 2007, and published in *IEEE Conference Record NSS/MIC*, 5:3781-3787.

SJ Cutler, **P Madhav**, KL Perez, DJ Crotty, MP Tornai. "Comparison of reduced angle and fully 3D acquisition sequencing and trajectories for dual-modality mammotomography." Presented at the *2007 IEEE Nucl. Sci. Symposium & Med. Imaging Conference*, Honolulu, Hawaii, 28 Oct.-3 Nov. 2007, and published in *IEEE Conference Record NSS/MIC*, 6:4044-4050.

SJ Cutler, KL Perez, **P Madhav**, MP Tornai. "Comparison of 2D scintimammography and 3D dedicated breast SPECT using a compressible breast phantom and lesions of varying size and tracer uptake." Presented at the *2008 IEEE Fourth International Workshop on the Molecular Radiology of Breast Cancer*, Dresden, Germany, 20-21 Oct. 2008, and published in *IEEE Conference Record NSS/MIC*, 5640-5646.

KL Perez, SJ Cutler, **P Madhav**, MP Tornai. "Novel patient acquisition trajectories for optimized dedicated breast SPECT imaging." Presented at the *2008 IEEE Fourth International Workshop on the Molecular Radiology of Breast Cancer*, Dresden, Germany, 20-21 Oct. 2008, and published in *IEEE Conference Record NSS/MIC*, 5629-5634.

DJ Crotty, SJ Cutler, RL McKinley, **P Madhav**, KL Perez, MP Tornai. "Improved chest wall imaging through combined complex trajectories in dedicated dual modality SPECT-CT breast molecular imaging." Presented at the *2008 IEEE Fourth International Workshop on the Molecular Radiology of Breast Cancer*, Dresden, Germany, 20-21 Oct. 2008, and published in *IEEE Conference Record NSS/MIC*, 5650-5656.

Abstracts and Presentations

DJ Crotty, **P Madhav**, KL Perez, SJ Cutler, RL McKinley, T Wong, PK Marcom, MP Tornai. "3D molecular breast imaging with dedicated emission mammotomography: results of the first patient study." Presented at the *Duke University Center for Molecular and Biomolecular Imaging Meeting*, Durham, NC, 11-13 March, 2007 and *Duke Frontiers 2007*, Durham, NC, 14 May, 2007.

P Madhav, DJ Crotty, SJ Cutler, KL Perez, RL McKinley, MP Tornai. "A novel dual-modality SPECT-CT system dedicated to 3D volumetric breast imaging." Presented at the *Duke University Center for Molecular and Biomolecular Imaging Meeting*, Durham, NC, 11-13 March, 2007 and *Duke Frontiers 2007*, Durham, NC, 14 May, 2007.

MP Tornai, **P Madhav**, DJ Crotty, SJ Cutler, RL McKinley, KL Perez, JE Bowsher. "Initial hybrid SPECT-CT system for dedicated fully-3D breast imaging." Presented at the *2007 Society of Nuclear Medicine Meeting*, Washington, DC, 2-6 Jun. 2007, and published in *J. Nucl. Med.* 48(5). 2007.

MP Tornai, **P Madhav**, DJ Crotty, SJ Cutler, RL McKinley, KL Perez, JE Bowsher. "Application of volumetric molecular breast imaging with a dedicated SPECT-CT mammotomograph." Presented at the *2007 American Association of Physicists in Medicine Meeting*, Minneapolis, MN, 22-26 Jun. 2007, and published in *Med. Phys.* 34(6):2597.

P Madhav, SJ Cutler, DJ Crotty, KL Perez, RL McKinley, MP Tornai. "3D volumetric breast imaging with a dedicated dual-modality SPECT-CT system." Presented at the *2007 Duke Biomedical Engineering Retreat*, Myrtle Beach, SC, 7-9 Oct. 2007.

DJ Crotty, **P Madhav**, SJ Cutler, KL Perez, RL McKinley, MP Tornai, "Performance of a new dual-modality molecular-anatomical imaging system dedicated to breast cancer." Presented at the *2008 Duke Cancer Center Annual Meeting*, Durham, NC, 10 Mar. 2008.

P Madhav, SJ Cutler, DJ Crotty, KL Perez, RL McKinley, PK Marcum, TZ Wong, MP Tornai. "Dedicated molecular and anatomical breast imaging - initial patient studies." Presented at the *2008 Duke Cancer Center Annual Meeting*, Durham, NC, 10 Mar. 2008.

P Madhav, MP Tornai. "Development and optimization of a dedicated, hybrid dual-modality SPECT-CmT system for improved breast lesion diagnosis." Presented at the *2008 Era of Hope Conference*, Baltimore, MD, 25-28 Jun 2008.

P Madhav, SJ Cutler, DJ Crotty, KL Perez, RL McKinley, L Wilke, TZ Wong, MP Tornai. "Pilot patient studies using a dedicated dual-modality SPECT-CT system for breast imaging." Presented at the *2008 American Association of Physicists in Medicine Meeting*, Houston, TX, 27-31 Jul. 2008, and published in *Med. Phys.* 35(6): 2894.

E. CONCLUSION

In Year 3, CmT scatter correction was implemented, and subsequently shown to reduce image cupping and improve image contrast and absolute attenuation value quantification. With scatter correction, peaks in the image histogram could be easily designated to a certain material. The results of this work will be presented at an upcoming *SPIE Medical Imaging* conference in February 2010. Attenuation correction of SPECT images using CT-scaled scatter corrected maps was also applied and shown to improve SNR, contrast, and quantification of breast uptake. Two manuscripts have appeared in peer-reviewed journals and more papers are in the works.

F. REFERENCES

- [1] R. Gray and Y. Linde, "Vector Quantizers and Predictive Quantizers for Gauss-Markov Sources," *Communications, IEEE Transactions on*, vol. 30, pp. 381-389, 1982.
- [2] J. Y. Lo, C. E. F. Jr, J. A. Baker, and C. E. Ravin, "Scatter compensation in digital chest radiography using the posterior beam stop technique," *Med. Phys.*, vol. 21, pp. 435-443, 1994.
- [3] J. W. Byng, J. G. Mainprize, and M. J. Yaffe, "X-ray characterization of breast phantom materials," *Phys Med Biol*, vol. 43, pp. 1367-77, May 1998.
- [4] J. H. Hubbell and S. M. Seltzer, "Tables of x-ray mass attenuation coefficients and mass energy-absorption coefficients 1keV to 20MeV for elements Z=1 to 92 and 48 additional substances of dosimetric interest," Gaithersburg: National Institutes of Standards and Technology, 1996.
- [5] P. C. Johns and M. J. Yaffe, "X-ray characterization of normal and neoplastic breast tissues," *Phys. Med. Biol.*, vol. 32, pp. 675-695, 1987.
- [6] C. M. Li, W. P. Segars, G. D. Tourassi, J. M. Boone, and J. T. D. III, "Methodology for generating a 3D computerized breast phantom from empirical data," *Medical Physics*, vol. 36, pp. 3122-3131, 2009.

- [7] M. C. Altunbas, C. C. Shaw, L. Chen, C. Lai, X. Liu, T. Han, and T. Wang, "A post-reconstruction method to correct cupping artifacts in cone beam breast computed tomography," *Med Phys*, vol. 34, pp. 3109-18, Jul 2007.
- [8] T. R. Nelson, L. I. Cervino, J. M. Boone, and K. K. Lindfors, "Classification of breast computed tomography data," *Med Phys*, vol. 35, pp. 1078-86, Mar 2008.
- [9] D. J. Crotty, R. L. McKinley, P. Madhav, S. J. Cutler, and M. P. Tornai, "Initial investigation of novel trajectories to improve chest wall imaging in a dedicated breast computed tomography system," 2009, p. 72585L.
- [10] T. Kashiwagi, K. Yutani, M. Fukuchi, H. Naruse, T. Iwasaki, K. Yokozuka, S. Inoue, and S. Kondo, "Correction of nonuniform attenuation and image fusion in SPECT imaging by means of separate x-ray CT," *Ann Nucl Med*, vol. 16, pp. 255-261, 2002.
- [11] K. J. LaCroix, B. M. W. Tsui, B. H. Hasegawa, and J. K. Brown, "Investigation of the use of x-ray CT images for attenuation compensation in SPECT," *IEEE Trans Nucl Sci*, vol. 41, pp. 2793-2799, 1994.
- [12] P. E. Kinahan, D. W. Townsend, T. Beyer, and D. Sashin, "Attenuation correction for a combined 3D PET/CT scanner," *Med Phys*, vol. 25, pp. 2046-2053, 1998.
- [13] P. E. Kinahan, B. H. Hasegawa, and T. Beyer, "X-ray based attenuation correction for positron emission tomography/computed tomography scanners," *Seminars in Nuclear Medicine*, vol. 33, pp. 166-179, 2003.
- [14] K. J. LaCroix, B. M. W. Tsui, B. H. Hasegawa, and J. K. Brown, "Investigation of the use of x-ray CT images for attenuation compensation in SPECT," *IEEE Trans Med Imaging*, vol. NS-41, pp. 2793-2799, 1994.
- [15] M. K. O'Connor, S. W. Phillips, C. B. Hruska, D. J. Rhodes, and D. A. Collins, "Molecular breast imaging: advantages and limitations of a scintimammographic technique in patients with small breast tumors," *Breast J*, vol. 13, pp. 3-11, Jan-Feb 2007.
- [16] Y. Takahashi, K. Murase, T. Mochizuki, H. Higashino, Y. Sugawara, and A. Kinda, "Segmented attenuation correction for myocardial SPECT," *Ann Nucl Med*, vol. 18, pp. 137-43, Apr 2004.

APPENDIX A: STATEMENT OF WORK

- Task 1* Design and implement a dual-modality prototype system (Months 1-17):
- Investigate effect of physical constraints (such as having the SPECT camera partially in front of the x-ray detector) on scatter contamination in reconstructed images. (Months 1-5)
 - Develop software to synchronize both systems during image acquisition. (Months 6-11)
 - Develop an ideal sequence (based on complete sampling, physical constraints) for emission and transmission data acquisition. (Months 11-12)
 - Explore 3D complex orbits with physically possible optimal orientations and tilt angles that can be used to have the system fit underneath the patient bed and still be able to image close to the chest wall. (Months 13-17)
- Task 2* Optimize CmT system by applying corrections to improve image quality (Months 18-29):
- Investigate methods to reduce circular artifacts in reconstruction from CmT images collected with a centered object and laterally offset central x-ray beam. (Months 18-22)
 - Investigate and implement scatter correction methods to CmT images. (Months 23-29)
- Task 3* Evaluate SPECT system for quantification measurements of lesion activity (Months 22-36):
- Perform image registration of SPECT and CmT images using existing image registration algorithm (i.e. surface fitting technique) with the aid of fiducial markers. (Months 22-23)
 - Investigate, implement, and compare two attenuation correction methods (i.e. uniform attenuation distribution, CmT-based attenuation distribution) to apply to SPECT data. (Months 24-30)
 - Perform SPECT quantification measurements incorporating all corrections using phantoms and lesions with known concentration activity. (Months 30-36)
- Task 4* Complete other aspects of the breast cancer training program (Months 1-36):
- Shadow a radiologist(s) to observe the clinical and diagnostic side in breast cancer imaging (Nuclear Medicine, Mammography). (Months 1-12)
 - Publish research work in peer-reviewed journals. (Months 1-36)
 - Attend and present at local seminars offered at Duke University through Medical Physics and the Breast and Ovarian Oncology Research Program, which is part of the Duke Comprehensive Cancer Center. (Months 13-36)
 - Attend international conferences such as SPIE Medical Imaging Conference, DOD BCRP Era of Hope Meeting, IEEE Medical Imaging Conference, RSNA Conference, and San Antonio Breast Cancer Symposium. (Months 13-36)
 - Prepare thesis and defend. (Months 30-36)

Development of *in vivo* characterization of breast tissues through absolute attenuation coefficients using dedicated cone-beam CT

Priti Madhav^{1,2}, Christina M. Li^{1,2}, Martin P. Tornai^{1,2}

¹ Department of Radiology, Duke University Medical Center, Durham, NC

² Department of Biomedical Engineering, Duke University, Durham, NC

ABSTRACT

With advances in 3D *in vivo* imaging technology, non-invasive procedures can be used to characterize tissues to identify tumors and monitor changes over time. Using a dedicated breast CT system with a quasi-monochromatic cone-beam x-ray source and flat-panel digital detector, this study was performed in an effort to directly characterize different materials *in vivo* based on their absolute attenuation coefficients. CT acquisitions were first acquired using a multi-material rod phantom with acrylic, delrin, polyethylene, fat-equivalent, and glandular-equivalent plastic rods, and also with a human cadaver breast. Projections were collected with and without a beam stop array for scatter correction. For each projection, the 2D scatter was estimated with cubic spline interpolation of the average values behind the shadow of each beam stop inside the object. Scatter-corrected projections were subsequently calculated by subtracting the scatter images containing only a mask of the object from corresponding projections without the beam stop array. Iterative OSTR was used to reconstruct the data and estimate the non-uniform attenuation distribution. Preliminary results show that with reduced beam hardening from the x-ray beam, scatter correction further reduces the cupping artifact, improves image contrast, and yields attenuation coefficients within 8% of narrow-beam values of the known materials (range 1.2 – 7.6%). Distinct peaks in the histogram showed clear separation between the different material attenuation coefficients. These findings indicate that minimizing beam hardening and applying scatter correction make it practical to directly characterize different tissues *in vivo* using absolute attenuation coefficients.

Keywords: tissue quantification, absolute attenuation coefficient, scatter correction, computed tomography, tomography, mammotomography, breast imaging, transmission imaging, cone-beam, iterative reconstruction

1. INTRODUCTION

With recent advances in 3D *in vivo* imaging technology, non-invasive procedures can be used to classify and quantify distinct tissues. This has been shown to be possible by taking advantage of the molecular properties of different tissue (attenuation, magnetic, and optical), which results in a noticeable image contrast between the various tissue types.¹⁻⁴ Accurate measurements of the quantification and differentiation of numerous tissues can be useful to identify disease from normalcy, as well as observe changes over time, e.g. with response to therapy.

In CT imaging, image contrast between distinct tissue components occurs due to differences in x-ray attenuation through each material. The narrower the spectral quality of the input beam, the more distinct (or higher) the contrast between tissues. For example, image contrast resulting from less x-rays attenuating through soft tissue than bone allow for both materials to be easily distinguished and visualized in an image. By quantifying different tissue components based on their attenuation characteristics, more information about the composition and distribution of the object can be gained. In addition, the CT attenuation map can be used to compensate molecular emission imaging modalities, such as SPECT or PET, for photon attenuation and absorption, making the molecular images more quantitative and spatially accurate.

However, quantifying the distribution of a adipose tissue, glandular tissue, and if present, breast carcinoma, can be a challenge in dedicated breast cone-beam CT imaging (mammotomography). This is primarily due to minimal differences between x-ray attenuation coefficient values of these materials, especially with increasing x-ray energies.¹ Physical processes during *in vivo* measurement of tissues such as beam hardening, photon scatter, sampling, and object motion

can further degrade image contrast and decrease quantitative accuracy. Beam hardening, caused by the preferential absorption of low-energy photons, and photon scatter, which is an energy dependent process, bring about cupping artifacts in the image, resulting in a reduction of the measured attenuation coefficient value towards the center of an object.⁵ In cone-beam CT particularly, the detrimental and unavoidable effect of photon scatter on quantification can also increase with wider cone-beam angles and large area 2D digital detectors.⁶ Under-sampling during acquisition and object motion causes aliasing, streaking, and blurring in the images, which in turn also affect quantification or voxel values.^{5,7}

Over the past few years, our lab has developed and characterized the intrinsic properties of a prototype hybrid SPECT-CT dedicated breast scanner and used it to image human subject volunteers.⁷ The CT sub-component of this system uses a practical quasi-monochromatic x-ray cone-beam to minimize the effect of beam hardening and improve the visualization of tissues with very small differences in attenuation coefficient values.^{1,8,9} With such a dedicated system, x-rays are only exposed to the breast and chest wall area, which limits the scatter from other areas of the body. The aim of this study is to exploit the minimal beam hardening and additionally apply scatter correction on reconstructed CT images to enhance image visualization and allow for direct *in vivo* characterization of different tissue types based on absolute attenuation coefficients. Images of a multi-material rod phantom and human cadaver breast were acquired with low-energy x-rays to maximize the contrast among the different components.¹ Scatter correction on CT projection images was performed by using a beam stop array method.^{10,11} Images were reconstructed using an iterative reconstruction algorithm yielding attenuation coefficients at corresponding voxels. Results of the measured attenuation values in the final reconstructed images are compared with actual quantities.

2. MATERIALS AND METHODS

2.1. CT system

The CT sub-system of the dual-modality SPECT-CT dedicated breast imaging system⁷ uses a rotating tungsten target x-ray source (model *Rad-94*, *Varian Medical Systems*, Salt Lake City, UT) with a 0.4/0.8mm nominal focal spot size and 14° anode angle, and a 20x25cm² field-of-view (FOV) CsI(Tl)-based amorphous silicon digital x-ray detector (model *Paxscan 2520*, *Varian Medical Systems*, Salt Lake City, UT) with a grid size of 1920x1536 pixels and 127µm pitch (Figure 1). The source and detector are secured to the same aluminum plate as the SPECT system. A custom built collimator is attached to the x-ray source to hold ultra-thick K-edge beam shaping filters to produce a quasi-monochromatic beam.¹² For these studies, 60kVp was used along with a 0.051cm cerium filter ($Z=58$, $\rho=6.77\text{g/cm}^3$, $K\text{-edge}=40.4\text{keV}$, *Santoku America, Inc.*, Tolleson, AZ). This filter reduced the exposure of the incident x-ray beam by a factor of 100 and yielded a well-characterized spectrum that had a mean energy of approximately 36keV and FWHM of 15%.^{8,9} In the current hybrid setup, the source-to-image distance (SID) is 60cm and source-to-object distance (SOD) is 38cm, resulting in a magnification of 1.57 for an object located at the system isocenter.

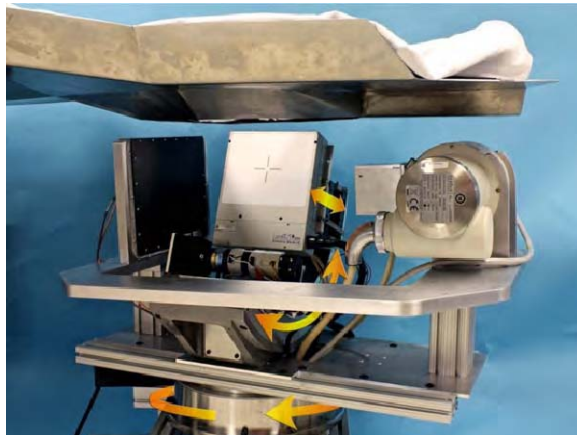


Figure 1: Photograph of the prototype dual-modality dedicated tomographic breast imaging system. The SPECT sub-system (center, back, white face) is placed orthogonally to the x-ray tube (right, front) and digital flat-panel detector (left, toward back, black face). The arrows illustrate system motions (azimuthal, polar and radius of rotation (ROR)). A customized patient bed is located above the hybrid system.

2.2. Data acquisition

To ensure that the x-ray exposure (measured in mR) was proportional to the tube current and detector pixel value, an exposure linearity test was conducted using a calibrated ionization chamber (model 1515, *Radical Corp*, Monrovia, CA). The ionization chamber was placed ~42cm from the x-ray source and orthogonal to the anode to avoid the heel effect. A range of exposures were obtained at different kVp and mAs.

Projection measurements were obtained of a multi-material rod phantom and a human cadaver breast (Figure 2). The multi-material rod phantom contained five different materials: acrylic, delrin, polyethylene (PE), and fat-equivalent and glandular-equivalent plastic rods (*Computerized Imaging Reference Systems, Inc.*, Norfolk, VA). Each rod had a length and diameter of 4.5cm and 1.9cm, respectively, and the rods were arranged in a pentagonal pattern. This phantom was placed in a cylinder with an inner length and diameter of 5.6cm and 8.2cm, respectively. Acquisitions were obtained with the cylinder filled with water. Table 1 lists the actual attenuation coefficient values at 36keV for the different materials.

The whole cadaver breast, obtained from a 48-year old woman, was placed in a breast shaped shell (nipple-to-chest distance of ~7cm, medial-to-lateral distance of ~16cm, and superior-to-inferior distance of ~18cm). Prior to imaging, the cadaver breast was clipped to the breast shell and refrigerated overnight. The next day the cadaver breast was defrosted before imaging with the CT sub-system.

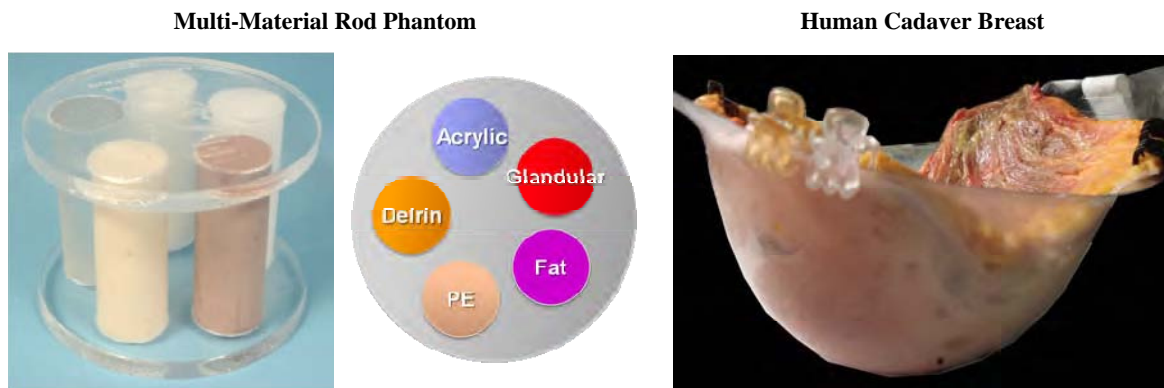


Figure 2: (Left) Photograph of the multi-material rod phantom. (Middle) Schematic of the multi-material rod phantom depicting the position of the five different materials: acrylic, delrin, polyethylene, and fat-equivalent and glandular equivalent plastic rods. (Right) Photograph of the human cadaver breast placed inside a breast shaped shell.

Table 1: Narrow beam attenuation coefficient values of the materials in the multi-material rod phantom and cadaver breast spline interpolated to 36keV

Material	Attenuation coefficient (cm ⁻¹)
Acrylic ^a	0.3136
Delrin ^a	0.3490
Fat (CIRS) ^b	0.2333
Fat (Breast Tissue) ^c	0.2284
Glandular (CIRS) ^b	0.2946
Glandular (Breast Tissue) ^c	0.3009
Polyethylene ^a	0.2285
Water ^a	0.3130

^a NIST table of x-ray mass attenuation coefficients¹³

^b Byng, Mainprize, and Yaffe¹⁴

^c Johns and Yaffe¹

For scatter correction, projections were collected with and without a custom designed beam stop array (BSA). The theory of using a BSA is that any incident x-rays striking a beam stop at this low energy will be completely stopped before reaching the detector. Consequently, the measured value in the shadow behind this beam stop should be zero (there will be a DC offset from the digital detector). However, due to the presence of scatter, the detected quantity is greater than zero. Therefore, any signal detected behind this beam stop can be assumed to be primarily due to scatter. The BSA used in this study consisted of a 10x10x0.5cm acrylic plate with 2mm diameter lead beads arranged in a square pattern, spaced 0.5cm apart (Figure 3). Several lead bead sizes and spacings were evaluated. Based on calculations and confirmation with measurements, the 2mm lead beads were thick enough to block the incident x-ray beam. The 0.5cm bead pitch was empirically determined with the goal that the shadows in the image due to the lead beads were at an adequate distance apart such that any scatter into each region would be exclusively due to scatter in that local area and not be affected by more distal surrounding beads. This BSA was attached to the front of the collimator, which was ~15cm from the x-ray source. For measurements without the BSA in place, a clear 0.5cm thick acrylic plate was attached to the front of the collimator.

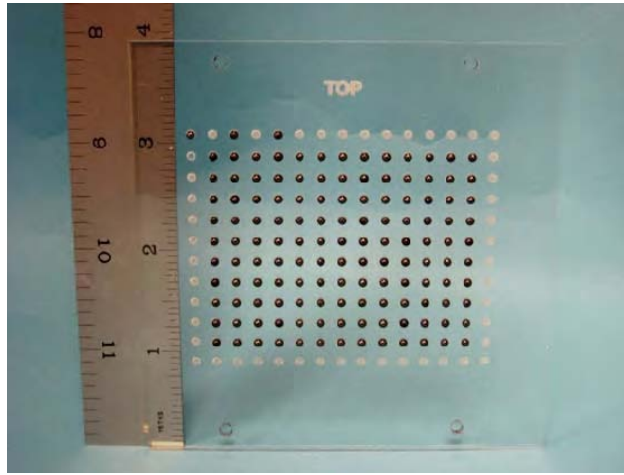


Figure 3: Photograph of the beam stop array with 2mm lead beads that was placed in front of the collimator (~15cm from the x-ray source) for scatter measurements.

Both the multi-material phantom and the cadaver breast were placed at the system's center of rotation. Tube potential was set at 60kVp with a 3.2mAs technique per projection. Using the ionization chamber, the x-ray exposure was linear to the tube current and detector pixel value. Projection images were collected every 1.5° through a 360° azimuthal circular acquisition, for a total of 240 projections. The total scan time for each acquisition was 6min.

For the multi-material rod phantom, additional experiments were done using a custom-built 4-jaw collimator.^{15, 16} This consisted of two vertical and two horizontal lead plates that could be moved to allow further collimation of the beam. The vertical collimator jaws were adjusted to five different positions including: (1) full FOV with no additional collimation, (2) vertical collimation to include only the cylinder with the phantom, (3) vertical collimation to include only the rods of the phantom; (4) vertical collimation to include only the bottom half of the rods of the phantom (flat part of the cone-beam intersects in this area to give the most complete sampling⁷); and (5) vertical collimation to include only 2mm jaw slot width of the rods to approximate narrow-beam geometry.

2.3. Scatter correction algorithm

A flow chart describing the scatter correction algorithm is presented in Figure 4. As mentioned in the previous section, a complete set of CT projections was obtained for each object without and with the BSA. The scatter correction algorithm was written in MATLAB (*The Mathworks, Inc.*, Natick, MA). From a CT projection with only the BSA in the FOV, the location of all the lead beads was found. In addition, for each projection, a mask of the object was automatically created by thresholding using a k-means algorithm. Next, the amount of scatter in all projections was measured using images with the BSA and object in the FOV. In this step, an average scatter value was measured over a 5x5pixel ROI in each lead bead localized inside the object. For each row containing the lead beads, the average scatter values were extrapolated using a cubic spline to obtain a single scatter measurement near the boundaries at both ends of the object.

This was repeated for each column with the lead beads. After the extrapolation along each row and column was completed, a 2D cubic spline interpolation was done to obtain a 2D scatter profile over the entire projection image. This profile was subtracted from projection images without the BSA to obtain final projection images with minimal scatter.¹⁰

In addition, this study also looked at the effect on reconstructed images by obtaining scatter measurements from only a few projections rather than all 240 projections. In this case, after the 2D scatter profiles for evenly spaced projections were measured, a 3D cubic spline interpolation between the measured azimuthal angles was performed to obtain the 2D scatter maps for all projections.

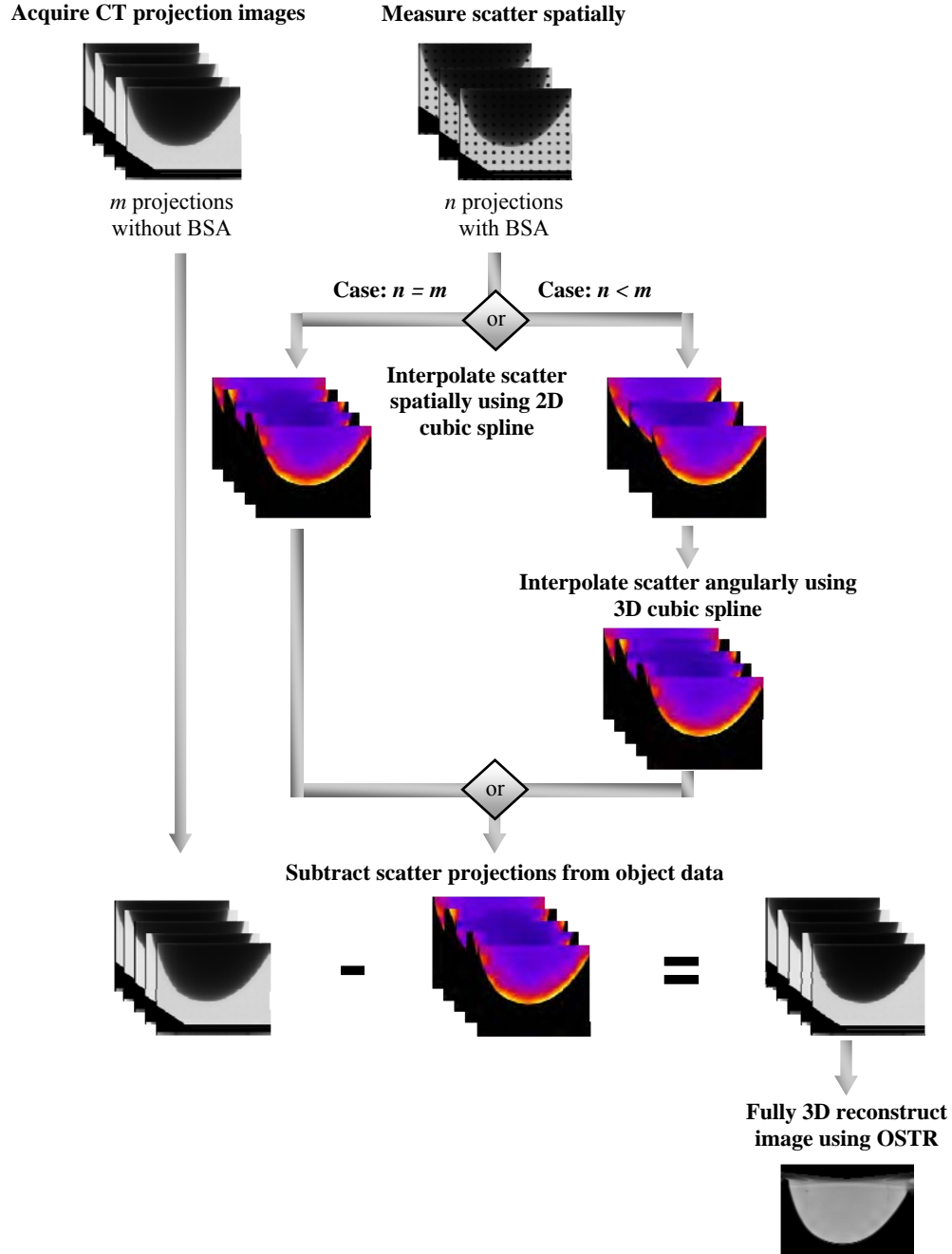


Figure 4: Flow chart of the algorithm used to correct for scatter in the CT projection images.

2.4. Reconstruction

Image reconstruction was performed on the CT projection images by increasing the log likelihood via the iterative ordered-subset transmission reconstruction algorithm (OSTR)¹⁷, using a ray-driven image reconstruction code, CT-MAP.¹⁸ Projection images were corrected for gain and offset and binned to 4×4 pixels. Reconstruction parameters were set to 10 iterations, 16 subsets, a $350 \times 350 \times 384$ reconstruction grid and a $508 \mu\text{m}$ voxel size. The total reconstruction time in this iterative framework was 4 hours. A 3D Hann filter was applied to smooth and reduce noise in the final reconstructed images.

2.5. Data analysis

In the final reconstructed images, line profiles were plotted and compared. Additionally, ROIs were drawn over each of the five rods in the multi-material rod phantom and over regions containing the fat and glandular tissue in the cadaver breast to determine the average attenuation value. Based on the actual attenuation value presented in Table 1, the percentage error was calculated. For the multi-material rod phantom, contrast measurements were also obtained between the rods and background. Image histograms were also obtained and compared for the cadaver breast.

3. RESULTS AND DISCUSSION

3.1. Multi-material rod phantom

3.1.1. Scatter correction

Figure 5 compares the reconstructed images of the multi-material rod phantom before and after scatter correction. From these images, all five rods can be seen. However, the line profiles clearly show that the contrast between the rods and the background, which in this case is water, is higher in the scatter-corrected reconstructed images. This indicates that since water and “glandular equivalent” plastic values are similar, water can be used as a reasonable substitute for hard plastic tissues in phantoms. In addition, the outer thickness of the acrylic cylinder holding the phantom can also be clearly distinguished in the scatter-corrected data. Absolute values from the contrast measurements are presented in Table 2.

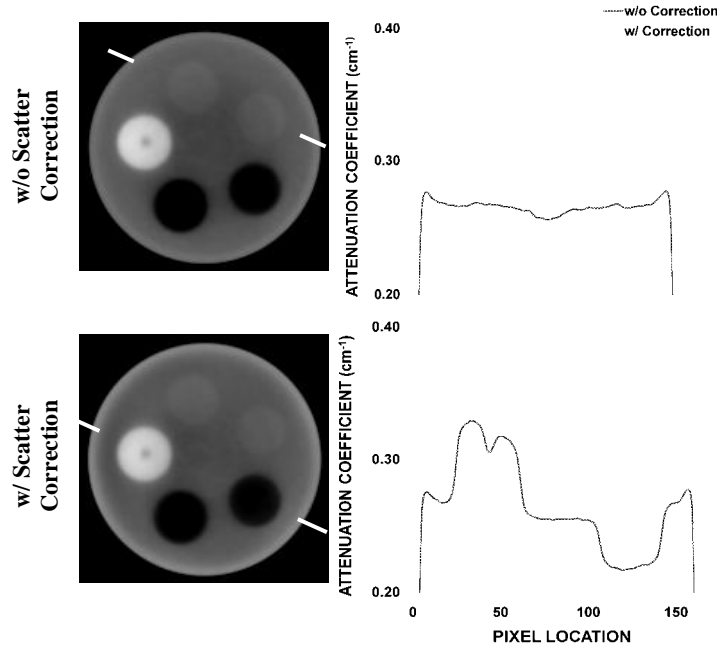


Figure 5: Reconstructed slices of the multi-material rod phantom (Top Left) without and (Bottom Left) with scatter correction. The material of each rod corresponds to the schematic shown in Figure 2, Middle. (Right) Line profiles taken across the phantom (between white hash marks) through the (Top Right) acrylic and glandular-equivalent rod and (Bottom Right) delrin and fat-equivalent rod.

Table 2: Contrast measurements for each material obtained with and without scatter corrected reconstructed images

Material	w/o Scatter Corrected Contrast	w Scatter Corrected Contrast
Acrylic 0.003		0.004
Delrin	0.205	0.215
Fat 0.170		0.211
Glandular	0.003	0.006
PE 0.195		0.218

The mean attenuation values were also measured and compared to the actual values. The small hollow center that was seen in the delrin rod (Figure 5) was excluded from these calculations. The percentage error in Table 3 shows that the implemented scatter correction also helps to align the overall measured attenuation coefficient to its true value.

Table 3: Measured attenuation values and % error for each material obtained with and without scatter corrected reconstructed images

Material	w/o Scatter Corrected Attenuation Value (cm ⁻¹)	% Error	w/ Scatter Corrected Attenuation Value (cm ⁻¹)	% Error
Acrylic	0.2659 15.2	0.3079		1.8
Delrin	0.3196	8.4 0.3755	7.6	
Fat	0.2200	5.7 0.2440	4.6	
Glandular	0.2644 10.3	0.3110		5.6
PE	0.2136	6.5 0.2417	5.8	
Water	0.2652 15.3	0.3091		1.2

3.1.2. Narrow cone-beam imaging geometry

The 4-jaw collimator was adjusted to four different views: (1) full FOV, (2) only the cylinder with the phantom, (3) only the rods of the phantom; (4) only the bottom half of the rods of the phantom; and (5) only 2mm jaw slot width of the rods. Table 4 shows that as the FOV is decreased and therefore the amount of scatter present in the reconstructed images is also decreased, the accuracy of the reconstructed attenuation coefficients greatly improves. This is consistent with others' measurements that have shown that with larger cone-beam angles and FOVs, scatter increases.⁶

Table 4: Measured attenuation values and % error for each material for the five different cases with the 4-jaw collimator

Material	Full Field-of-View		Cylinder		Full Rods		Bottom Half of Rods		2mm Width of Rods	
	Attenuation Value (cm ⁻¹)	% Error	Attenuation Value (cm ⁻¹)	% Error	Attenuation Value (cm ⁻¹)	% Error	Attenuation Value (cm ⁻¹)	% Error	Attenuation Value (cm ⁻¹)	% Error
Acrylic	0.2673 14.8		0.2693	14.1	0.2773	11.6	0.2902 7.5		0.2901 7.5	
Delrin	0.3233	7.4	0.3260	6.6	0.3373	3.4 0.3578	2.5 0.3638		4.3	
Fat 0.2190		6.2	0.2204	5.5	0.2258	3.2 0.2287	2.0 0.2374		1.8	
Glandular	0.2646 10.2		0.2664	9.6	0.2742	7.0 0.2855	3.1 0.2901		1.5	
PE 0.2131		6.8	0.2144	6.2	0.2196	3.9 0.2215	3.1 0.2303		0.8	
Water	0.2655 15.2		0.2672	14.6	0.2743	12.4	0.2834 9.5		0.2854 8.8	

A collimator opening of 2mm (vertically), which approximated fan-beam imaging geometry, results in the least scatter in these conditions, and therefore can be assumed to produce more accurate reconstructed images. With a narrower beam, less than 10% percent error was measured between the actual and measured attenuation coefficients, and these values are similar to the scatter-corrected cases (compare values in Table 3).

3.2. Cadaver breast

Reconstructed slices of the cadaver breast are shown in Figure 6. In the image before scatter correction, the center appears darker. Since the effect of beam hardening is reduced with the use of a quasi-monochromatic x-ray beam, it can be assumed that this cupping is primarily due to scatter. The image after scatter correction appears to be more uniform. This is confirmed in the line profile through the breast which clearly illustrates that the cupping artifact is minimized with scatter correction. Cupping was probably not visible in the multi-material rod phantom since the physical size of this object is smaller than the cadaver breast resulting in less scatter. In addition, the contrast between the glandular tissue, fat, and skin appears to be improved (images are displayed on the same absolute gray scale). The line profiles also show there is very minimal difference between the two scatter-corrected reconstructed images: one obtained using all 240 BSA-cadaver breast projections and the other obtained using only six equally spaced BSA-cadaver breast projections. This is important since in practice scatter measurements with the BSA will not be obtained for all 240 projections since this would double the amount of dose given to the patient. Scatter measurements will most likely be obtained when acquiring a few scout images to assure that the breast is at the center of rotation and/or during the acquisition itself with the BSA moved into place.

An image histogram from a section of the breast shows that for both cases with scatter correction, glandular tissue and fat are distinctly separated into two distributions. With the histogram obtained from the non-scatter-corrected data, it is difficult to distinguish between the two different tissues, though one might assume that there are two underlying distributions.¹⁹ Most likely due to scatter, the peaks for both tissues are broader and merge into an asymmetric distribution in the case of our quasi-monochromatic x-ray beam. The image histogram of the scatter-corrected data has narrower peaks with values that are closer to the true attenuation value of fat and glandular tissue (Table 1). ROIs drawn over fat and glandular tissues showed once again that scatter correction can improve the attenuation value to within 10% of its actual value (Table 5).

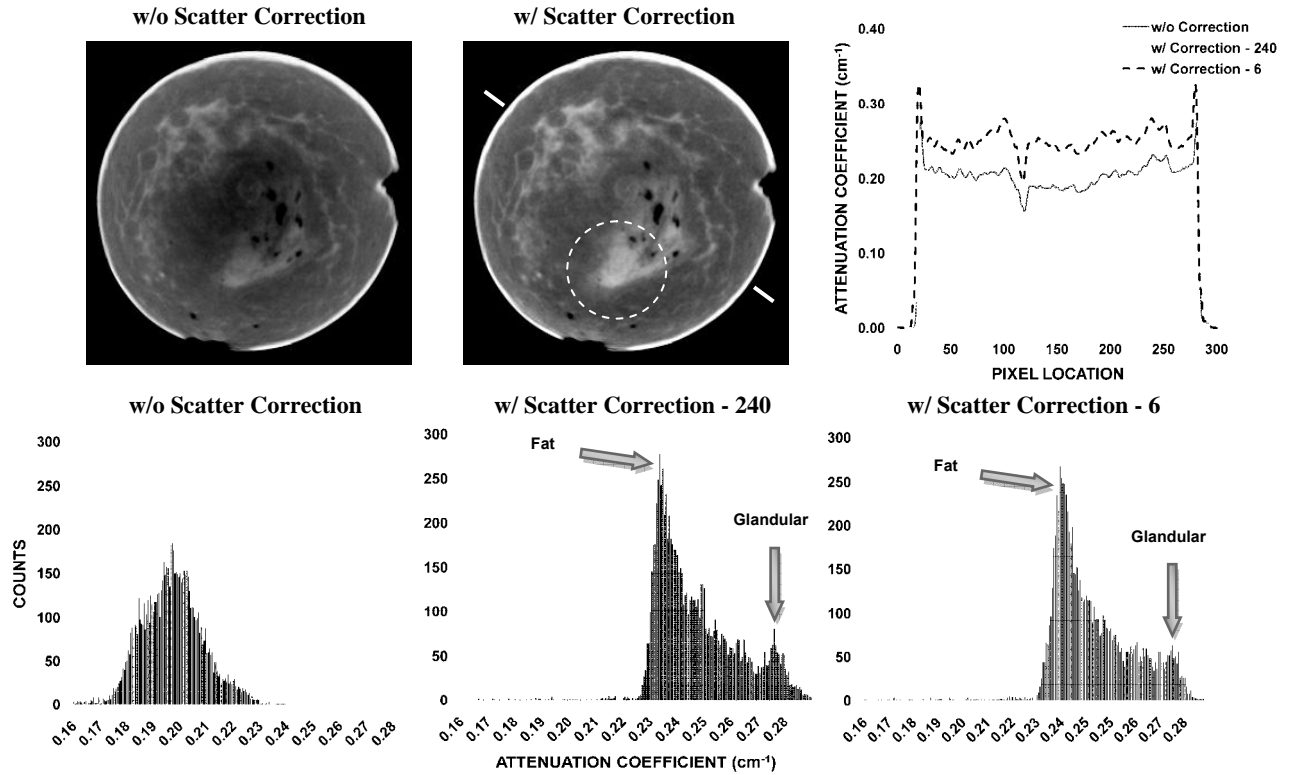


Figure 6: (Top) Reconstructed slices of the cadaver breast (Top Left) without and (Top Middle) with scatter correction. (Top Right) Line profile obtained across the cadaver breast (between white hash marks) without and with scatter correction. (Bottom) Image histograms obtained from a section of the breast (inside dashed circle).

Table 5: Measured attenuation values and % error of fat and glandular tissue in the cadaver breast obtained with and without scatter corrected reconstructed images

Material	w/o Scatter Corrected Attenuation Value (cm ⁻¹)	% Error	240 projections		6 projections	
			w/ Scatter Corrected Attenuation Value (cm ⁻¹)	% Error	w/ Scatter Corrected Attenuation Value (cm ⁻¹)	% Error
Fat 0.1873		18.0	0.2321	1.6	0.2340	2.5
Glandular	0.2148	28.6	0.2793	7.2	0.2775	7.8

4. CONCLUSION

This study showed that minimizing beam hardening and correcting for scatter can minimize cupping artifacts, improve intrinsic material contrast, and yield image values closer to the actual attenuation value of a material. Results showed that scatter-corrected data yielded attenuation values within 8% (range from 1.2 to 7.6%) of the actual attenuation coefficients. This improvement for cone-beam CT with scatter correction was similar to the case with narrow-beam collimation, which had the least scatter effect. The comparison results with narrow-beam imaging indicate that not only does the implemented scatter correction effectively minimize degradation due to scatter in the final reconstructed images, but also that measured scatter corrected attenuation values are nearly identical to narrow-beam values, leading to the possibility of true *in vivo* tissue characterization with dedicated breast CT. In addition, image histograms clearly differentiated the different materials in the scatter-corrected reconstruction images, whereas the results were ambiguous in the uncorrected images, even though the intrinsic beam is already quasi-monochromatic. This allows for the possibility to differentiate between normal glandular tissue and diseased tissue in the breast, given that they have intrinsically different attenuation characteristics. Given the high quantitative fidelity, this cone-beam imaging approach could possibly be used for *in vivo* tissue characterization. Lastly, contrast and attenuation coefficient quantification appears to be preserved even by taking scatter measurements from only a few projections, making this approach practicable in a clinical environment.

One next step with the hybrid breast imaging system will be to use the final CT scatter-corrected reconstructed images to correct for attenuation in the SPECT images in order to improve quantification of radiotracer uptake. Also, with the current dual-modality prototype, the CT sub-system is restricted to only circular motion around the breast. Previous studies have shown that a dedicated breast CT system moving in non-traditional acquisition trajectories can improve object sampling and simultaneously image more of the breast volume compared to acquisitions using a simple circular orbit.^{7,15} Studies will be done to see if better sampling can also improve CT tissue quantification further.

ACKNOWLEDGEMENTS

The authors would like to thank Dr. E. Samei and N. Ranger for the use of their ionization chamber, and O. Christianson, S. Earp, and J. Owen for their assistance at the machine shop.

This work is supported by NIH grant RO1-CA096821, and partly by DOD grants W81XWH-06-1-0791 and W81XWH-06-1-0732. MPT is the inventor of this hybrid breast imaging technology, and is named as an inventor on the patent for this technology assigned to Duke (US Pat. #7,609,808). If this technology becomes commercially successful, MPT and Duke could benefit financially.

REFERENCES

- [1] P. C. Johns and M. J. Yaffe, "X-ray characterization of normal and neoplastic breast tissues," *Phys. Med. Biol.* **32**, 675-695 (1987).
- [2] N. Mitsopoulos, R. N. Baumgartner, S. B. Heymsfield, et al., "Cadaver validation of skeletal muscle measurement by magnetic resonance imaging and computerized tomography," *J Appl Physiol* **85**, 115-122 (1998).

- [3] J. Machann, C. Thamer, B. Schnoedt, et al., "Standardized assessment of whole body adipose tissue topography by MRI," *J Magn Reson Imaging* **21**, 455-462 (2005).
- [4] V. Chernomordik, D. W. Hattery, D. Grosenick, et al., "Quantification of optical properties of a breast tumor using random walk theory," *J Biomed Opt* **7**, 80-87 (2002).
- [5] J. F. Barrett and N. Keat, "Artifacts in CT: Recognition and Avoidance," *Radiographics* **24**, 1679-1691 (2004).
- [6] J. H. Siewerdsen and D. A. Jaffray, "Cone-beam computed tomography with a flat-panel image: magnitude and effects of x-ray scatter," *Med Phys* **28**, 220-231 (2001).
- [7] P. Madhav, D. J. Crotty, R. L. McKinley and M. P. Tornai, "Evaluation of tilted cone-beam CT orbits in the development of a dedicated hybrid mammothomograph," *Phys Med Biol* **54**, 3659-3676 (2009).
- [8] R. L. McKinley, M. P. Tornai, E. Samiei and M. L. Bradshaw, "Simulation study of a quasi-monochromatic beam for x-ray computed mammothomography," *Med. Phys.* **31**, 800-813 (2004).
- [9] D. J. Crotty, R. L. McKinley and M. P. Tornai, "Experimental spectral measurements of heavy K-edge filtered beams for x-ray computed mammothomography," *Phys Med Biol* **52**, 603-616 (2007).
- [10] J. Y. Lo, C. E. F. Jr, J. A. Baker and C. E. Ravin, "Scatter compensation in digital chest radiography using the posterior beam stop technique," *Med. Phys.* **21**, 435-443 (1994).
- [11] W. Cai, R. Ning and D. Conover, "Scatter correction using beam stop array algorithm for cone-beam CT breast imaging," 2006 SPIE Medical Imaging Conference **6142**, (2006).
- [12] R. L. McKinley, M. P. Tornai, E. Samiei and M. L. Bradshaw, "Initial study of quasi-monochromatic beam performance for x-ray computed mammothomography," *IEEE Trans. Nucl. Sci.* **52**, 1243-1250 (2005).
- [13] J. H. Hubbell and S. M. Seltzer, "Tables of x-ray mass attenuation coefficients and mass energy-absorption coefficients 1keV to 20MeV for elements Z=1 to 92 and 48 additional substances of dosimetric interest," *Journal* (1996).
- [14] J. W. Byng, J. G. Mainprize and M. J. Yaffe, "X-ray characterization of breast phantom materials," *Phys Med Biol* **43**, 1367-1377 (1998).
- [15] R. L. McKinley, C. N. Brzymialkiewicz, P. Madhav and M. P. Tornai, "Investigation of cone-beam acquisitions implemented using a novel dedicated mammothomography system with unique arbitrary orbit capability," 2005 Proc SPIE: Phys Med Imag **5745**, 609-617 (2005).
- [16] M. P. Tornai, R. L. McKinley, C. N. Brzymialkiewicz, et al., "Design and development of a fully-3D dedicated x-ray computed mammothomography system," 2005 SPIE Med Imag Conf **5745**, 189-197 (2005).
- [17] H. Erdogan and J. A. Fessler, "Ordered subsets algorithms for transmission tomography," *Phys Med Biol* **44**, 2835-2851 (1999).
- [18] J. E. Bowsher, M. P. Tornai, J. Peter, et al., "Modeling the axial extension of a transmission line source within iterative reconstruction via multiple transmission sources," *IEEE Trans Med Imaging* **21**, 200-215 (2002).
- [19] T. R. Nelson, L. I. Cervino, J. M. Boone and K. K. Lindfors, "Classification of breast computed tomography data," *Med Phys* **35**, 1078-1086 (2008).

Towards Quantification of Dedicated Breast SPECT Using Non-Traditional Acquisition Trajectories

Kristy L. Perez *IEEE Student Member*, Spencer J. Cutler *IEEE Student Member*, Priti Madhav *IEEE Student Member*, Martin P. Tornai *IEEE Senior Member*

Abstract- Quantification of radiotracer uptake in lesions can provide valuable information to physicians in deciding patient care or determining treatment efficacy. Physical processes (e.g. scatter, attenuation), detector/collimator characteristics, sampling and acquisition trajectories, and reconstruction artifacts contribute to an incorrect absolute measurement of tracer activity and distribution. For these experiments, a cylinder with three syringes of varying radioactivity concentration, and a fillable 800mL breast with two lesion phantoms containing aqueous ^{99m}Tc pertechnetate were imaged using the SPECT sub-system of the dual-modality SPECT-CT dedicated breast scanner. SPECT images were collected using a compact CZT camera with various 3D acquisitions including vertical axis of rotation, 30° tilted, and complex sinusoidal trajectories. Quantitative differences in the measured absolute activity values were investigated for each acquisition trajectory to determine the efficacy of an acquisition trajectory to quantify regions of focal uptake. With attenuation and scatter corrections applied, reconstruction image results showed that the measured average activity concentrations in the hot-spot areas corresponded to within 15% of the actual dose calibrator measured activity concentration. More complete sampling trajectories outperform incomplete tilted acquisition trajectories.

I. INTRODUCTION

Quantification is not common for routine SPECT imaging. Generally, nuclear medicine physicians rely on differences in relative radioactive tracer uptake patterns to analyze molecular SPECT images. Quantification of the radioactive uptake in the images requires careful application of data corrections. Because radiotracers can be designed to label metabolic processes, receptors, and the like, their absolute *in vivo* quantification of concentration could be a valuable diagnostic tool to differentiate between benign and malignant tissue. Particularly in breast cancer patients, distinguishing absolute *in vivo* quantification via non-invasive molecular imaging could affect a patient's treatment plan.

There are a variety of physical factors that can affect the quantification in SPECT images [1]. These include photon attenuation and scatter which have both been shown to degrade images and hence, various methods have been proposed to correct for these. Attenuation correction relies on obtaining a spatial distribution of attenuation coefficients to model the imaged object, often derived from computed tomography (CT) data, and compensates for non-uniform

attenuation. There have been many scatter correction techniques derived over time. For ^{99m}Tc imaging, the Jaszczak or Compton Window Method uses an energy window abutting the photopeak, but lower in energy, to estimate the scatter fraction in the photopeak [2].

Additionally, corrections for system factors, such as the detector, collimator and geometric efficiencies, must be incorporated. These efficiencies scale detected and recorded events to the actual volumetric activity at the time of imaging.

Other groups have investigated quantitative breast imaging using planar single photon imaging techniques [4,5] and have shown that quantification of size and uptake has implications for staging disease [4]. In spite of this, due to the nature of planar imaging, it becomes difficult to correctly quantify smaller volumes. SPECT can localize the disease in 3D space and quantify its absolute radiotracer uptake without added activity from "normal" background tissue [1]. Because our dedicated SPECT system has a fully 3D range of motion, we are able to sample into the chest wall and axilla of the breast [6].

In this study, quantification is implemented on our dedicated SPECT to test the system's linearity in measuring radiotracer uptake. In particular, the effect of data acquired with non-traditional, non-circular trajectories on absolute quantification of SPECT data is observed.

II. METHODS

A. Gamma Camera and Data Acquisition

The SPECT sub-system of the hybrid imaging device consists of a Cadmium-Zinc-Telluride (CZT) *LumaGEM* 3200STM gamma camera (*Gamma Medica Inc.*, Northridge, CA) that has 2.3x2.3 mm crystals with a 6.7% intrinsic FWHM at 140 keV and a sensitivity of 37.9 cps/MBq (Fig. 1). The lead parallel hole collimator has 1.22 mm flat-to-flat hexagonal holes with 0.2 mm septa and is 25.4 mm in height. The camera system is attached to precision positioning motors to permit movement in 3D to contour the breast surface by moving in and out, up and down and around the center of rotation. Previous work has defined a set of trajectories which maximize the volume of the object imaged [6].

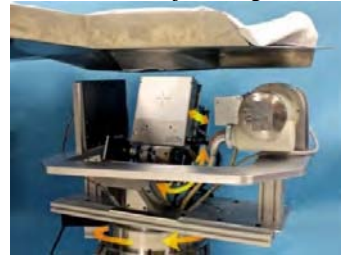


Fig. 1. Hybrid SPECT-CT breast imaging device. Orange and yellow arrows indicate the directions of movement of the SPECT camera (center).

Manuscript received November 13, 2009. This work has been funded by the National Cancer Institute of the National Institutes of Health (R01-CA096821) and the Department of Defense Breast Cancer Research Program (W81XWH-08-1-0192, W81XWH-06-1-0765 and W81XWH-06-1-0791).

KLP and MPT are with the Medical Physics Program and Radiology Department, Duke University, Durham, NC 27710 USA (telephone: 919-684-7943, e-mail: kristy.perez@duke.edu).

SJC, PM and MPT are with Biomedical Engineering and Radiology Departments, Duke University, Durham, NC 27710 USA.

B. Model System in Reconstruction Code

A flow chart outlining the steps for quantifying data with this system appears in Figure 2. Image reconstruction was performed using a ray-driven, iterative ordered-subsets expectation maximization (OSEM) reconstruction code [3]. Collimator, geometry and detection efficiencies of the SPECT camera, radiopharmaceutical half-life, and attenuation and scatter correction maps were included in the reconstruction algorithm.

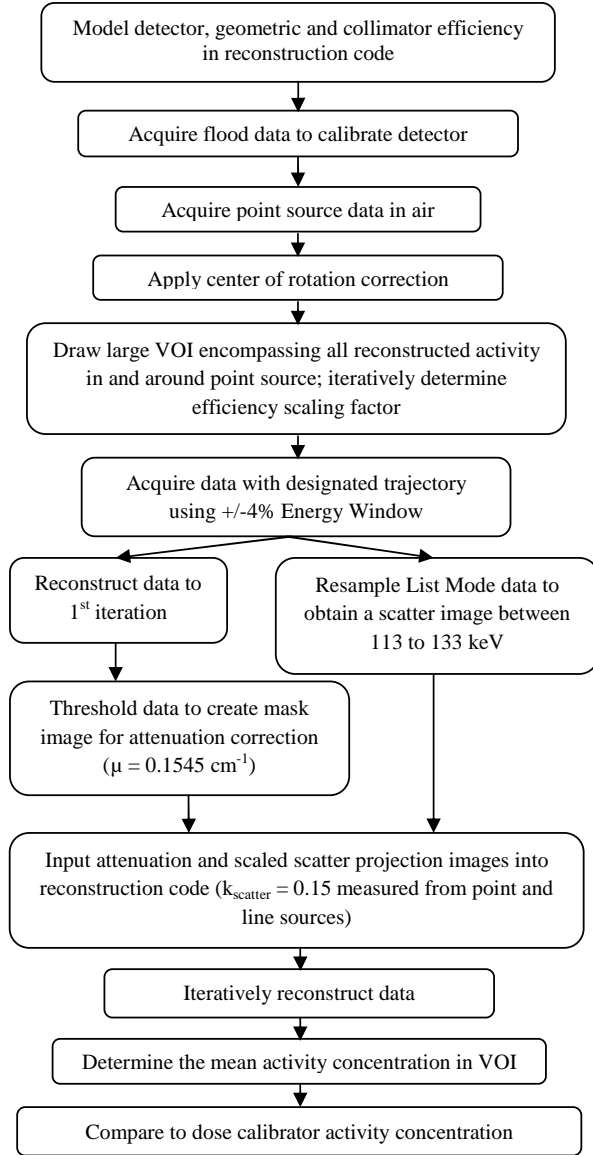


Fig 2. Flowchart of the steps to correct data for quantification.

To find the reconstruction scaling coefficient, two 0.7 mL balloons (*Harvard Apparatus*, Holliston, MA) filled with 125.5 and 115.5 μCi of $^{99\text{m}}\text{Tc}$ pertechnetate in 0.5 and 0.4 mL were suspended at and off the center of rotation, respectively, in a 12.5 cm diameter cylinder and were imaged with a simple circular, vertical axis of rotation (VAOR) acquisition

trajectory in air. All reconstructed slices containing the point sources were summed and a region of interest was drawn encompassing all counts in the image. Equation 1 is used to determine the total activity in the reconstructed image which is compared to the dose calibrator measured activity.

$$A_{\text{tot}} = \sum_i \left[\left(\frac{A}{V} \right)_i V_i \right] \quad (1)$$

Where A_{tot} is the total activity in the cumulative volume of interest, i is the voxel number, A/V is the reconstructed voxel value and V is the reconstructed voxel volume. The reconstruction scaling coefficient was determined by the ratio of the measured activity concentration in the image to dose calibrator activity.

To determine the iteration at which the measured activity concentrations in the reconstructions vary the least, the data set of syringes in air was reconstructed with 8 subsets up to 100 iterations. The mean value (units of microcuries per milliliter) in a region of interest (ROI) in the reconstructed image was determined every 5 iterations for up to 100 iterations to determine the iteration where convergence is reached.

C. Geometric & Anthropomorphic Phantoms

1) Linearity Test

Three 30 mL syringes were filled with ~10 mL of clinical concentrations of aqueous $^{99\text{m}}\text{Tc}$ pertechnetate. The syringes were placed in a 12.5 cm diameter cylinder (Fig. 3) and imaged in air, and then in water, and water plus background activity. The initial radioactive concentrations, measured with a calibrated dose calibrator (CRC-30BC, *Capintec, Inc.*, Ramsey, NJ), are given in Table I.

TABLE I: INITIAL RADIOACTIVITY AND ACTIVITY CONCENTRATION IN SYRINGES AND CYLINDER.

	Activity (μCi)	Volume (mL)	Activity Conc ($\mu\text{Ci/mL}$)
Syringe 1	34.7	9.7	3.6
Syringe 2	113.3	10	11.3
Syringe 3	226.8	11	20.6
Background	386.8	900	0.430

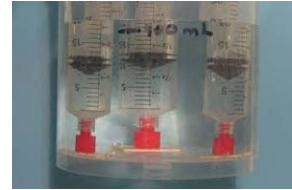


Fig. 3. Photograph of syringes with varying concentrations of radioactivity in a cylinder with an aqueous uniform radioactive background.

2) Breast & Lesion Phantoms

An 800 mL anthropomorphic breast phantom containing a 2.3 mL acrylic-walled sphere (*Radiological Service Devices Inc.*, Newport Beach, CA) and a 1.6 mL thin-walled balloon (*Harvard Apparatus*, Holliston, MA) were filled with aqueous $^{99\text{m}}\text{Tc}$ pertechnetate (Fig. 4). Table II gives the initial

radioactive concentrations, measured with a dose calibrator, of the spheres and background.

TABLE II: INITIAL RADIOACTIVITY AND ACTIVITY CONCENTRATION OF THE SPHERES AND BREAST PHANTOMS.

	Activity (μCi)	Volume (mL)	Activity Conc ($\mu\text{Ci/mL}$)
Acrylic	28.4	2.3	12.3
Balloon	19.8	1.6	12.4
Background	222.6	765	0.291

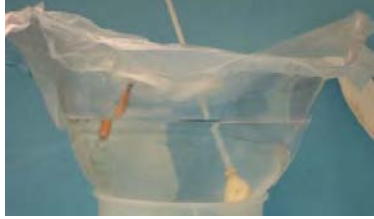


Fig. 4. Photograph of the acrylic (left) and balloon (right) spheres in the anthropomorphic breast phantom filled with 765 mL of water.

D. Data Acquisition

For this data, 128 projection images collected over 360° with vertical axis of rotation (VAOR), 30° tilted parallel beam (TPB) and projected sinusoidal (PROJSINE) ranging from 15° to 45° polar tilt, paths (Fig. 5) were compared for quantification accuracy. The data was collected with a $\pm 4\%$ photopeak energy window centered about 140 keV.



Fig. 5. 3D trajectories (yellow path) of the gamma camera (blue box) used to acquire data.

E. Attenuation and Scatter Corrections

We assumed a uniform emission volume to correct for signal loss due to photon attenuation. A map of the attenuation coefficients was defined by reconstructing the data to the first iteration, thresholding the image to obtain the mask of the object, and assigning each pixel a constant attenuation coefficient for water, 0.1545 cm^{-1} [7]. The original data is then reconstructed a second time implementing the uniform attenuation map along with the following scatter corrections in the reconstruction algorithm.

For scatter correction, the Compton Window Method estimates the percentage of scatter in the photopeak with a lower energy scatter window scaled by a proportionality constant, k [2]. Because a $\pm 4\%$ symmetric photopeak window ranging from 134 to 146 keV was used, we chose to center the scatter window around an energy that produced a window abutting the photopeak window: $123 \text{ keV} \pm 8\%$, ranging from 113 to 133 keV. Following the methods outlined in [2], we iteratively empirically determined k to be 0.15, consistent with previous measures in our lab.

F. Reconstruction

The original data was reconstructed a second time implementing the attenuation and scatter correction maps. For qualitative visual purposes and quantitative observer studies, previous studies have shown that with eight subsets the 2nd iteration gives the best SNR and contrast values [8]. To determine the optimal iteration point for quantification purposes, the image set of the syringes in air was reconstructed with eight subsets up to 100 iterations with the OSEM reconstruction code [3]. A reconstruction grid size of $150 \times 150 \times 150$ was used. The isotropic voxel size was selected to be the same as the detector pixel size, with 2.5 mm on each side. Thus, gray scale values of the reconstructed images are output in absolute $\mu\text{Ci/mL}$ units.

G. Data Analysis

Three sagittal slices of the final converged reconstructed images were summed and ROIs were drawn in the syringe/lesions and backgrounds. ROIs for the syringes were completely within and not close to the edges of the syringes to avoid partial volume edge effects. The mean, decay corrected, reconstructed image activity concentration was determined and compared with the dose calibrator measured activity concentration. The percent difference was calculated to determine the accuracy of the reconstruction process.

III. RESULTS & DISCUSSION

A. Convergence of Activity Concentration Value

The plot in Figure 6 shows that for 8 subsets, the 20th iteration will provide information that is near convergence for each trajectory.

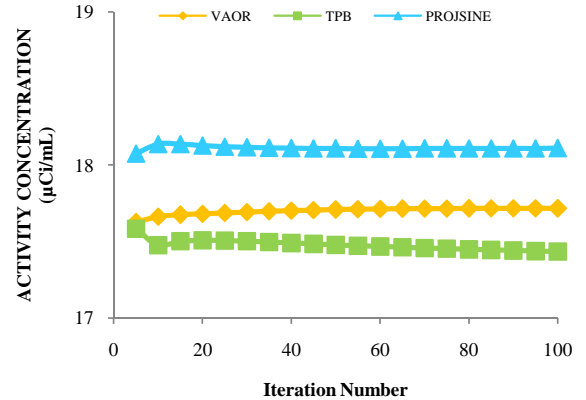


Fig. 6. Plot of mean activity concentration in an ROI as a function of iteration number. Iteration 20 was determined to be a good compromise for convergence for each of the trajectories.

B. Linearity

The reconstructed data shows evident differences in contrast between the variety of activity concentrations (Fig. 7). The decay corrected, mean activity concentration has good agreement with “known” values (Fig. 8). The “known” values are determined from dose calibrator measurements, which are considered as the gold standard. The results indicate that the accuracy has some dependence on both activity concentration

and acquisition trajectory. For lower activity concentrations, the accuracy is worse than for greater amounts of activity (Table III). Generally, the accuracy is better than 15% for activity concentrations $>3\mu\text{Ci/mL}$. For the data with water plus radioactive background, the variability between scans is generally less than 10% for all three acquisition trajectories.

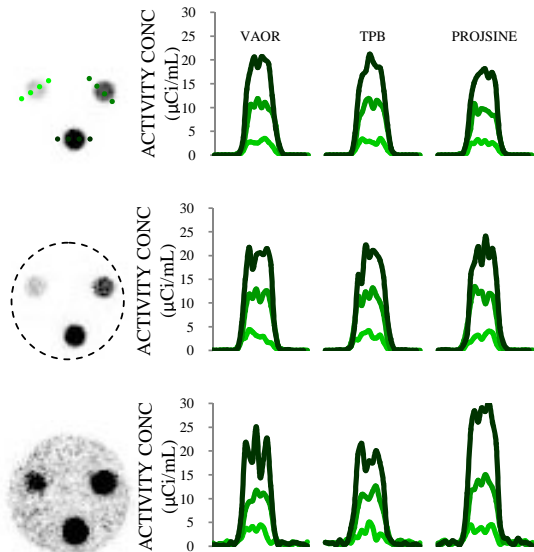


Fig. 7. Average of seven summed reconstructed slices of syringes in air (TOP, LEFT), water (MIDDLE, LEFT) and aqueous radioactivity background (BOTTOM, LEFT) acquired with a VAOR trajectory; images from other trajectories look similar. Three pixel line profiles (RIGHT) through each syringe for each acquisition.

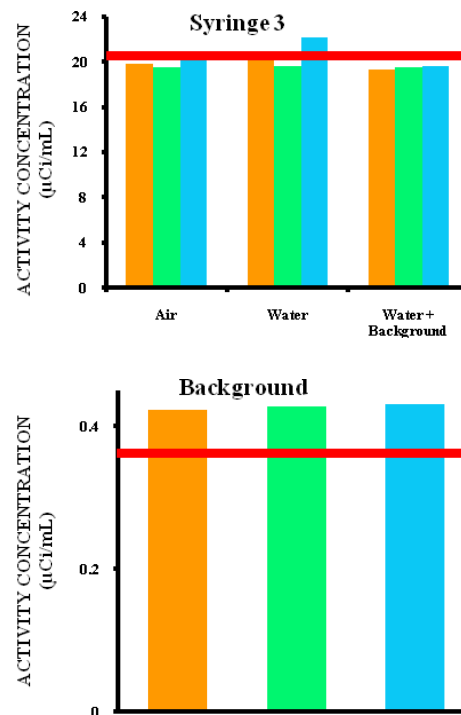
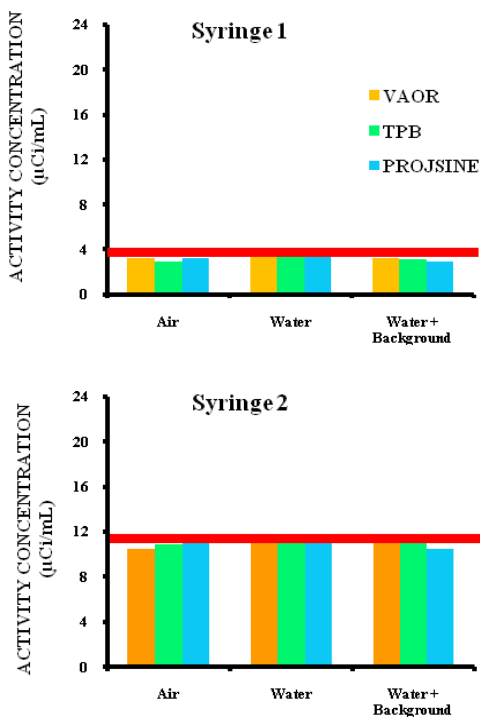


Fig. 8. Bar charts of dose calibrator (red lines) and decay corrected image measured activity concentrations for syringes 1, 2, and 3, and background.

TABLE III: PERCENT DIFFERENCE OF SYRINGES IN AIR FOR EACH ACQUISITION TRAJECTORY.

	% Difference		
	Syringe 1	Syringe 2	Syringe 3
VAOR	9.14	7.38	3.7
TPB	17.2	4.22	5.45
PROJSINE	8.84	3.36	0.4

C. Breast & Lesion

VAOR and PROJSINE spherical lesion data are accurate to within 15%, while TPB data have consistently greater than 30% deviation from the actual dose calibrator measured concentration (Fig. 10). Because the TPB data is insufficiently sampled, elongation artifacts in the reconstructed images distort the shape of the breast and lesions, dispersing the activity into a greater image volume. Additionally, there is an attenuation map inconsistency given the elongation artifact and the known, smoothly varying, true phantom distribution. Therefore, the total activity is dispersed over the larger volume, and consequently the activity concentration reported in each voxel decreases, as evident in the images set to the same global maximum in Figure 9.

The accuracy of measuring the background concentration varies greatly (Fig. 10), due to the relatively poor counting statistics of the low activity area.



Fig. 9. MIP images of reconstructed data set to a global maximum containing acrylic (top) and thin-walled (bottom) radioactive lesion phantoms.

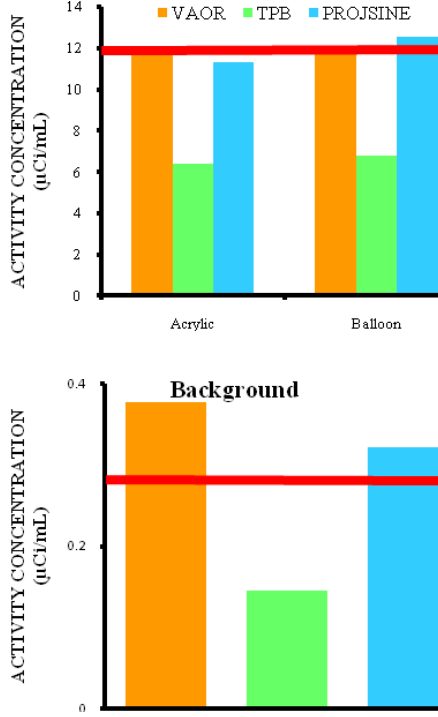


Fig. 10. Bar charts of dose calibrator (red lines) and decay corrected image measured activity concentration for the acrylic and balloon lesions (TOP) and uniform breast background (BOTTOM).

IV. CONCLUSIONS

A method to quantify the activity concentration of regions of interest in data acquired with our unique dedicated SPECT system has been implemented. The average activity concentration reported in hot-volume regions corresponds to within 15% of the actual measured activity concentrations. Larger errors persist in diffuse background regions, most likely due to the much higher noise characteristics (variability) in the background.

For this anthropomorphic breast data set, VAOR and PROJSINE data have better than 15% accuracy with respect to the absolute activity concentration. Insufficiently sampled TPB data, not unexpectedly, has the worst accuracy.

Very low activity concentrations are more difficult to accurately quantify, most likely due to their poorer counting statistics. For this study, a $\pm 4\%$ photopeak energy window was used, despite that part of the photopeak is cutoff due to low energy tailing using the compound semi-conductor detector system. The accuracy of quantifying low activity concentration regions by utilizing more of the photopeak events (increasing the counting statistics) will be investigated.

Additional future steps to improve results would include using the CT reconstructed data set to calculate the spatial distribution map of attenuation coefficients as well as to define the ROI for better placement, and correcting for partial volume effects. To analyze the mean activity concentration in the syringes we were able to use relatively large ROIs and place them well within the boundaries of the syringe, minimizing partial volume effects. However, for smaller and/or irregularly shaped hot spots (lesions), ROI placement has a large effect on the measured mean activity concentration. Thus, having a CT selected ROI would give more confidence in the measurement.

V. ACKNOWLEDGEMENTS

MPT is an inventor of this dedicated SPECT imaging technology, and is named as an inventor on the patent for this technology assigned to Duke. If this technology becomes commercially successful, MPT and Duke could benefit financially.

REFERENCES

- [1] M. S. Rosenthal, J. Cullom, W. Hawkins, S. C. Moore, B. M. Tsui and M. Yester, "Quantitative SPECT imaging: a review and recommendations by the Focus Committee of the Society of Nuclear Medicine Computer and Instrumentation Council," *J Nucl Med*, vol. 36, p. 1489-513, 1995.
- [2] R. J. Jaszcak, K. L. Greer, C. E. Floyd, C. C. Harris and R. E. Coleman, "Improved SPECT Quantification Using Compensation for Scattered Photons," *J Nucl Med*, vol. 25, p. 893-900, 1984.
- [3] J. E. Bowsher, V. E. Johnson, T. G. Turkington, R. J. Jaszcak, C. R. Floyd and R. E. Coleman, "Bayesian reconstruction and use of anatomical a priori information for emission tomography," *IEEE Trans on Med Img*, vol. 15 p. 673-86, 1996.
- [4] C. B. Hruska and M. K. O'Conner, "Quantification of Lesion Size, Depth and Uptake Using a Dual-Head Molecular Breast Imaging System," *Med Phys*, vol. 35 p. 1365-1376, 2008.
- [5] M. B. Williams, M. J. More, D. Narayanan, S. Majewski, B. Welch, R. Wojcik, and D. A. Kieper, "Phantom Study of Radiotracer Concentration Quantification in Breast Scintigraphy," *IEEE Trans Nucl Sci*, vol. 50, p. 433-438 2003.
- [6] C. Archer, M. Tornai, and J. E. Bowsher, "Implementation and Initial Characterization of Acquisition Orbits with a Dedicated Emission Mammothomograph," *IEEE Trans Nucl Sci*, vol. NS50, p. 8, 2003.
- [7] J. H. Hubbell and S. M. Seltzer, " <http://physics.nist.gov/PhysRefData/XrayMassCoef/cover.html>" *NIST*, 1996.
- [8] C. N. Brzymialkiewicz, "Development and evaluation of a dedicated emission mammothomography system," Duke University, 2005.

Characterizing the MTF in 3D for a Quantized SPECT Camera Having Arbitrary Trajectories

Priti Madhav, *Member, IEEE*, James E. Bowsher, *Member, IEEE*, Spencer J. Cutler, *Member, IEEE*, and Martin P. Tornai, *Senior Member, IEEE*

Abstract—The emergence of application-specific 3D tomographic small animal and dedicated breast imaging systems has stimulated the development of simple methods to quantify the spatial resolution or Modulation Transfer Function (MTF) of the system in three dimensions. Locally determined MTFs, obtained from line source measurements at specific locations, can characterize spatial variations in the system resolution and can help correct for such variations. In this study, a method is described to measure the MTF in 3D for a compact SPECT system that uses a $16 \times 20 \text{ cm}^2$ CZT-based compact gamma camera and 3D positioning gantry capable of moving in different trajectories. Image data are acquired for a novel phantom consisting of three radioactivity-filled capillary tubes, positioned nearly orthogonally to each other. These images provide simultaneous measurements of the local MTF along three dimensions of the reconstructed imaged volume. The usefulness of this approach is shown by characterizing the MTF at different locations in the reconstructed imaged 3D volume using various (1) energy windows; (2) iterative reconstruction parameters including number of iterations, voxel size, and number of projection views; (3) simple and complex 3D orbital trajectories including simple vertical axis of rotation, simple tilt, complex circle-plus-arc, and complex sinusoids projected onto a hemisphere; and (4) object shapes in the camera's field of view. Results indicate that the method using the novel phantom can provide information on spatial resolution effects caused by system design, sampling, energy windows, reconstruction parameters, novel 3D orbital trajectories, and object shapes. Based on these measurements that are useful for dedicated tomographic breast imaging, it was shown that there were small variations in the MTF in 3D for various energy windows and reconstruction parameters. However, complex trajectories that uniformly sample the breast volume of interest were quantitatively shown to have slightly better spatial resolution performance than more simple orbits.

Index Terms—CZT detector, emission imaging, mammotomography, modulation transfer function, single photon computed emission tomography, three-dimensional trajectories.

I. INTRODUCTION

THE Modulation Transfer Function (MTF) can be used to characterize the frequency composition of spatial resolution. For emission imaging, the MTF can be determined via

Manuscript received March 20, 2008; revised August 19, 2008 and December 09, 2008. Current version published June 10, 2009. This work was supported in part by NIH R01-CA096821, in part by DOD W81XWH-06-1-0791 and W81XWH-06-1-0765, and in part by NIH EB001040-01.

P. Madhav, S. J. Cutler, and M. P. Tornai are with the Multi-Modality Imaging Lab, Department of Radiology, Duke University Medical Center, and the Department of Biomedical Engineering, Duke University, Durham, NC 27710 USA (e-mail: priti.madhav@duke.edu).

J. E. Bowsher is with the Department of Radiation Oncology, Duke University Medical Center, Durham, NC 27710 USA.

Digital Object Identifier 10.1109/TNS.2009.2013464

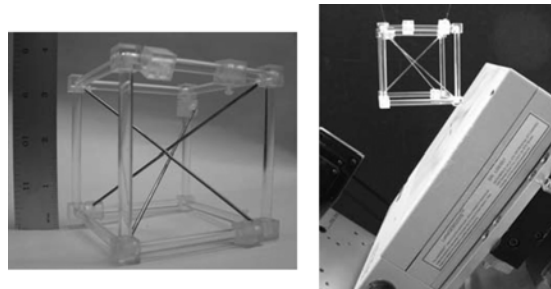


Fig. 1. (Left) Photograph of the acrylic phantom frame with three brass rods (brass rods were used in place of capillaries for the photo to clearly display the position of each tube). (Right) Photograph of the phantom suspended in front of the compact SPECT camera in air during a 360° acquisition.

the line spread function (LSF) from images of a line source [1] (i.e. a capillary tube filled with radioactivity) or an edge source (i.e. radioactivity placed behind a lead plate) [2] in air. Measurements are usually taken at various distances from the camera face to determine spatial variations in resolution. MTF variations with respect to object-to-background ratio contribute to characterizing system linearity. Knowledge of these variations in the spatial resolution of an imaging system is important in understanding the reliability of information derived from an image, (i.e. gauging the minimum size of a lesion that could be detected).

In emission tomography, spatial resolution is determined quantitatively by measuring the LSF or point spread function (PSF), and semiquantitatively by assessing the reconstructed image quality of standard test objects such as the 3D disk and frequency-resolution (cold or hot) rod phantoms. In 2D, measurements of the LSF or PSF often assume that radiation detectors have a continuous response across their surface that is invariant within any given plane parallel to the detector's surface. However, this invariance assumption is questionable for recent medium- and small-field-of-view nuclear emission cameras having quantized detector elements, as are assumptions of approximately Gaussian response. Parallel hole or pinhole collimation, e.g. for small-animal imaging, involves significant nonstationarity in gamma camera response. It is also more common to describe the system performance in the frequency domain by obtaining the Fourier Transform of the PSF or LSF. Generally, image filtering is done in frequency space. The noise power spectrum (NPS), detective quantum efficiency (DQE), and other common parameters used in describing system response are also all measured in the frequency domain and

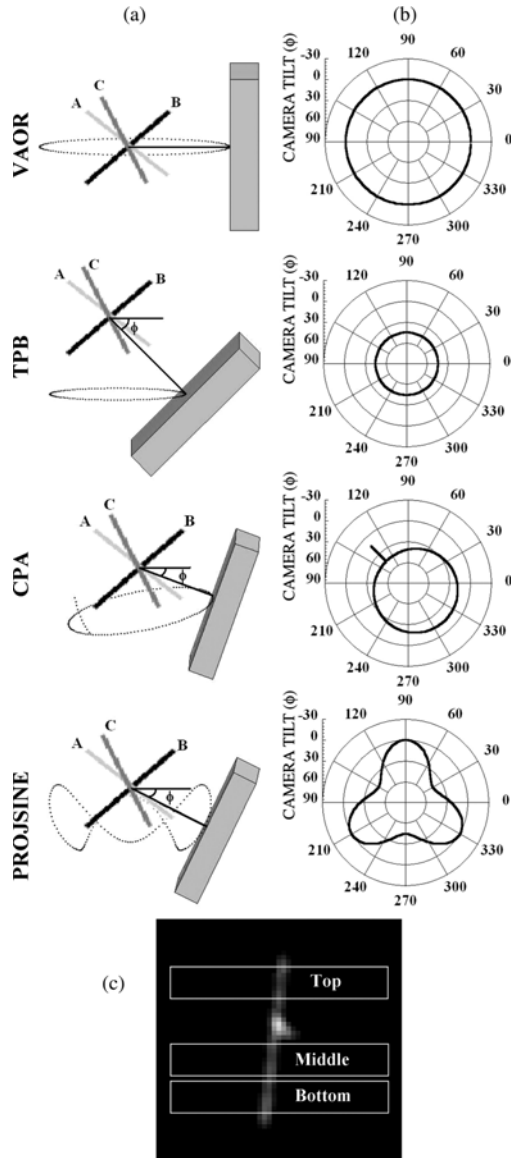


Fig. 2. (a) 3D setup of the phantom for all four trajectories. The SPECT camera (shown as a gray box) is facing left towards the phantom, placed at the center of the field-of-view. The phantom consists of three radioactivity-filled capillary tubes (labeled A,B,C). The shown placement of the tubes nearly matches the photograph of the phantom suspended in front of the SPECT camera in Fig. 1. The direction of increased polar camera tilt, ϕ , is also shown relative to the horizon. (b) Next to each 3D schematic is the corresponding polar plot (i.e. camera tilt) of the camera trajectory (plotted as a radius with $+90^\circ$ at the center and -30° at the edge) versus azimuth angle (plotted around the circle from 0° to 360°). (c) Reconstructed slice (5th iteration, 8 subsets, $80 \times 80 \times 80$ grid size, 2.5 mm) for one isolated capillary tube located in air acquired with a TPB orbit. "Top," "Middle," and "Bottom" of the capillary tube are defined for subsequently presented results, and span 11 cm along the length of the line source.

require the MTF in their calculations. Thus, there are various reasons for computing the MTF instead of simply the PSF or

TABLE I
TRAJECTORY PARAMETERS USED FOR EACH ACQUISITION
OVER A 360° AZIMUTHAL RANGE

Trajectories	Acronym	Number of Projs	Polar Tilt Range (min-max degrees)	ROR Range (min-max cm)
Vertical Axis of Rotation	VAOR	128	0°	8.74
Tilted Parallel Beam	TPB	128	45°	4.05
Circle Plus Arc	CPA	139	0° - 45°	4.05-6.48
Three-Lobed Sinusoid Projected onto a Hemisphere	PROJSINE	150	15° - 45°	4.05-8.74

LSF. Therefore, by looking at the frequency response, measurement of the MTF in 2D or 3D can provide a quantitative insight into the full frequency response of the system regardless of the detector response function.

Previous line-source phantoms used to measure the MTF in 3D have been limited to measuring the spatial resolution one dimension at a time [3]–[5]. Arrays of point sources have also been used to assess spatial resolution in three dimensions at various locations throughout the image volume [6]. However, unlike line sources, 3D arrays of point sources are more difficult to manufacture and position uniformly, and also are more difficult to evaluate under different scatter and scatter-free conditions due to the nature of their support structure. For this work, a novel phantom was constructed to fully evaluate the three-dimensional MTF along three nearly orthogonal axes after a single tomographic acquisition. This phantom allows for the characterization of spatial resolution in three dimensions and at various locations throughout the imaged volume, providing insight into the total amount of blur and its spatial variation. This phantom can be especially useful for tomographic imaging systems capable of fully-3D acquisitions for SPECT or PET, though it could also be modified for use in transmission imaging systems [7].

Over the past few years, our laboratory has developed a dedicated emission mammotomography system [8]–[11]. Several 3D, non-traditional, noncircular trajectories about a pendant breast with various lesion sizes located in different areas have been implemented and assessed [9], [12]. Due to the spatially varying spatial resolution in SPECT and the nonlinear response of iterative ordered-subsets expectation maximization (OSEM) reconstruction, the system blur cannot be fully described by a single LSF or MTF. Instead, some indication of system blur can be provided by measuring the blur at several locations in the image, for several signal-to-background ratios, and for several sizes and shapes of structures of interest.

The purpose of this study is to describe the novel phantom and to use this phantom to characterize the local MTF in 3D and to identify parameters that can affect the overall spatial resolution of our current SPECT system. Here we focus on measuring the MTF in different locations in the 3D volume using several different energy windows, different reconstruction parameters and acquisition trajectories, and different object shapes. In the present paper, LSF refers to the image of a line source in zero



Fig. 3. Photographs of the MTF phantom contained inside (Left) the 2000 mL cylinder and (Right) 850 mL breast phantom shell. (Bottom) Phantom was immersed in the water to the extent possible to quantify the effect of different object shapes along with various acquisition trajectories on the MTF, and (Top) is also shown in the phantoms without water present.

background and at a particular location. MTF refers to the absolute magnitude of the Fourier Transform of a particular LSF (i.e. at a particular location in the image) and thus throughout this paper the MTF will be referred to as the local MTF. In addition, isotropic in this paper is defined in terms of the MTF being uniform throughout the entire volume.

II. MATERIALS & METHODS

A. MTF Phantom

In order to quantify the spatial response of any imaging system including detector response, image acquisition procedures, complex 3D trajectories, scatter, and photon attenuation, a novel phantom was constructed (Fig. 1) to measure the local MTF in 3D. This phantom could be used for both emission (SPECT, PET, or even MRI) and transmission (X-ray CT) systems [7], [13]. A line source was chosen from which to obtain the MTF, since a radioactivity-filled capillary tube for emission imaging and solid tungsten wire for transmission imaging are easily interchangeable. Thus, this phantom would allow using a similar acquisition and quantification procedure for most imaging systems. More than one line source was necessary such that the MTF could be measured at different locations in the reconstructed imaged volume after a single tomographic acquisition. Using too many line sources runs the risk of creating an overlap between the line sources in the reconstructed images, and so three lines were chosen. Additionally the phantom had very low scatter and attenuation characteristics, could be easily assembled, could be placed in any desired position in the camera's field of view, could be inserted into various fluid

filled containers, and could provide flexibility to reposition the line sources in order to image anywhere in the imaged volume.

Based on the desired features, acrylic rods (side length of 7.8 cm) are attached together into the shape of a box frame. Three capillary tubes (~ 11 cm long with 0.9 mm inner diameter) filled with 44.4–66.6 MBq of aqueous ^{99m}Tc (140 keV) were placed within the boxed frame such that each tube was held from one vertex to its corresponding opposite end, slightly away from another vertex. On its corresponding opposite end, the tube is attached to a slider piece which gives the flexibility to position the tube anywhere along the length of the side-rod to which it is attached. Once the desired position of the rod was set, the sliding support was fixed with an acrylic screw pressed against the side-rod. Depending on the size of the SPECT system, pixel size of the camera, and its minimum radius of rotation, smaller or larger capillary tubes could be used to encompass the entire field of view. The tubes were visibly separable in their positions such that they did not touch one another, and spanned the entire field of view. Also, they were not placed at exactly orthonormal planes in order to avoid interplay of measured responses from different directions near the center of the field of view.

B. Data Acquisition and Image Reconstruction

Our emission tomography system is composed of a compact $16 \times 20 \text{ cm}^2$ field of view cadmium zinc telluride (CZT) LumaGEM 3200S gamma camera (Gamma Medica, Inc., Northridge, CA) attached to a hemispherically positioning gantry. The camera uses a 64×80 array of $2.5 \times 2.5 \times 6 \text{ mm}^3$ quantized CZT elements for a total of 5120 pixels. Measured mean energy resolution of the gamma camera at 140 keV is 6.7% FWHM and overall sensitivity is 37.9 cps/MBq [11]. A parallel-hole collimator with hexagonal holes (1.2 mm hole size flat-to-flat (inner diameter), 0.2 mm septa, and 25.4 mm height) is used in these studies. Due to the flexible gantry, the camera can be positioned anywhere in a hemisphere to facilitate acquiring projection data around a pendant uncompressed breast [8], [9], [11], [12].

Projections were collected over a 360° azimuthal rotation around the phantom suspended in air [Figs. 1 and 2(a)] using a vertical axis of rotation (VAOR), comparable to the simple circular orbits used by clinical SPECT systems (about their horizontal axis). Acquisitions were made at a radius of rotation (ROR) that corresponded to the minimum ROR possible when the MTF phantom was placed in different object shaped media (described in the next section). Data was collected in list mode and post-processed to obtain $\pm 4\%$ and $\pm 8\%$ wide symmetric energy windows about the 140 keV photopeak. Total scan time for each acquisition was 10 min, with increased acquisition times for subsequent scans to compensate for radioactive decay. Under these conditions, there were ~ 28 k events per projection in the $\pm 8\%$ wide energy windowed data.

Images were iteratively reconstructed using 8 subsets of OSEM, and displayed at 1, 3, 5, and 10 iterations in all cases. These reconstructions were on a grid of $80 \times 80 \times 80$ voxels, for two different voxel widths—1.25 mm and 2.50 mm. The reconstructions were performed using the same ray-driven code as described earlier in [9], [10].

Three other trajectories were investigated: (1) tilted parallel beam (TPB) with 45° fixed camera tilt; (2) tilted circle plus (one) arc (CPA) with 45° max camera tilt, and (3) a three-lobed sinusoid projected onto a hemisphere (PROJSINE) with 0° to 45° polar camera tilting range (sinusoidal amplitude). These trajectories have been investigated elsewhere [9], [11], [12], but not for their frequency response characteristics. These trajectories and the direction of polar camera tilt are illustrated in Fig. 2. Specific parameters that were used for all four trajectories are given in Table I. The increased number of projections is due to the use of polar (ϕ) sampling along with azimuthal (θ) sampling, necessitating $\Delta\phi$ steps along with $\Delta\theta$ steps to reach 360° azimuthally.

C. MTF Phantom in Different Object Shapes

The degrading effects of different object shapes on the MTF were also evaluated by placing the line source phantom in two different environments: 2000 mL water-filled glass-walled cylinder (12 cm diameter) and 850 mL water-filled plastic-walled breast-shaped container (nipple-to-chest distance of 11 cm, medial-lateral distance of 17 cm, and superior-inferior distance of 18 cm) (Fig. 3). All four trajectories were investigated except for the cylinder where only VAOR was used. The local MTF was calculated for all trajectories measured with the phantom placed in the cylinder and breast. Data was collected using an $\pm 8\%$ wide symmetric energy window and was post-processed to also obtain $\pm 4\%$ wide symmetric energy windows. Energy window width for dedicated, uncompressed breast imaging has been shown to affect image quality under various acquisition conditions [14]. The $\pm 8\%$ wide energy window, while not exploiting the fine resolution capability of CZT (6.7% intrinsic FWHM), corresponds to that used in standard, clinical nuclear medicine camera systems (15% wide), and is substantially narrower than that of scintillator based compact, quantized detector element gamma cameras (30% wide). Furthermore, early contrast-detail observer studies with this system have shown that energy windows near but above the intrinsic system resolution allow for visualization of small objects [14]. The ROR was determined by placing the breast 1 cm or less away from the camera face at all camera orientations. For all four trajectories tested, acquisitions were obtained at the same RORs used for the phantom in air (shown in Table I). Scans were also performed over 10 min, with increased acquisition times for subsequent scans to compensate for radioactive decay. Under these conditions, approximately 13 k counts were collected in each $\pm 8\%$ wide energy windowed projection of the MTF phantom measured in the scatter media. Iterative reconstruction was performed using the same parameters for the projections of the phantom suspended in air.

D. Local MTF Determination

The overall local MTF calculation was computed based on an algorithm presented elsewhere [15], and has been successfully applied in the preliminary local MTF measurements of our 3D X-ray computed mammotomography (CmT) system as well [7]. Once the images were reconstructed, the first step was to manually rotate the images such that each tube could be isolated onto a single slice [Fig. 2(c)]. A binary line image of the outline of

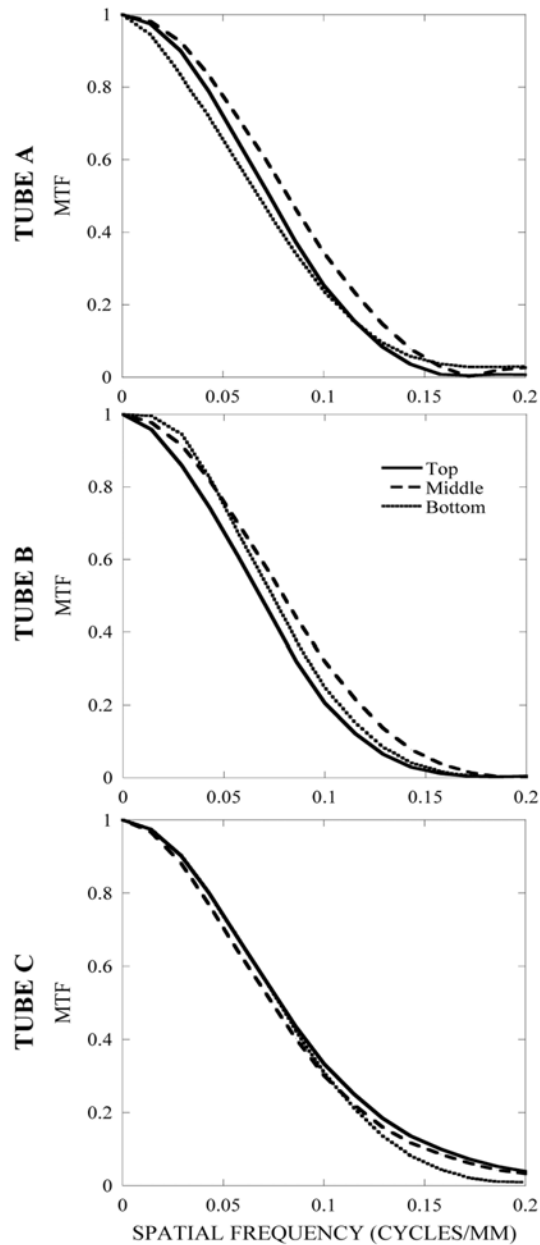


Fig. 4. Results for tube A (top), B (middle), and C (bottom) show little variation in MTFs at different portions along the capillary line source for a 360° SPECT acquisition. MTF measurements were obtained from measurements taken of the phantom in air using a simple VAOR orbit. Nyquist frequency is at 0.2 mm^{-1} .

the tube was acquired by using a Sobel edge detection method [16]. The angle and position of the tube was determined by the Radon transform. Based on the resulting curves in polar coordinate space, the location of the curves' intersection (i.e. maximum intensity) gave an estimate of the angle and spatial position of the line source [17]. Inaccuracy in estimating the true

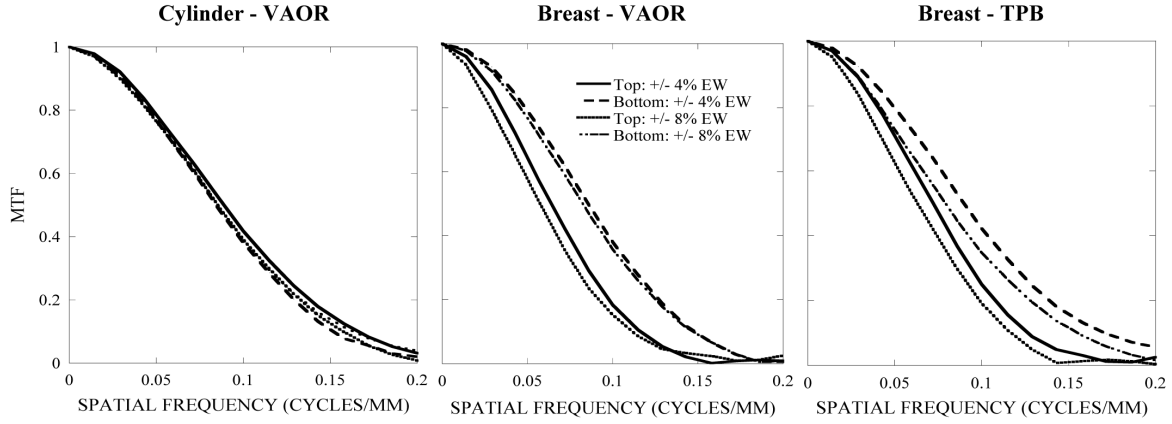


Fig. 5. MTF of the top and bottom segment of the capillary source B placed in a water-filled cylinder (Left) and a water-filled breast shape phantom acquired using VAOR (Middle) and TPB (Right) orbits at $\pm 4\%$ and $\pm 8\%$ energy windows. Tighter energy windows appear to have a slight improvement in resolution especially at the TPB case.

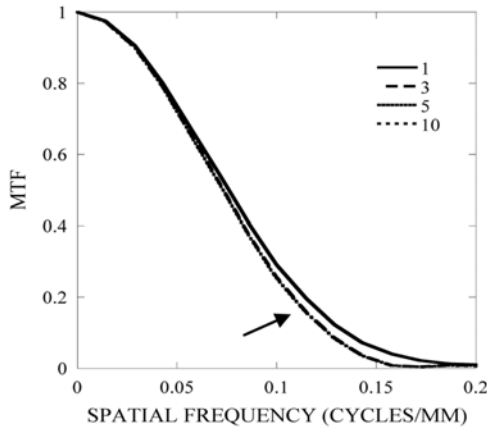


Fig. 6. MTF at several iterations of the phantom in air using VAOR. MTFs overlap for iterations 3, 5 and 10 (shown by arrow). MTF was obtained using the top portion of capillary A.

angle of a line can give an unsmooth LSF and degrade the MTF, especially in higher frequency regions. A composite local LSF was generated by reprojecting and resampling a small region of interest around the line source onto a one-dimensional array of sub-pixel bins positioned perpendicular to the calculated angle of the tube. Use of subpixel bins was necessary since the samples were not uniformly distributed along the one-dimensional array [18]. Different subpixel bin sizes (0.1, 0.3, and 0.7) were initially tested to find an optimal bin size. For smaller bin sizes, such as 0.1, high frequency components were exaggerated in the MTF due to the increased noise. At larger bin sizes, such as 0.7, the zero of the MTF occurred below the Nyquist frequency. Therefore, for this work 0.3 subpixel bin size was found to be the optimal size. The samples were thus binned to 1/3 of the

original pixel size of 2.5 mm. This result was then smoothed by averaging neighboring pixels within a three pixel moving average window to get the final local LSF (LSF_f)

$$LSF_f(x) = \frac{LSF(x-1) + LSF(x) + LSF(x+1)}{3} \quad (1)$$

where x is the spatial location of the pixel. Smoothing is necessary to reduce the noise and effect of the high-frequency response in the MTF. Zero padding and a Hanning filter were also applied to the local LSF to eliminate other high frequency artifacts.

Corresponding local MTFs were calculated by taking the absolute value of the one-dimensional discrete Fourier Transform of the LSF_f

$$MTF(f) = |\Im\{LSF_f(x)\}| \quad (2)$$

where f represents the spatial frequency. The local MTF here describes the magnitude of the component response of the system to the known input. Since an infinitely small line source is not being used, the effects of the finite width of the capillary tube, a , is corrected for by dividing the MTF by $a \text{sinc}(\pi a f)$. This MTF was finally normalized to yield the final MTF. The MTFs along various parts of the tube (e.g. a “local MTF”) were calculated in order to evaluate the response at different locations in the sampled volume [Fig. 2(c)].

For each tube, an average MTF, its standard deviation, and upper and lower bounds for the estimated average MTF was calculated from the measured MTF along different segments of the tube. Using these results, the root mean square difference (RMSD) was calculated by subtracting the upper and lower bounds, squaring the difference, finding the average of all these squared differences, and taking the square root. The measured RMSD values help to evaluate the amount of uniformity in the MTF along different portions of a single line source.

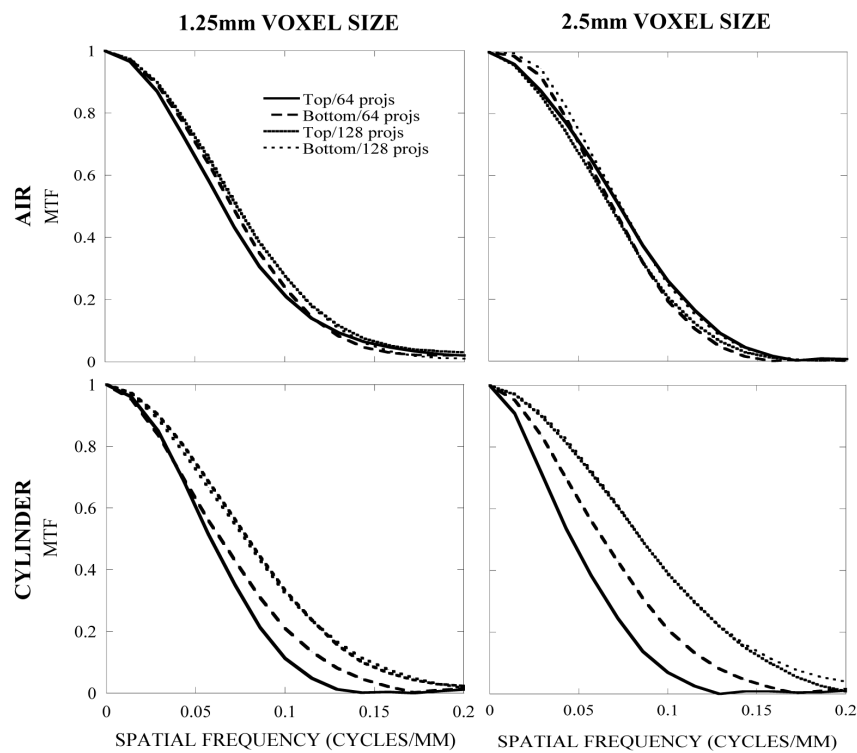


Fig. 7. (Top row) MTF obtained of the phantom in air at a reconstructed voxel size of (Left column) 1.25 mm ($160 \times 160 \times 160$ grid size) and (Right column) 2.5 mm ($80 \times 80 \times 80$ grid size). Plots indicate very slight difference between the different numbers of indicated projections. (Bottom row) Unlike in air, the MTF obtained from the phantom in the water-filled cylinder, for both voxelizations, has a greater decrease and more anisotropy in MTF for the 64 projection data set. MTFs shown here were obtained using capillary tube B and VAOR orbital acquisition (see Fig. 2).

III. RESULTS AND DISCUSSION

A. MTF Along Different Line Location

Fig. 4 shows the local MTFs measured in air with the $\pm 8\%$ wide energy window at different locations along each of the nearly orthogonal capillary tubes. Measurements were derived from images collected of the phantom in air using the VAOR orbit. For all three orientations, there was only a small variation in the MTF along the lines, indicating uniform 3D resolution throughout the imaged volume. VAOR orbits are known to be the largest uniformly sampled volumes for both conventional and compact, versatile 3D SPECT cameras [9]. The uniformity of these results is not surprising since the SPECT scan was collected over a 360° azimuthal orbit. Hence, projection “averaging” throughout this reconstructed volume may be expected to yield a nearly uniform response.

B. MTF at Different Energy Window

The MTF was also determined at $\pm 4\%$ and $\pm 8\%$ energy windows to see if different amounts of object scatter would affect the resolution of the reconstructed images. Fig. 5 shows the MTF for one of the capillary tubes in the MTF phantom suspended in the water-filled cylinder and the water-filled breast,

with data acquired using VAOR and TPB orbits at both energy windows. For the cylinder, there is no difference in the MTFs measured anywhere along the line.

For the breast phantom, the MTF results are somewhat different. There are differences in the measured MTFs at different locations, which correspond to the thicker posterior breast (top) or narrower anterior breast near the nipple (bottom), but only slight differences in these locations due to energy window width. Furthermore, using a smaller energy window with incomplete sampling and the TPB orbit also had a very slight effect on the local MTF.

C. MTF With Various Reconstruction Parameters

In OSEM, the projection data is grouped into subsets and the EM algorithm is applied to each subset to get an estimate of the image. In principle, more iterations are performed until the algorithm has converged to a true (or near) optimum value. However this can yield images of poor quality. Previous studies for emission mammotomography imaging breast lesions have shown that there is a trade-off between the rate of contrast improvement and SNR degradation in the reconstructed images [8], [9], [12]. This contrast-SNR roll-over is similar to the minimum of a bias-variance metric. For SPECT mammotomography imaging this roll-off is often best between 2 and 3 iterations.

In a similar way, the measured local system MTF appears to have stopped changing after only a few iterations. Fig. 6 shows the MTF at 1st, 3rd, 5th, and 10th iterations along a single dimension. The slow-down in MTF improvement is probably similar to the slow-down in contrast improvement with increasing iterations. At the 5th and 10th iteration, it appears that there is no change in the MTF beyond the 3rd iteration. The results are similar (not shown) for the other portions of each of the three capillary sources for a uniform orbit such as VAOR.

Using smaller voxel sizes and fewer projection images during iterative reconstruction can also have an effect on the measured resolution (Fig. 7). As voxel size decreases and number of projections increase, the MTF expectedly improves and remains consistent (less anisotropic), especially under non-ideal conditions (i.e. water-filled cylinder) (Fig. 7, BOTTOM). From these plots, it can be inferred that when acquiring fewer projections under non-ideal conditions, the MTF varies significantly due to incompleteness of sampling the scatter distribution and can introduce artifacts in the reconstructed images. However, very small differences are seen in the MTF for conditions without scatter (Fig. 7, TOP). The MTF obtained at 128 projections in the water-filled cylinder appears to be better than in air. This could be due to the increased attenuation and noise in the scatter images which made it more difficult to localize the signal.

D. MTF With Various 3D Trajectories

Other than VAOR, three different trajectories, TPB, CPA, and PROJSINE, were also evaluated by measuring the MTF at three different locations along the capillary tube in air (Fig. 8). RMSD results in Table II indicate small but similar variations in the MTF for VAOR and PROJSINE. The importance of this is that the complex trajectory will likely be necessary for clinical breast imaging [8], [9], while VAOR provides a completely sampled region with the largest volume. The TPB and CPA trajectories yielded a worse MTF in the top portion, but had a better MTF at the bottom portion due to the relative position of the camera to the line sources (Fig. 8). This is most likely due to a combination of incomplete sampling, attenuation, and distance related degradations associated with SPECT imaging.

Fig. 9 shows the difference in spatial resolution among each of the four orbits for the top segment of the capillary tube. Previous studies have shown that insufficient sampling can cause the reconstructed slices to be distorted [9], [12]. For the TPB orbit, in contrast to the bottom segment of the capillary source, the top segment of the capillary tube [shown in schematic in Fig. 2(a)] is never close to the face of the SPECT camera, causing a difference in the measured spatial response.

E. MTF Within Different Object Shapes

Using a VAOR orbit, the MTF was determined for the line phantom suspended in (1) air; (2) a water-filled cylinder; and (3) a water-filled breast phantom using the same, fixed ROR for all three cases. Images reconstructed with 5 iterations and 5 subsets of an OSEM algorithm produced minimal differences between

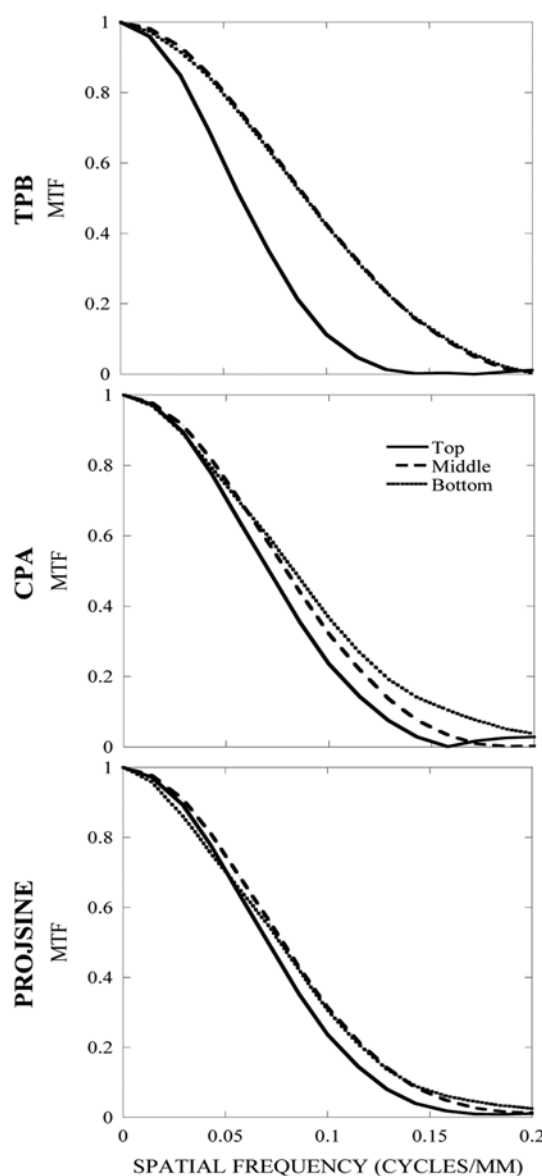


Fig. 8. Using TPB (top), CPA (middle), and PROJSINE (bottom) trajectories, the MTFs were obtained from the top, middle, and bottom segment of the reconstructed line source B. The MTFs for TPB and CPA have more variation among different segments along the tube compared to VAOR (Fig. 4, middle) and PROJSINE. For the bottom line segment, both TPB and CPA actually give a higher MTF than VAOR and PROJSINE due to the bottom segment being closest to the camera throughout the trajectory, as seen in the schematic in Fig. 2(a).

the MTF obtained in air and in the cylinder (Figs. 4 and 7), but showed a slight difference in comparison to the MTF obtained with the breast phantom (Fig. 10) mostly likely due to the differences in object shape (i.e. breast phantom versus a cylinder) and a slight difference in the measured location relative to the measurement in air or with the cylinder. RMSD values for capillary

TABLE II
RMSD VALUES FOR EACH CAPILLARY TUBE ACQUIRED
USING VARIOUS TRAJECTORIES

Trajectories	Tube A	Tube B	Tube C
VAOR	0.049	0.044	0.039
TPB	0.145	0.123	0.042
CPA	0.103	0.093	0.091
PROJSINE	0.041	0.032	0.040

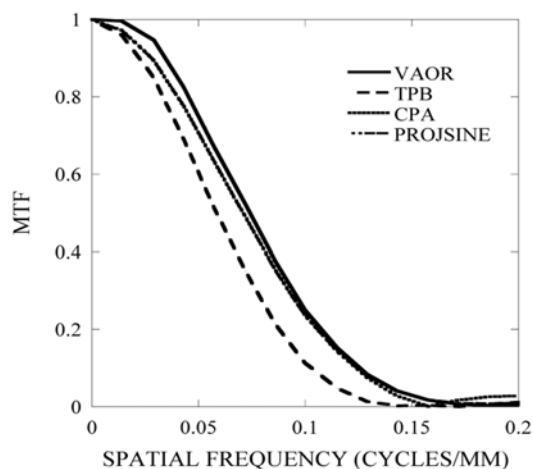


Fig. 9. MTFs were obtained from the top segment of the reconstructed line source B for each of the three orbits. TPB produces slightly worse MTFs than VAOR and PROJSINE since the top segment is farther away from the camera for those trajectories.

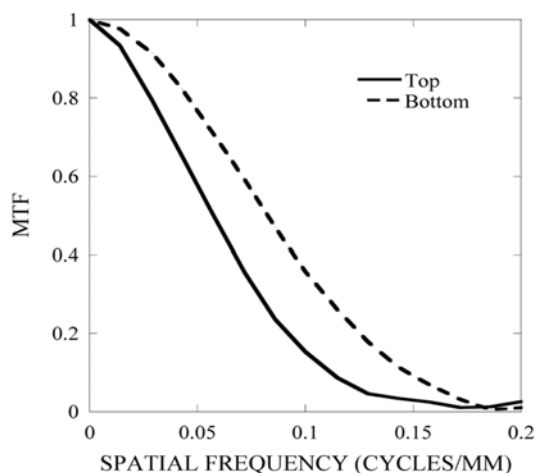


Fig. 10. MTF obtained from the line phantom (capillary tube B) placed in the breast using the VAOR orbit. Unlike MTF curves obtained in air and a cylinder, there is more variation in MTF in a breast phantom.

tube B acquired in air, cylinder, and breast are 0.044, 0.048, and 0.064, respectively. This slight degradation in resolution seen with VAOR in a breast phantom illustrates the necessity of using

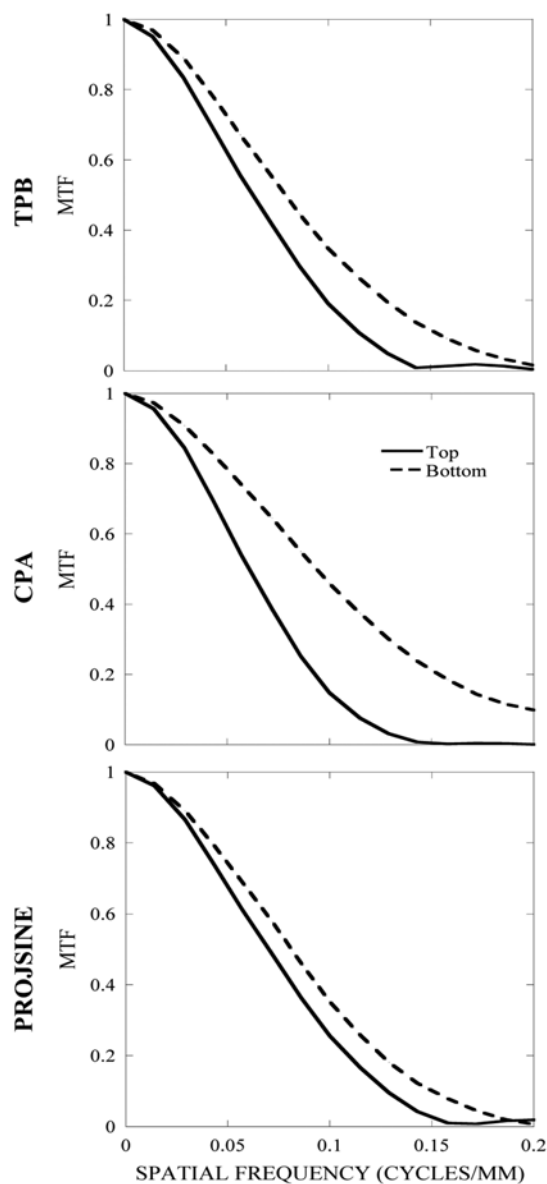


Fig. 11. MTF obtained from the phantom (top and bottom segment of capillary tube B) placed in the breast using TPB (top), CPA (middle), and PROJSINE (bottom) trajectories. Results are very similar to results measured in air.

novel trajectories that use increased camera tilt angles to improve sampling and also achieve a closer ROR. As shown in Figs. 10, 11, and Table III, there is slight variation in the MTFs with VAOR, TPB and CPA trajectories, consistent with earlier results using these trajectories. There is considerably less variation with PROJSINE. Comparisons of all four trajectories are plotted together for the top and bottom segment of the capillary tube (Fig. 12).

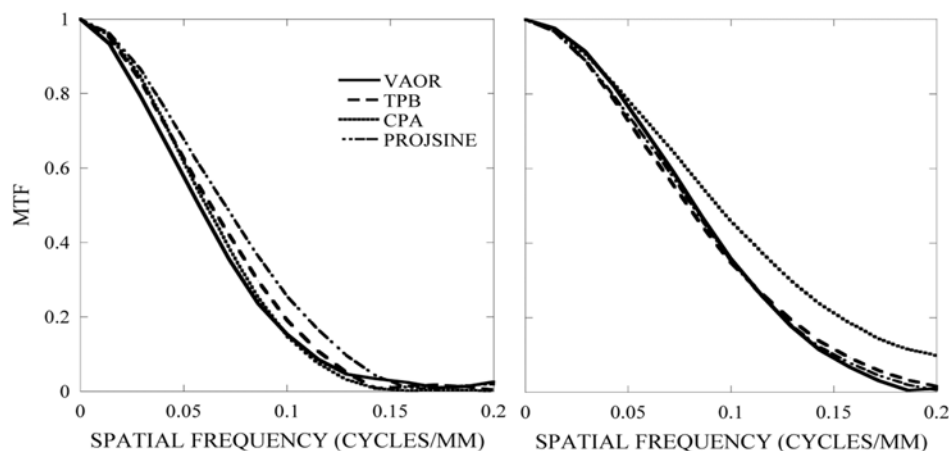


Fig. 12. MTF of the top (left) and bottom (right) segment of capillary source B placed in the breast for all four trajectories.

TABLE III
RMSD VALUES FOR EACH CAPILLARY TUBE IN BREAST ACQUIRED
USING VARIOUS TRAJECTORIES

Trajectories	Tube A	Tube B	Tube C
VAOR	0.056	0.064	0.086
TPB	0.103	0.092	0.122
CPA	0.092	0.119	0.096
PROJSINE	0.050	0.052	0.046

IV. CONCLUSION

In this work, we have developed a novel phantom for use in measuring the local MTF in 3D to evaluate versatile, novel-trajectory emission tomographic systems and provide an insight into the degrading effects caused by different orbital acquisitions, different shaped geometries, and the reconstruction process. This initial study demonstrated that energy window has a secondary effect on resolution, in contrast to incomplete sampling. The relatively small number of OSEM iterations also had little effect on the MTF, and that more projections are necessary in non-ideal conditions (i.e. with attenuation media) to yield an improved and more isotropic MTF. Also, it was shown that unlike for simple circular (VAOR) and more complex (PROJSINE) trajectories, asymmetric acquisition trajectories (e.g. TPB and CPA) have more variations in the MTF between different locations in 3D space. Differences between the curves are caused both by trajectories having fixed polar tilt and subsequently incomplete sampling. This implies that a complex trajectory like PROJSINE more uniformly samples the breast volume of interest and may be necessary for clinical breast imaging. Having flexible 3D positioning about the breast yielded minimal RMSD differences, which is important for high resolution molecular emission imaging.

This study also demonstrates the benefit of using a local 3D MTF phantom to evaluate a tomographic imaging system. With such a phantom, the effect of attenuation, scatter, energy windows, reconstruction process, and 3D trajectories can be easily evaluated to get a better understanding on how these different parameters can affect image quality.

ACKNOWLEDGMENT

The authors would like to thank Dr. C. Catarious and Dr. E. Samei for their assistance in this project.

REFERENCES

- [1] M. L. Nusynowitz and A. R. Benedetto, "Simplified method for determining the modulation transfer function for the scintillation camera," *J. Nucl. Med.*, vol. 16, pp. 1200–1203, 1975.
- [2] T. Väyrynen, U. Pitkänen, and K. Kiviniitty, "Methods for measuring the modulation transfer function of gamma camera systems," *Eur. J. Nucl. Med.*, vol. 5, pp. 19–22, 1980.
- [3] M. Coleman, M. A. King, S. J. Glick, K. Knesaurek, and B. C. Penney, "Investigation of the stationarity of the modular transfer function and the scatter fraction in conjugate view SPECT restoration filtering," *IEEE Trans. Nucl. Sci.*, vol. 36, pp. 969–972, 1989.
- [4] S. J. Glick, M. A. King, K. Knesaurek, and K. Burbank, "An investigation of the stationarity of the 3D modulation transfer function of SPECT," *IEEE Trans. Med. Imag.*, vol. 36, pp. 973–977, 1989.
- [5] S. J. Glick, W. G. Hawkins, M. A. King, B. C. Penney, E. J. Soares, and C. L. Byrne, "The effect of intrinsic attenuation correction methods on the stationarity of the 3-D modulation transfer function of SPECT," *Med. Phys.*, vol. 19, pp. 1105–1112, 1992.
- [6] L. R. Furenlid, D. W. Wilson, Y. Chen, H. Kim, P. J. Pietraski, M. J. Crawford, and H. H. Barrett, "FastSPECT II: A second-generation high-resolution dynamic SPECT imager," *IEEE Trans. Med. Imag.*, vol. 51, pp. 631–635, 2004.
- [7] P. Madhav, R. L. McKinley, E. Samei, J. E. Bowsher, and M. P. Tornai, "A novel method to characterize the MTF in 3D for computed mamotomography," in *Proc. SPIE Med. Imag. Conf.*, Feb. 11–17, 2006, vol. 6142.
- [8] M. P. Tornai, J. E. Bowsher, C. N. Archer, J. Peter, R. J. Jaszczak, L. R. MacDonald, B. E. Patt, and J. S. Iwanczyk, "A 3D gantry single photon emission tomograph with hemispherical coverage for dedicated breast imaging," *Nucl. Instrum. Meth. Phys. Res. A*, vol. 497, pp. 157–167, 2003.
- [9] C. N. Archer, M. P. Tornai, J. E. Bowsher, S. D. Metzler, B. C. Pieper, and R. J. Jaszczak, "Implementation and initial characterization of acquisition orbits with a dedicated emission mamotomograph," *IEEE Trans. Nucl. Sci.*, vol. 50, pp. 413–420, 2003.
- [10] C. N. Brzymialkiewicz, M. P. Tornai, R. L. McKinley, S. J. Cutler, and J. E. Bowsher, "Performance for dedicated emission mamotomography for various breast shapes and sizes," *Phys. Med. Biol.*, vol. 51, pp. 5051–5064, 2006.
- [11] C. N. Brzymialkiewicz, M. P. Tornai, R. L. McKinley, and J. E. Bowsher, "Evaluation of fully 3D emission mamotomography with a compact cadmium zinc telluride detector," *IEEE Trans. Med. Imag.*, vol. 24, pp. 868–877, 2005.

- [12] C. N. Brzymialkiewicz, M. P. Tornai, R. L. McKinley, and J. E. Bowsher, "3D data acquisition sampling strategies for dedicated emission mammotomography for various breast sizes," in *Proc. IEEE Nuclear Science Symp. Medical Imaging Conf.*, Oct. 16–22, 2004, vol. 4, pp. 2596–2600.
- [13] P. Madhav, C. N. Brzymialkiewicz, S. J. Cutler, J. E. Bowsher, and M. P. Tornai, "Characterizing the MTF in 3D for a quantized SPECT camera having arbitrary trajectories using a novel phantom," in *Proc. IEEE Nuclear Science Symp. Medical Imaging Conf.*, Oct. 23–29, 2005, pp. 1722–1726.
- [14] S. J. Cutler, C. N. Brzymialkiewicz, and M. P. Tornai, "Investigating the effects of energy resolution in dedicated emission mammotomography," in *Proc. IEEE Nuclear Science Symp. Medical Imaging Conf.*, Oct. 23–29, 2005, vol. 5, pp. 2537–2541.
- [15] E. Samei and M. J. Flynn, "A method for measuring the presampled MTF of digital radiographic systems using an edge test device," *Med. Phys.*, vol. 25, pp. 102–113, 1998.
- [16] J. S. Lim, *Two-Dimensional Signal and Image Processing*. Englewood Cliffs, NJ: Prentice-Hall, 1990.
- [17] R. C. Gonzalez, *Digital Image Processing*, 2nd ed. Reading, MA: Addison-Wesley, 1987.
- [18] H. Fujita, D. Tsai, T. Itoh, K. Doi, J. Morishita, K. Ueda, and A. Ohtsuka, "A simple method for determining the modulation transfer function in digital radiography," *IEEE Trans. Med. Imag.*, vol. 11, pp. 34–39, 1992.

Evaluation of tilted cone-beam CT orbits in the development of a dedicated hybrid mammotomograph

P Madhav^{1,2}, D J Crotty^{1,2}, R L McKinley³ and M P Tornai^{1,2}

¹ Department of Radiology, Duke University Medical Center, Durham, NC 27710, USA

² Department of Biomedical Engineering, Duke University, Durham, NC 27708, USA

³ Zumatek Incorporated, Chapel Hill, NC 27519, USA

E-mail: priya.madhav@duke.edu

Received 13 February 2009, in final form 13 April 2009

Published 28 May 2009

Online at stacks.iop.org/PMB/54/3659

Abstract

A compact dedicated 3D breast SPECT-CT (mammotomography) system is currently under development. In its initial prototype, the cone-beam CT sub-system is restricted to a fixed-tilt circular rotation around the patient's pendant breast. This study evaluated stationary-tilt angles for the CT sub-system that will enable maximal volumetric sampling and viewing of the breast and chest wall. Images of geometric/anthropomorphic phantoms were acquired using various fixed-tilt circular and 3D sinusoidal trajectories. The iteratively reconstructed images showed more distortion and attenuation coefficient inaccuracy from tilted cone-beam orbits than from the complex trajectory. Additionally, line profiles illustrated cupping artifacts in planes distal to the central plane of the tilted cone-beam, otherwise not apparent for images acquired with complex trajectories. This indicates that undersampled cone-beam data may be an additional cause of cupping artifacts. High-frequency objects could be distinguished for all trajectories, but their shapes and locations were corrupted by out-of-plane frequency information. Although more acrylic balls were visualized with a fixed-tilt and nearly flat cone-beam at the posterior of the breast, 3D complex trajectories have less distortion and more complete sampling throughout the reconstruction volume. While complex trajectories would ideally be preferred, negatively fixed-tilt source-detector configuration demonstrates minimally distorted patient images.

(Some figures in this article are in colour only in the electronic version)

1. Introduction

Over the past decade, dual-modality tomographic imaging systems have grown in both clinical and preclinical popularity and offer great promise in the detection and staging of numerous

cancerous diseases, monitoring and prediction of treatment therapies and improving precision of surgical biopsies. The main benefit of acquiring 3D transmission and emission data is in the ability to fuse the anatomical framework of an object obtained from a transmission image with an emission image that provides the *in vivo* localization of the molecular tracer, e.g. in a tumor. Additionally, the transmission data can be used as an attenuation map to compensate the emission data for photon attenuation and absorption by overlapping structures, making the molecular images more quantitatively and spatially accurate. It is anecdotally observed that integrating complementary anatomical and molecular functional information can lead to further improvements in visual quality and quantitative accuracy over independent systems alone (Shreve 2000, Israel *et al* 2001, Hany *et al* 2002, Hasegawa *et al* 2002, Schillaci and Simonetti 2004).

Our lab has been working on developing such a dual-modality single photon emission computed tomography (SPECT) and computed tomography (CT) imaging system specifically dedicated to fully 3D breast imaging (Crotty *et al* 2005, 2006, Madhav *et al* 2006). With the compact, high performance gamma camera of the SPECT system (Brzymialkiewicz *et al* 2006) and the novel quasi-monochromatic x-ray cone-beam of the CT system (McKinley *et al* 2005b), both systems have independently yielded visualization of small lesions in the breast, especially ones closer to the chest wall. Each system was first developed on its own 3D positioning gantry which permitted simultaneous azimuthal and polar tilting motion capabilities (Brzymialkiewicz *et al* 2005, McKinley *et al* 2005a). This allowed the source–detector combinations to be positioned anywhere in a hemisphere about a pendant, uncompressed breast during a tomographic acquisition.

In its initial hybrid integration described here, the SPECT system retains its fully 3D positioning capability. However, the CT system is placed at a fixed-tilt angle and restricted to only a 360° circular rotation around the vertical axis of a pendant breast. Various groups that have developed cone-beam dedicated breast CT tomographic scanners have also been limited to using a circular scan during image acquisition (Chen and Ning 2002, Vedula and Glick 2003, Chen *et al* 2005, Boone *et al* 2006). This limits the CT system in its ability to image deep into the breast and chest wall, and introduces insufficient sampling which has previously been shown to be eliminated by using 3D complex acquisition trajectories (Kudo and Saito 1990, Zeng *et al* 1994, Junhai *et al* 2003, McKinley *et al* 2005a, Tornai *et al* 2005). In this study, we describe the configuration of the dual-modality SPECT-CT system and evaluate the effects on object distortion with the CT system at different stationary tilts. It is necessary to determine if a stationary tilt will (1) permit maximal access to the patient's breast; and (2) provide sufficiently sampled information.

2. Materials and methods

2.1. Overview of the SPECT-CT system

The first prototype compact dual-modality SPECT-CT system was built (figure 1) for imaging pendant uncompressed breasts (Madhav *et al* 2006). Both systems, using separate detectors to view an object in the common field-of-view (FOV), rest on a common rotation stage (model RV350CCHL, Newport Corp., Irvine, CA) to allow an azimuthal rotation of 360° around the vertical axis of the breast. The SPECT system is positioned 90° relative to the x-ray source–detector axis. With both systems on the same gantry, the subject is not required to move in between the SPECT and CT acquisitions. A customized patient bed, placed above the hybrid system, is built to allow for patient comfort, shield from scatter x-rays and avoid collision with the equipment below (Crotty *et al* 2007a).

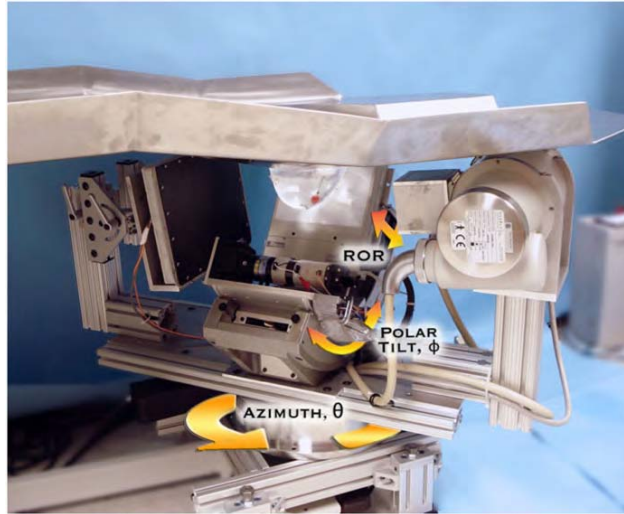


Figure 1. Photograph of the prototype dual-modality dedicated breast imaging tomographic system. The SPECT sub-system (center, back) is placed orthogonally to the x-ray tube (right, front) and digital flat-panel detector (left, toward back). The arrows illustrate system motions (azimuthal, polar and radius of rotation (ROR)). A customized patient bed is located above the hybrid system, shown with a breast phantom pendant through the center opening in the table. Note that the lesion-containing breast phantom is in the common FOV of both systems.

Our current parallel-beam emission tomography system uses a compact $16 \times 20 \text{ cm}^2$ field-of-view Cadmium Zinc Telluride (CZT) gamma camera (model LumaGEM 3200STM, Gamma Medica, Inc., Northridge, CA) with discretized crystals, each $2.3 \times 2.3 \times 5 \text{ mm}^3$ on a 2.5 mm pitch. The measured energy resolution of the gamma camera at 140 keV is 6.7% FWHM and the collimator sensitivity is $37.9 \text{ cps MBq}^{-1}$ (Brzymialkiewicz *et al* 2005). Higher energy resolution is the primary reason for using the CZT camera over a scintillator-based camera for the SPECT system. This system has a parallel-hole collimator with hexagonal holes (1.2 mm hole size flat-to-flat, 0.2 mm septa and 25.4 mm height). The camera is attached to a laboratory jack (model M-EL120, Newport Corp., Irvine, CA) and a goniometric cradle (model BGM200PE, Newport Corp., Irvine, CA) permitting various radius of rotations (RORs) and polar tilts (ϕ), respectively.

Our existing cone-beam transmission tomography system uses a rotating tungsten target x-ray source (model Rad-94, Varian Medical Systems, Salt Lake City, UT) with a 0.4/0.8 mm nominal focal spot size and 14° anode angle and a $20 \times 25 \text{ cm}^2$ FOV CsI(Tl)-based amorphous silicon digital x-ray detector (model Paxscan 2520, Varian Medical Systems, Salt Lake City, UT) with a grid size of 1920×1536 pixels and $127 \mu\text{m}$ pitch. Source and detector are secured to the same aluminum plate as the SPECT system. A custom-built collimator is attached to the x-ray source to hold ultra-thick K-edge beam shaping filters to produce a quasi-monochromatic beam (McKinley *et al* 2005b). The advantages of using a quasi-monochromatic source are (1) improving the visualization of tissues with very small differences in attenuation coefficients; (2) using a low x-ray dose and (3) minimizing beam hardening effect. For these studies, a 60 kVp x-ray beam and a 0.051 cm cerium filter ($Z = 58$, $\rho = 6.77 \text{ g cm}^{-3}$, K-edge = 40.4 keV, Santoku America, Inc., Tolleson, AZ) were used. This filter was approximately a 100th attenuating value layer which reduced the exposure of the incident x-ray beam by a factor of 100 and yielded a spectrum that had a mean energy of approximately 36 keV and the

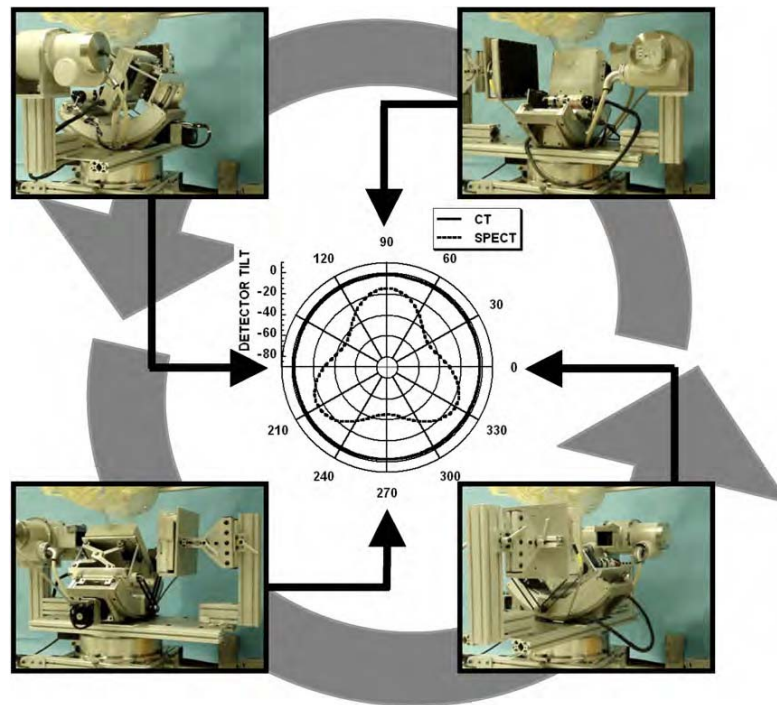


Figure 2. Photographs at different positions of the dual-modality system rotating around a pendant, uncompressed breast and torso phantoms. Polar plot (center) is shown for the SPECT (3D noncircular trajectory) and CT sub-systems (simple fixed-tilt circular orbit).

FWHM of 15% (McKinley *et al* 2004). In the current hybrid setup, the source-to-image distance (SID) is 60 cm and source-to-object distance (SOD) is 38 cm resulting in a magnification of 1.57 for an object located at the center of rotation of the system.

Figure 2 illustrates the current dual-modality SPECT-CT system rotating around a pendant uncompressed breast phantom. As shown in the corresponding polar plot, the SPECT sub-system has fully 3D positioning capabilities while the CT sub-system remains at a fixed polar tilt as the system rotates 360° around the breast. Along with the parallel-beam imaging geometry of the SPECT sub-system, the entire volume of the breast is in the FOV of both systems even at different cone-beam CT tilts (figure 3).

2.2. Data acquisition

Object visualization, distortion and frequency dependence at different planes of the image volume were measured using a Defrise-type disk phantom (model ECT/MI-DEF/P, 5 mm disk thickness, 5 mm disk spacing, Data Spectrum Corp., Hillsborough, NC) with and without 3.5 mm acrylic balls placed in the interstitial spaces between the disks (figure 4, left). Another measurement utilized a breast phantom consisting of numerous acrylic balls suspended throughout the entire volume. These 'suspended spheres' were created by arranging 5 mm diameter acrylic balls on 10 mm center-to-center pitch in a cross pattern on a thin plastic sheet. Each plastic sheet was stretched and glued to the bottom of a circular acrylic frame (20 mm height). These circular bands of varying diameters were stacked together to roughly

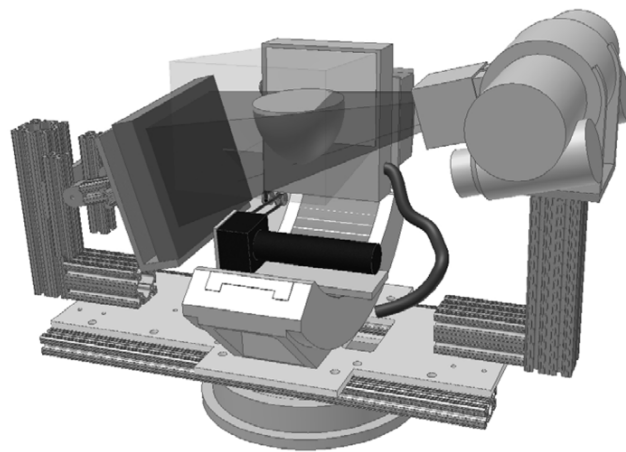


Figure 3. 3D CAD model of the SPECT-CT system with a breast placed at the center of rotation. The breast is in the common FOV of both systems regardless of the tilt of the CT sub-system. Translucent volumes illustrate the intersection of both the parallel-beam of the SPECT sub-system and the cone-beam of the CT sub-system.

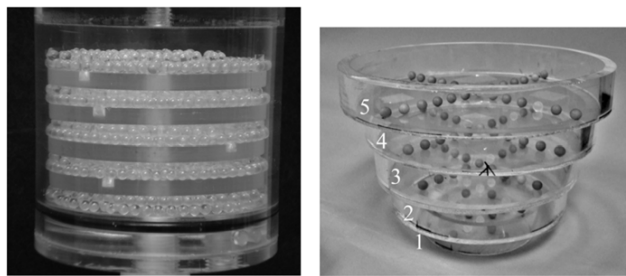


Figure 4. (left) Photograph of the disk phantom with 3.5 mm acrylic beads in the gaps between the disks. (right) Photograph of 5 mm diameter acrylic spheres suspended on thin plastic sheets inside each circular band. Each frame or level is labeled 1 through 5, with 1 being the smallest diameter frame.

contour the shape of the breast (figure 4, right). The frames could also be immersed in liquids while retaining the distribution of spheres on a single, nominally attenuating plane. For this set of experiments, five circular concentric frames were placed in a 1050 mL breast phantom shell (nipple-to-chest distance of 11 cm, medial-to-lateral distance of 17 cm and superior-inferior distance of 18 cm). Throughout this paper, each frame of this phantom will be referred to by a number with one representing the circular band with the smallest diameter (nearest the pendant nipple).

Several measurements were taken in air and with the breast uniformly filled with mineral oil to provide different contrasts between the acrylic spheres and breast background. Due to the physical distortion of the breast phantom after filling it with oil (i.e. due to the added weight), only the four smallest annular disks fit in the breast shell. Mineral oil has an intrinsic density of 0.87 g cm^{-3} and acrylic has a density of 1.19 g cm^{-3} .

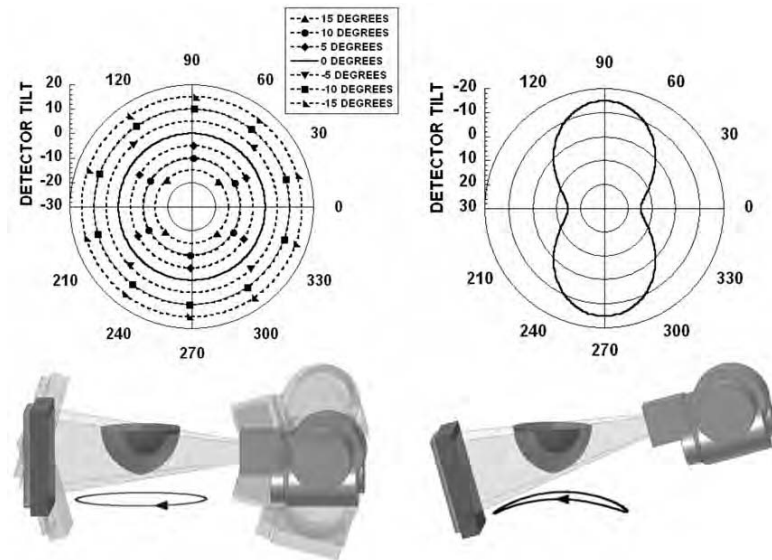


Figure 5. (top) Polar plots for (left) simple tilted circular orbits and (right) 3D saddle trajectory. Polar tilt is defined by the radius of the circle, and the azimuthal angle (location) is defined around the circumference of the circle. (bottom) The 3D CAD drawings of the CT system setup and dark circles underneath are shown to illustrate the location(s) of the source–detector pair during an acquisition. Negative polar tilt is defined as the x-ray detector moving down (or the x-ray source moving closer to the patient bed).

Initial measurements were obtained using a simple circular trajectory at 0° , $\pm 5^\circ$, $\pm 10^\circ$ and $\pm 15^\circ$ fixed polar tilts (figure 5, left), and a saddle trajectory having $+15^\circ$ to -15° ranging polar tilts (figure 5, right). The CT system pivots at the intersection point between the central ray of the cone-beam and center-of-rotation axis. A prior study showed that using a noncircular acquisition orbit (i.e. saddle trajectory) will improve sampling (satisfying Tuy's data sufficiency condition) and reduce distortion (McKinley *et al* 2005a). Note that a negative polar tilt is defined as the x-ray source moving up (closer to the patient bed) and the detector moving down (closer to the ground). For ease of acquiring images using the various tilted circular orbits and complex 3D trajectory motion, all acquisitions were taken on the independent CT system which had a 55 cm SID, 35 cm SOD and 1.57 magnification. In this setup, the x-ray source and detector were affixed on their own base plate which rested on top of the goniometer and rotation stage. Similar to the SPECT sub-system on the hybrid device, the goniometer allowed the CT system to be tilted in the polar direction to provide the flexibility to acquire tomographic projection data at various fixed tilted circular orbits and complex trajectories. Tube potential was set at 60 kVp with a 1.25 mAs exposure per projection (McKinley and Tornai 2006). Projection images were collected every 1.5° through a 360° azimuthal acquisition for a total of 240 projections. The total scan time for each acquisition was 6 min. Although the breast is somewhat truncated (seen in figure 5), the suspended sphere phantom was placed in the breast volume such that it was in the center of the field-of-view and not truncated.

2.3. Patient study

A volunteer with biopsy confirmed breast cancer (adenocarcinoma) in her left breast was imaged with the dedicated breast CT sub-system having a tilted circular orbit, under a protocol

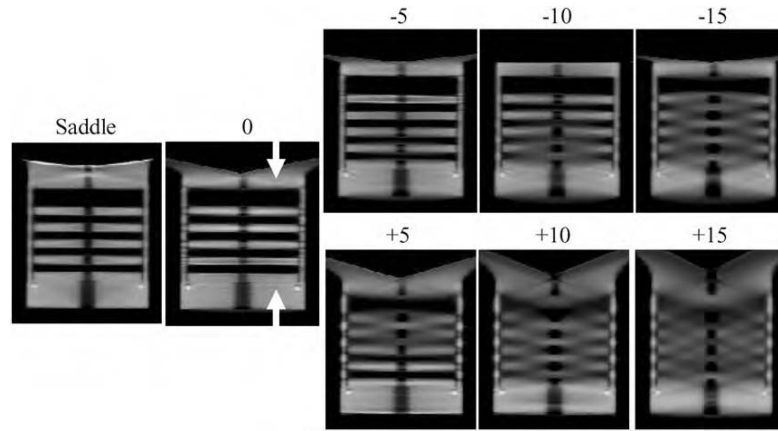


Figure 6. Sagittal reconstructed slices of the disk phantom for 0, ± 5 , ± 10 and ± 15 , and saddle acquisition trajectories.

approved by the Duke University Medical Center institutional review board (IRB). Informed written consent was obtained.

The subject was scanned with the hybrid system and a customized patient bed. The CT sub-system was at a -6.2° tilt for the entire 360° acquisition. Tube potential was set at 60 kVp with a 1.25 mAs exposure using our standard Ce filtration.

2.4. Image reconstruction and data analysis

Image reconstruction was performed on the CT projection images by increasing the log likelihood via the iterative ordered-subset transmission reconstruction algorithm (OSTR) (Erdogan and Fessler 1999), using a ray-driven image reconstruction code, CT-Map (Bowsher *et al* 2002), which also accounted for the 3D motion of the CT system (McKinley *et al* 2005b). Projection images were corrected for gain and offset and binned to 4×4 pixels. Reconstruction parameters were set to 5 iterations, 16 subsets, a $350 \times 350 \times 384$ reconstruction grid and a $508 \mu\text{m}^3$ voxel size. The total reconstruction time in this iterative framework was 4 h.

Object distortion was observed using the sagittal and coronal reconstructed slices of the disk and suspended sphere phantoms collected for all acquisition orbits. Horizontal and vertical line profiles were also drawn through the disks and acrylic balls to compare the differences in image distortion and artifacts for all acquisition trajectories.

3. Results and discussion

3.1. Disk phantom without acrylic balls

The sagittal reconstructed slices of the disk phantom (figure 6) show that the tilted cone-beam acquisition orbits result in disk distortion especially for images acquired at higher positive tilts, where it becomes more difficult to visibly separate out each of the five disks. At some locations in the reconstructed volumes, the apparent positions of the disk and air layer appear to be reversed, a common problem with aliased or highly undersampled tomographic data. Tuy's data sufficiency condition states that for cone-beam imaging, each plane crossing the object must intersect the orbit of the focal point at least once (Tuy 1983, Smith 1985). Due to

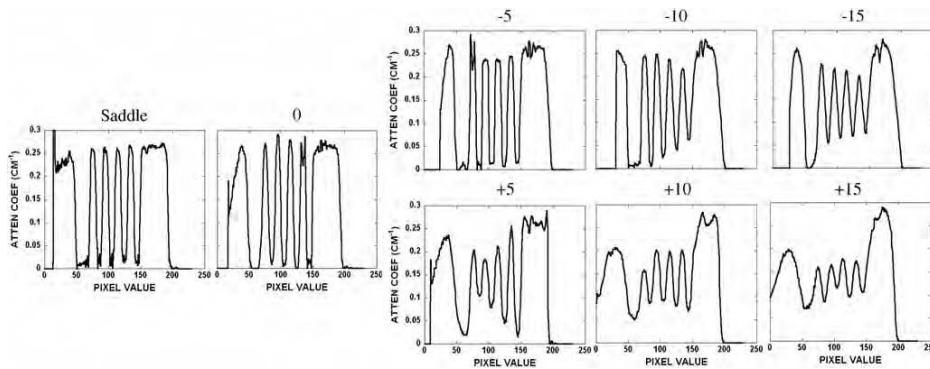


Figure 7. Line profiles obtained vertically through the disks in the disk phantom for all acquisition trajectories. Values indicate degrees of tilt or complex trajectory. Figure 6 indicates the position of the line profile shown between the white arrows.

the failure to meet this condition with a wide cone-beam, reconstruction of slices for locations further away from the flat plane of the beam (which is parallel to the ground and intersects the focal point) contains significant distortion and errors. This incompleteness in circular trajectories with cone-beam acquisitions has been seen to degrade the reconstructed images, especially with the use of large cone angles (Webb *et al* 1987, Kudo and Saito 1990, Davis 2005, McKinley *et al* 2005a).

Figure 5 (bottom left) illustrates the cause of the insufficient sampling in our experimental setup. When the CT system is at a -10° tilt with the detector positioned down (closer to the ground), the cone-beam is relatively flat near the top of the phantom. This location would be nearer to a patient's chest wall. Better sampling and minimal disk distortion are seen in the top area of the reconstructed images since these planes intersect the orbit of the vertex of the cone-beam (figure 6, top row). A loss in resolution and inaccuracy in reconstruction are observed when the x-rays travel at a large enough angle that intersects at least two disks. Not surprisingly, the reverse is true for the $+10^\circ$ tilt case, where the insufficient sampling now occurs for slices that are reconstructed from divergent x-rays away from the flat plane at the bottom of the cone-beam (figure 6, bottom row). Due to the large included cone-beam angle of 28° , geometric distortion increases with circular orbits. However, this limitation can be overcome by using a 3D complex acquisition trajectory such as a saddle orbit, which is easily implemented on our independent, 3D CT imaging system. As shown in the reconstructed image slices (figure 6, left), the saddle trajectory can reproduce the object with minimal geometrical distortion due to the improved sampling throughout the object volume.

A vertical line profile was obtained for all trajectories semi-quantitatively confirming the disk distortion (figure 7) seen in the earlier reconstructed images (figure 6). The shape of the line profile for the saddle acquisition has a relatively distortion-free and constant attenuation coefficient value through each of the five disks and cylindrical support structure, in contrast to the varying results from the tilted acquisition trajectories. Those other profiles illustrate definite distortion and artifacts especially for planes farther away from the flat, more completely sampled plane of the cone-beam acquisition. These distortions cause the profiles to have a greater variation in the attenuation coefficient value among each of the disks. For instance, in the -10° tilt situation, the profile taken through the disks near the top of the disk phantom is less distorted than the profile taken through the disks further away. Therefore, it is clearly illustrated how complex 3D acquisition trajectories can overcome these cone-beam

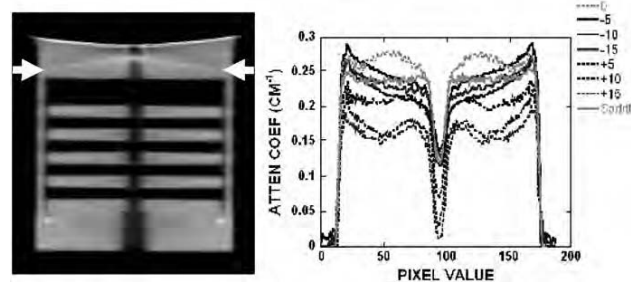


Figure 8. (left) Reconstructed sagittal slice of the disk phantom acquired with the saddle trajectory. (right) Horizontal line profile for all acquisition trajectories. Arrows indicate the position of the profile.

sampling artifacts, especially for the outer planes of the beam where distortions become more significant.

A horizontal line profile was also drawn across regions of the reconstructed images of the disk phantom (figure 8, right). For the profiles obtained with simple circular orbits, cupping artifacts were observed and became worse at locations further away from the flat horizontal plane of the cone-beam. Cupping artifacts are generally considered to be consisted of scatter and beam hardening in the projection images. Since the disks are virtually suspended in air, scatter is minimal in this experimental setup. Also, the independent dedicated breast CT system uses a quasi-monochromatic beam which virtually eliminates beam hardening (McKinley *et al* 2005b, Crotty *et al* 2007b). Therefore, the apparent cupping artifacts are most likely caused by data insufficiency. The profile in figure 8 shows the saddle trajectory having more constant profile values than the other tilted circular acquisition orbits. Using a table of x-ray mass attenuation coefficients, the measured attenuation coefficient of acrylic at 36 keV is 0.30 cm^{-1} (Hubbell and Seltzer 1996). The line profile shows a reduced attenuation coefficient value primarily due to the presence of scatter. Negative circular acquisition orbits display a slight cupping artifact due to the location of the flat plane of the cone-beam relative to the position of the line profile. A distinct and consistent decrease in attenuation coefficient values at higher positive angle acquisition orbits is observed since this region is in the outer planes (i.e. x-rays at larger angles) of the cone-beam, relative to where the profile was measured.

3.2. Disk phantom containing additional acrylic balls

Disk distortion due to undersampling was next examined with the disk phantom uniformly packed with 3.5 mm acrylic beads in the interstitial spaces between each disk. The intent with this modified disk phantom was to evaluate whether there was an object frequency dependence on the reconstructed image results by imaging both the disks and considerably smaller acrylic balls simultaneously. Figure 9 shows a not surprisingly similar disk distortion as seen for the disk-only phantom without the balls. Furthermore, despite the inaccurate reproduction of the disks located further away from the fully sampled plane of the cone-beam, some small acrylic beads can be singled out, and appear to be less distorted in these same areas. The saddle trajectory-acquired data, which clearly illustrate the visualization of all balls in that given slice, can be used as the standard with which to compare all the other acquired and reconstructed data. A line profile through the bottom row of acrylic balls in the phantom confirms that each can be distinctly separated (figure 10). These findings suggest that identifying an amorphous object in reconstructed space partly depends on the distribution of its frequency components (Bartolac

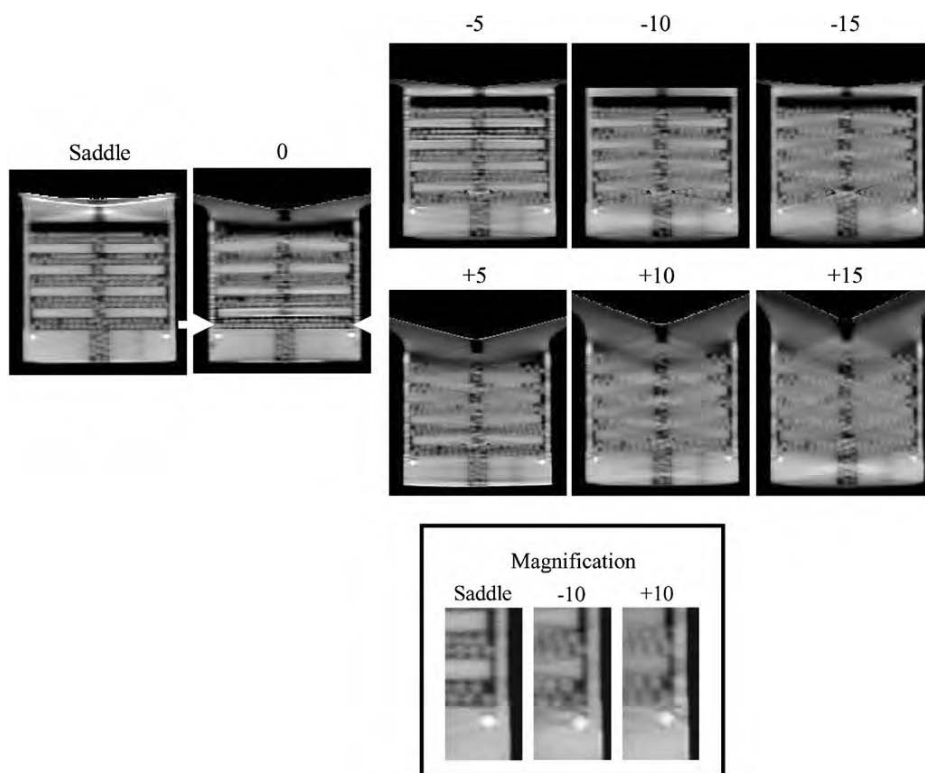


Figure 9. Sagittal reconstructed central slices of the disk phantom containing additional acrylic balls for 0, ± 5 , ± 10 and ± 15 , and saddle acquisition trajectories. (Bottom) Magnification of a small area of the disk phantom for ± 10 and saddle acquisition trajectories to illustrate the visualization of the acrylic balls.

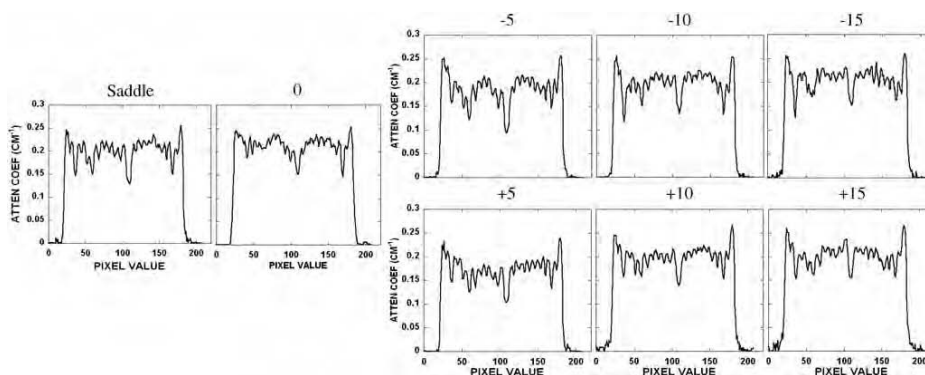


Figure 10. Horizontal line profile taken through the bottom row of acrylic balls in the disk phantom for all acquisition trajectories. Figure 9 indicates the position of the line profile shown between the white arrows.

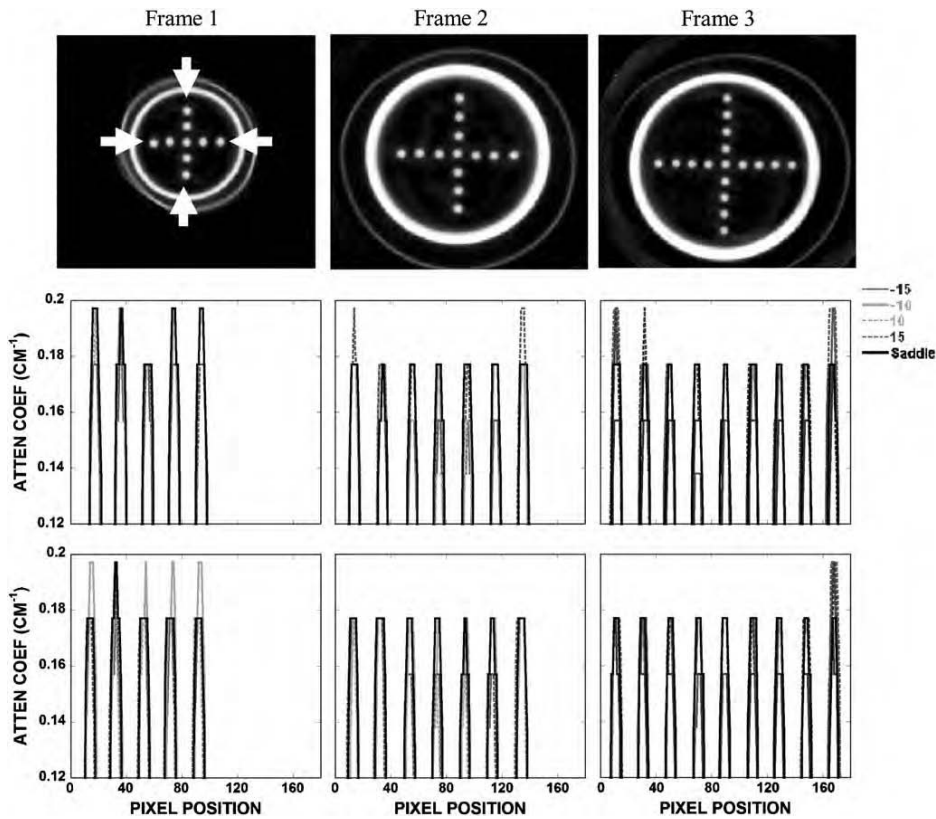


Figure 11. (top) Reconstructed coronal slices of the spheres arranged in a cross pattern acquired with saddle. Outer thin perimeter is the actual breast cup; inner thicker annulus is the acrylic frame supporting the sheet suspending the balls. (middle) Vertical and (bottom) horizontal profiles drawn through the acrylic balls along the directions indicated between the white arrows.

et al 2006). In this case, the high frequency and discrete objects (i.e. acrylic balls) remain more preserved than the low-frequency information (i.e. disks). One study has previously shown that data collected with larger cone angles sustained high-frequency details despite the distortion and artifacts associated with cone-beam imaging, while smaller cone angles maintained low-frequency details at the expense of the lower signal-to-noise ratio (Davis 2005). Our results with the dedicated mammotomographic imaging system are consistent with these previous findings. For all tilted orbits, figure 9 shows that the low-frequency information in the disks is preserved around the area of the flat plane of the cone-beam (i.e. small cone angles) while at locations further away (i.e. large cone angles) the high-frequency information of the acrylic spheres is kept regardless of the disk distortion. Not surprisingly, use of the more completely sampling saddle trajectory nearly completely eliminates these sampling-related distortions.

3.3. Suspended spheres in air in the breast phantom

Object distortion was additionally examined in different coronal slices of a breast-shaped phantom with the suspended sphere phantom inside its tiered frame. Horizontal and

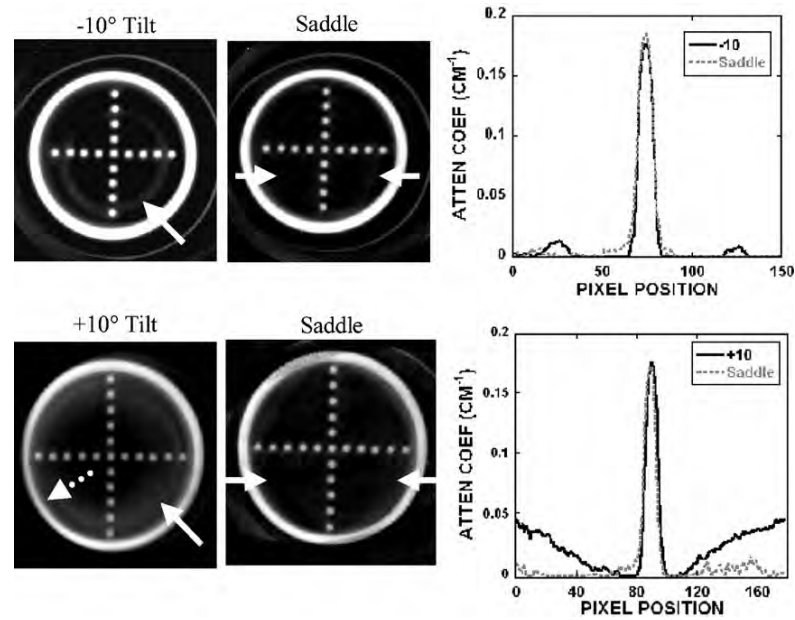


Figure 12. (top left) Reconstructed slice of frame 3 obtained with the -10° tilted orbit. (bottom left) Reconstructed slice of frame 4 obtained with the $+10^\circ$ tilted orbit. Solid arrow illustrates an overlapped region in which the frame below can also be seen in this single slice (shown at the arrow tip). Dotted arrow illustrates the geometric distortion of the acrylic frame. (middle column) Reconstructed slice of the same phantom acquired with the saddle trajectory. (right column) Line profile (obtained from between arrows on the saddle slice) shows some artifacts due to the overlapped regions in the slice acquired with the (top) -10° and (bottom) $+10^\circ$ tilts.

vertical lines drawn across images of the acrylic balls in the three smallest circular disks (frames 1–3) placed closest to the nipple showed negligible differences among different acquisition trajectories (i.e. fixed tilt or saddle) (figure 11). However, close inspection of the reconstructed coronal slices through each of the annular disks obtained using stationary polar tilt orbits revealed overlapping structures (figure 12). For the -10° tilt cone-beam acquisition, there is nearly complete sampling close to the top slice (near the chest wall) where all objects are more completely sampled and no overlapping (i.e. out-of-plane) structures can be seen there. However, with a negative system tilt, overlapping structures (i.e. from the frame below) become more noticeable in reconstructed slices closer to the nipple (figure 12, top left). Due to the insufficient polar sampling that does not ‘fill in’ additional views of the object in the FOV, out-of-plane information is inaccurately superimposed on any single plane of interest (shown by the white solid arrow in figure 12, top left). The reverse trend is true in the $+10^\circ$ tilt case (figure 12, bottom). However, using the saddle trajectory, there is more complete polar sampling yielding far fewer noticeable artifacts in the reconstructed slices (figure 12, middle column). The line profiles (figure 12, right column) illustrate how out-of-plane object information acquired with an incomplete sampling trajectory can contribute contaminated information into a given plane of interest. With 3D acquisition trajectories, such as saddle, there is more complete sampling of the object volume in the polar and azimuthal directions, resulting in the reduction of overlapping structures originating out-of-plane. Although more of the acrylic balls can be clearly seen when the top of the cone-beam is level (i.e. -10° tilt)

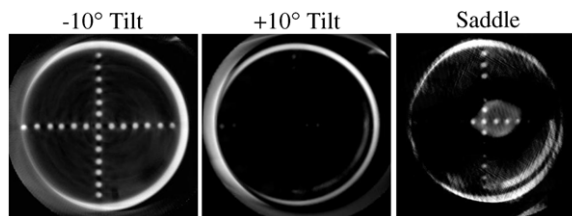


Figure 13. Reconstructed slice of frame 5 acquired at (left) -10° , (middle) $+10^\circ$ tilt and (right) saddle trajectory. The top plane at the -10° tilt is more uniformly sampled, whereas this frame is out of the FOV for many of the angles with the other two trajectories. Even though more acrylic balls are seen at the -10° tilt, 3D complex trajectories have less distortion and more complete sampling throughout the reconstruction volume.

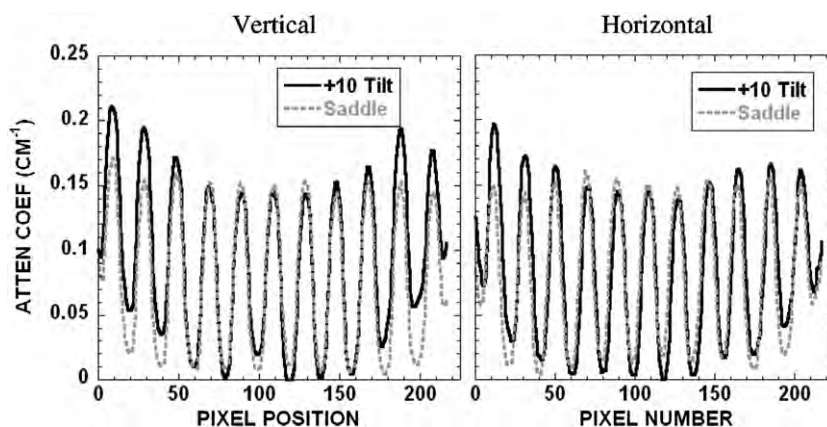


Figure 14. (left) Vertical and (right) horizontal profiles over lesions of frame 4 obtained with the $+10^\circ$ tilt and saddle shown in figure 12, bottom.

near the back of the pendant breast (i.e. near chest wall), complex 3D trajectories overall allow for less distortion and more complete sampling (figure 13).

Profiles drawn over the acrylic balls of frame 4 shown in figure 12, bottom, are illustrated in figure 14. Consistent with the earlier disk measurements (figure 8), the horizontal and vertical profiles also show that there is a cupping artifact with the fixed-tilt orbit by observing the intensities from the edge toward the center, which could be mistaken for scatter or beam hardening. This is missing from the saddle-acquired data due to its more sufficient sampling throughout the imaged volume.

Effects of insufficient sampling were also seen in the reoriented sagittal slices of the breast phantom (figure 15). When the system is at a -10° tilt, there is better sampling at the top of the reconstructed volume compared with the bottom. This is illustrated by the uniformity of the peak heights of the profiles across the FOV. This phenomenon is reversed for the $+10^\circ$ tilt, which again shows a similar cupping artifact as illustrated earlier, in which the plane was located at an extreme edge of the cone-beam. However, while the particular image shows artifacts at the top with a saddle trajectory, line profiles confirm that there is uniformity of signal amplitude through the entire reconstructed volume, for the indicated spheres.

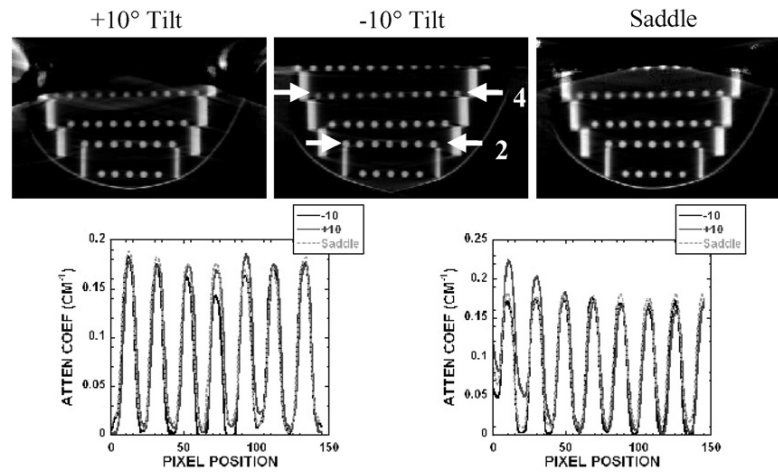


Figure 15. (top) Sagittal reconstructed slices of the ball phantoms acquired at indicated trajectories. (bottom) Profiles drawn through the ball phantom (bottom left) at frame 2 (indicated in the top-middle image) and (bottom right) at frame 4. Tilt at -10° shows greater peak uniformity at frame 4, while the $+10^\circ$ tilt shows more uniformity at frame 2. Saddle trajectory shows stable peak height uniformity throughout the reconstructed volume.

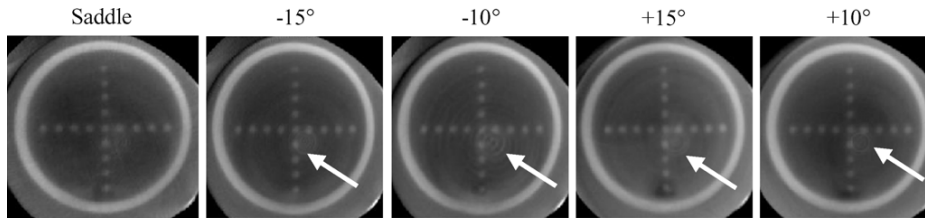


Figure 16. Reconstructed slices of frame 3 of the suspended sphere phantom in oil acquired at various acquisition trajectories as indicated. Although the breast phantom is truncated, the circular frames are completely in the FOV. Images acquired with a fixed polar tilt and circular orbit had a circular ring due to nonuniformity errors (indicated by an arrow) in some of the reconstructed slices. However, in the same slice for the saddle trajectory, there is no circular ring apparent.

3.4. Suspended spheres in oil in the breast phantom

In order to assess whether these phenomena are visible in lower contrast environment, the breast shell containing the suspended sphere phantom was uniformly filled with mineral oil. Figure 16 shows the reconstructed slices of frame 3 measured with the different indicated trajectories. When examining the images for all trajectories, a series of circular rings appear in the reconstructed slices, except for the saddle trajectory. Typically, these rings in reconstructed images occur due to the nonuniform response between detector elements, errors in detector gain calibration, etc. The advantage of using a 3D complex trajectory such as saddle is that since the same detector element does not always view the object from the same vantage point, the detector nonuniformity effect is not compounded hence amplified. For this reason, reconstructed images acquired with the 3D saddle trajectory tend to not have these artifacts.

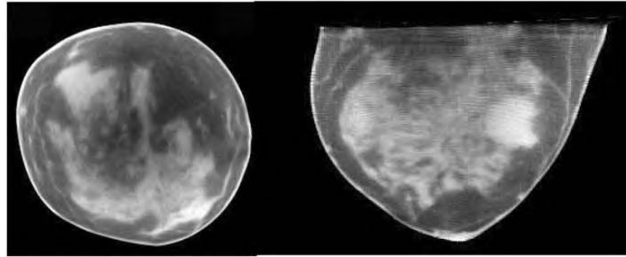


Figure 17. Reconstructed CT (left) coronal and (right) transverse image slices of human subject volunteer.

As with the experiments in air, horizontal line profiles (not shown here) drawn over the acrylic balls near the chest wall (or back of the breast phantom) also showed improved sampling for the negative tilted orbits, since this layer of the phantom was located closer to the flat part of the cone-beam.

3.5. Patient data

Figure 17 shows the result of our first CT patient study acquired with a -6.2° tilted orbit. The real human subject data are meant to illustrate here the high-frequency content as well as the nonuniform nature of the object ultimately intended to be imaged. Although the geometric phantoms have shown the known and consistent artifacts due to undersampling with circular cone-beam acquisitions, these patient images show that the perception of distortion and reconstruction inaccuracy are minimal and details are preserved (Madhav *et al* 2008). As described in the previous sections, this is due to small negative tilts having more complete sampling near the chest wall and the components of the breast consisting of more high-frequency detail.

4. Conclusion

Imaging with a dedicated dual-modality breast imaging tomographic system may help to improve identification and localization of lesions during patient screening, diagnostic work-ups and therapeutic monitoring of response. The two main advantages of having a dedicated versus a whole-body imaging system are that the x-ray radiation dose is limited to only the breast and axillary regions. Thus, imaging can be optimized for the breast, and potentially 'peer' into the chest wall and axillary region to improve the detection of small breast tumors without unduly contorting the subjects. Furthermore, this system can acquire images sequentially with the SPECT and CT sub-systems without transferring the subject from one location to another or moving the patient bed in between acquisitions. This should minimize acquisition time and allow SPECT and CT images to be consistent and correlate with each other for easier co-registration. Our current prototype dedicated SPECT-CT system can provide volumetric fully 3D registered and fused breast images. This system can image an entire breast close to the chest wall to facilitate the detection and biopsy of small tumors without breast compression. This system has common emission (SPECT) and transmission (cone-beam CT) FOVs that intersect each other, as opposed to being either on separate systems or linearly juxtaposed on separate gantries.

Here, the CT component of the hybrid assembly was characterized for various system orientations and acquisition trajectories. Imaging results of the disk phantom with and without

acrylic balls, and tiered cross-shaped ball phantoms suspended throughout the 3D breast volume acquired using stationary polar tilted simple circular orbits, demonstrated geometric distortions and reconstruction inaccuracies (i.e. overlapping structures, circular ring) that manifest themselves as cupping artifacts. These cupping artifacts are distinctly different from those commonly known to arise from scatter and beam hardening. Given that insufficient cone-beam sampling yields an additional component of reconstruction ‘cupping’, any general scatter correction algorithm applied to these regions may indeed ‘flatten’ the response across the image, but would incorrectly account for the measured scatter response. That resulting data could not explicitly be considered quantitative in terms of resulting attenuation coefficients. Blur around the disks in the disk phantom was progressively observed away from the horizontal plane of the cone-beam, which had the more complete sampling using simple circular orbits. From the results of this study, we suggest that these incomplete sampling-based cupping artifacts are an addition to but distinct from any scatter or beam hardening induced cupping artifacts, indicating that simple scatter correction algorithms present in some systems may thus overestimate the scatter correction. Additionally, the results also showed that high-frequency information (smaller object size) was more preserved in incompletely sampled data, implying that resolution recovery is also dependent on the frequency components of an object. One caveat to note about the object frequency dependence, however, is that there may still be incorrect information transferred from out-of-plane regions into any plane of interest due to incomplete sampling. Thus, interpreting absolute attenuation coefficients should be made cautiously unless the system has more complete polar sampling as well.

Currently in our prototype dual-modality dedicated mammotomography system, the CT component has a stationary tilt. Results indicate that having the cone-beam flat closer to the chest wall (i.e. negative CT system tilt) allows for more complete sampling near the chest wall, and more lesion-like small spherical objects can be clearly seen than for a completely sampled complex 3D trajectory. The drawback is that there are overlapping structures throughout the volume, geometric distortion and incomplete sampling in the rest of the reconstruction volume. Clinically, this can translate to decreased contrast and size estimation of a lesion in the breast, as well as inaccurate absolute attenuation coefficient determination. Regardless of these known inaccuracies due to insufficient sampling with circular cone-beam acquisitions, CT patient images have shown that distortion appears to be nominal with high resolution recovery. However, for more distortion-free images, use of complex 3D trajectories in imaging procedures having more complete and uniform sampling is suggested. Our ongoing goal is to develop a CT sub-system with a complex 3D trajectory capability as part of the hybrid system that would allow for more complete and uniform sampling of the entire image volume, and subsequently lead to more quantitative CT image content potentially useful in tissue characterization. A large number of complex 3D acquisition trajectories are possible with the completely flexible positioning CT system; many would facilitate better sampling and are under investigation and development (Crotty *et al* 2006). The volume limitation issue of complex sampling may be ameliorated by lowering the object farther into the FOV, provided it is possible to do so (Cutler *et al* 2007, Crotty *et al* 2008).

Acknowledgments

This work was supported by NIH R01-CA096821, and in part by DOD W81XWH-06-1-0791, W81XWH-08-1-0352 and DOD W81XWH-05-1-0280. MPT is the inventor of this breast CT and hybrid imaging technology, and is named as an inventor on the patent for this technology applied for by Duke. If this technology becomes commercially successful, MPT and Duke could benefit financially. MPT is a founder and consultant of Zumatek.

References

- Bartolac S, Noo F, Clackdoyle R, Moseley D, Siewerdsen J and Jaffray D 2006 A local Fourier description of artifacts in circular cone beam computed tomography *Med. Phys.* **33** 2287
- Boone J M, Kwan A L, Yang K, Burkett G W, Lindfors K K and Nelson T R 2006 Computed tomography for imaging the breast *J. Mammary Gland Biol. Neoplasia* **11** 103–11
- Bowsher J E, Tornai M P, Peter J, Gonzalez Trotter D E, Krol A, Gilland D R and Jaszczak R J 2002 Modeling the axial extension of a transmission line source within iterative reconstruction via multiple transmission sources *IEEE Trans. Med. Imaging* **21** 200–15
- Brzymialkiewicz C N, Tornai M P, McKinley R L and Bowsher J E 2005 Evaluation of fully 3D emission mammotomography with a compact cadmium zinc telluride detector *IEEE Trans. Med. Imaging* **24** 868–77
- Brzymialkiewicz C N, Tornai M P, McKinley R L, Cutler S J and Bowsher J E 2006 Performance for dedicated emission mammotomography for various breast shapes and sizes *Phys. Med. Biol.* **51** 5051–64
- Chen B and Ning R 2002 Cone-beam volume CT mammographic imaging: feasibility study *Med. Phys.* **29** 755–70
- Chen L, Shaw C C, Tu S, Altunbas M C, Wang T, Lai C, Liu X and Kappadath S C 2005 Cone-beam CT breast imaging with a flat panel detector: a simulation study *Proc. SPIE: Phys. Med. Imaging* **5745** 943–51
- Crotty D J, Brzymialkiewicz C N, McKinley R L and Tornai M P 2005 Optimizing orientation of SPECT and CT detectors through quantification of cross contamination in a dual modality mammotomography system *Proc. IEEE Med. Imaging Conf.* **3** 1672–6
- Crotty D J, Brzymialkiewicz C N, McKinley R L and Tornai M P 2006 Investigation of emission contamination in the transmission image of a dual modality computed mammotomography system *Proc. SPIE: Phys. Med. Imaging* **6142** 664–74
- Crotty D J, Cutler S J, McKinley R L, Madhav P, Perez K L and Tornai M P 2008 Improved chest wall imaging through combined circular trajectories in dedicated dual modality SPECT-CT breast molecular imaging *Proc. IEEE MRBC Conf.* pp 5650–65
- Crotty D J, Madhav P, McKinley R L and Tornai M P 2007a Investigating novel patient bed designs for use in a hybrid dual modality dedicated 3D breast imaging system *Proc. SPIE: Phys. Med. Imaging* **6150** 65101H
- Crotty D J, McKinley R L and Tornai M P 2007b Experimental spectral measurements of heavy K-edge filtered beams for x-ray computed mammotomography *Phys. Med. Biol.* **52** 603–16
- Cutler S J, Madhav P, Perez K L, Crotty D J and Tornai M P 2007 Comparison of reduced angle and fully 3D acquisition sequencing and trajectories for dual-modality mammotomography *Proc. IEEE Med. Imaging Conf.* **6** 4044–50
- Davis G 2005 Explicit control of image noise and error properties in cone-beam microtomography using dual concentric circular source loci *Nucl. Instrum. Methods Phys. Res. A* **547** 679–85
- Erdogan H and Fessler J A 1999 Ordered subsets algorithms for transmission tomography *Phys. Med. Biol.* **44** 2835–51
- Hany T F, Steinert H C, Goenes G W, Buck A and von Schulthess G K 2002 Improvement of diagnostic accuracy of PET imaging using an in-line PET-CT system—initial results *Radiology* **225** 575–81
- Hasegawa B H, Wong K H, Iwata K, Barber W C, Hwang A B, Sakdinawat A E, Ramaswamy M, Price D C and Hawkins R A 2002 Dual-modality imaging of cancer with SPECT/CT *Technol. Cancer. Res. Treat.* **1** 449–58
- Hubbell J H and Seltzer S M 1996 Tables of x-ray mass attenuation coefficients and mass energy-absorption coefficients 1 keV to 20 MeV for elements $Z = 1$ to 92 and 48 additional substances of dosimetric interest (Gaithersburg: National Institutes of Standards and Technology)
- Israel O, Keidar Z, Iosilevsky G, Bettman L, Sachs J and Frenkel A 2001 The fusion of anatomic and physiologic imaging in the management of patients with cancer *Semin. Nucl. Med.* **31** 191–205
- Junhai W, Hongbing L, Wei Z, Zigang W and Zhengrong L 2003 A study on truncated cone-beam sampling strategies for 3D mammography *Proc. IEEE Med. Imaging Conf.* **5** 3200–4
- Kudo H and Saito T 1990 Feasible cone beam scanning methods for exact reconstruction in three-dimensional tomography *J. Opt. Soc. Am. A* **7** 2169–83
- Madhav P, Crotty D J, McKinley R L and Tornai M P 2006 Initial development of a dual-modality SPECT-CT system for dedicated mammotomography *Proc. IEEE Med. Imaging Conf.* **4** 2382–6
- Madhav P, Cutler S, Crotty D, Perez K, McKinley R, Marcom P, Wong T and Tornai M 2008 Pilot patient studies using a dedicated dual-modality SPECT-CT system for breast imaging *Med. Phys.* **35** 2894
- McKinley R L, Brzymialkiewicz C N, Madhav P and Tornai M P 2005a Investigation of cone-beam acquisitions implemented using a novel dedicated mammotomography system with unique arbitrary orbit capability *Proc. SPIE: Phys. Med. Imaging* **5745** 609–17
- McKinley R L and Tornai M P 2006 Preliminary investigation of dose for a dedicated mammotomography system *Proc. SPIE: Phys. Med. Imaging* **6142** 60–70

- McKinley R L, Tornai M P, Samei E and Bradshaw M L 2004 Simulation study of a quasi-monochromatic beam for x-ray computed mammotomography *Med. Phys.* **31** 800–13
- McKinley R L, Tornai M P, Samei E and Bradshaw M L 2005b Initial study of quasi-monochromatic beam performance for x-ray computed mammotomography *IEEE Trans. Nucl. Sci.* **52** 1243–50
- Schillaci O and Simonetti G 2004 Fusion imaging in nuclear medicine: applications of dual-modality systems in oncology *Cancer Biother. Radiopharm.* **19** 1–10
- Shreve P D 2000 Adding structure to function *J. Nucl. Med.* **41** 1380–2
- Smith B D 1985 Image reconstruction for cone beam projections: necessary and sufficient conditions and reconstruction methods *IEEE Trans. Med. Imaging* **4** 14–25
- Tornai M P, McKinley R L, Brzymialkiewicz C N, Madhav P, Cutler S J, Crotty D J, Bowsher J E, Samei E and Floyd C E 2005 Design and development of a fully-3D dedicated x-ray computed mammotomography system *Proc. SPIE: Phys. Med. Imaging* **5745** 189–97
- Tuy H K 1983 An inversion formula for cone-beam reconstruction *SIAM J. Appl. Math.* **43** 546–52
- Vedula A A and Glick S J 2003 Computer simulations of CT mammography using a flat panel imager *Proc. SPIE: Phys. Med. Imaging* **5030** 349–60
- Webb S, Sutcliffe J, Burkinshaw L and Horsman A 1987 Tomographic reconstruction from experimentally obtained conebeam projections *IEEE Trans. Med. Imaging* **6** 67–73
- Zeng G L, Clack R and Gullberg G T 1994 Implementation of Tuy's cone-beam inversion formula *Phys. Med. Biol.* **39** 493–507